

REPORT DOCUMENTATION PAGE

AFRL-SR-AR-TR-03-

Public reporting burden for this collection of information is estimated to average 1 hour per response, including the time for reviewing instructions, data needed, and completing and reviewing this collection of information. Send comments regarding this burden estimate or any other aspect of this burden to Department of Defense, Washington Headquarters Services, Directorate for Information Operations and Reports (0704-0188-4302). Respondents should be aware that notwithstanding any other provision of law, no person shall be subject to any penalty for failing to valid OMB control number. PLEASE DO NOT RETURN YOUR FORM TO THE ABOVE ADDRESS.

1. REPORT DATE (DD-MM-YYYY) 01/06/2003		2. REPORT TYPE Final Performance Report		3. DATES COVERED (From - To) 04/2000 - 03/2003	
4. TITLE AND SUBTITLE A Study of the thermal stability, degradation mechanism And properties of polymer/organically modified layered silicate nanocomposites				5a. CONTRACT NUMBER	
				5b. GRANT NUMBER F49620-00-1-0260	
				5c. PROGRAM ELEMENT NUMBER 61103D	
6. AUTHOR(S) Wei-Ping Pan, John T. Riley and Charles W. M. Lee				5d. PROJECT NUMBER 3484	
				5e. TASK NUMBER BS	
				5f. WORK UNIT NUMBER	
7. PERFORMING ORGANIZATION NAME(S) AND ADDRESS(ES) Western Kentucky University Foundation Building 107 1 Big Red Way Bowling Green, KY 42101				8. PERFORMING ORGANIZATION REPORT NUMBER 512401	
9. SPONSORING / MONITORING AGENCY NAME(S) AND ADDRESS(ES) Charles Y-C Lee AFOSR/NL 4015 Wilson Blvd, Room 713 Arlington, VA 22203-1954				10. SPONSOR/MONITOR'S ACRONYM(S)	
				11. SPONSOR/MONITOR'S REPORT NUMBER(S)	
12. DISTRIBUTION / AVAILABILITY STATEMENT Approve for Public Release: Distribution Unlimited					
13. SUPPLEMENTARY NOTES					
<p style="text-align: right;">20030612 025</p> <p>14. ABSTRACT PS-MMT nanocomposites were prepared via suspension free radical polymerization of styrene in the dispersed organo-MMT. The results of XRD and TEM indicated that exfoliated nanocomposites were achieved. The effect of surfactants on the properties of then synthesized nanocomposites was studied. It is found that PS-MMT nanocomposite with 5% wt% of organo-MMT gave the greatest improvement in the thermal stability, and PS-MMT nanocomposites with 7.5% of organo-MMT showed the greatest improvement in mechanical properties, comparing with that of pure PS in our experimental conditions. The alkyl chain length of surfactant used in fabricating organo-MMT affects the synthesized PS nanocomposites, the longer the alkyl chain length that the surfactant possesses, the higher glass transition temperature PS nanocomposite. It is found that the organoclay in the nanocomposites seems to play a dual role: (a) as nanofiller leading to the increase of storage modulus and (b) as plasticizer leading to the decrease of storage modulus.</p>					
<p>15. SUBJECT TERMS Nanocomposites, MMT, Polystyrene, Organo-MMT</p>					
16. SECURITY CLASSIFICATION OF:			17. LIMITATION OF ABSTRACT UU	18. NUMBER OF PAGES 96	19a. NAME OF RESPONSIBLE PERSON 19b. TELEPHONE NUMBER (include area code)
a. REPORT	b. ABSTRACT	c. THIS PAGE			



Final Performance Report

**A Study of the Thermal Stability, Degradation Mechanisms and Properties of
Polymer/Organically Modified Layered Silicate Nanocomposites**

Research Grant **F49620-00-1-0260**

April 1, 2000 to March 31, 2003

Prepared by:

Dr. Wei-Ping Pan (PI)
Dr. John T. Riley
Dr. Charles W.M. Lee

Department of Chemistry
Western Kentucky University
Bowling Green, KY 42101

DISTRIBUTION STATEMENT A

Approved for Public Release
Distribution Unlimited

TABLE OF CONTENTS

	PAGE
1. Objectives.....	8
2. Status of Effort.....	8
3. Accomplishments/New Findings.....	9
3.1. Materials Selection and Experimental.....	9
3.2. Thermal Degradation Chemistry Of Quaternary Ammonium Modified Layered Silicates.....	13
3.3. Thermal Degradation Chemistry Of Quaternary Ammonium Modified Layered Silicates.....	23
3.4. Synthesis and Characterization of Polystyrene-Organo-Montmorillonite Nanocomposites Prepared by Suspension Polymerization.....	31
3.5. Conclusions.....	37
3.6. References.....	38
4. Personnel Supported.....	40
5. Publications.....	41
6. Interactions/Transitions.....	41
7. New discoveries, inventions, or patent disclosures.....	42
8. Honors/Awards.....	42
9. Appendix.....	42
9.1. List of Tables.....	3
9.2. List of Figures.....	4
9.3. List of Schemes.....	7

LIST OF TABLES

	PAGE
Table 1. Alkyl Quaternary Ammonium Modified Montmorillonites.....	43
Table 2. Composition of Natural Product Alkyls.....	44
Table 3. Decomposition Temperatures in UHP N ₂	45
Table 4. Relative Mass Loss (TGA) During Decomposition of the N-MMTs.....	46
Table 5. Representative Organic Species Evolved from N-C18 and TMO (Pyrolysis/GC-MS).....	47
Table 6. Properties and Relative Mass Losses (TGA) During Decomposition of the P-MMTs.....	48
Table 7. Decomposition Temperatures in UHP N ₂	49
Table 8. Representative Organic Species Evolved from P-C18 and TBOPBr (Pyrolysis/GC-MS).....	50
Table 9. Representative Organic Species Evolved from P-4Ph and TPhPBr (Pyrolysis/GC-MS).....	51
Table 10. The Effect of Organophilic-Montmorillonite Content on the Properties of PS-Montmorillonite Nanocomposites.....	52
Table 11. The Effect of Surfactants on the Properties of PS-Montmorillonite Nanocomposites.....	53
Table 12. Average Molecular Weights and Polydispersed Particles of PS-MMT Nanocomposites.....	53

LIST OF FIGURES

	PAGE
Figure 1. DTG curves from conventional and high resolution TGA studies of pristine montmorillonite.....	54
Figure 2. DTG curves from conventional and high resolution TGA studies of N-CoCo.....	55
Figure 3. DTG curves from conventional TGA studies of N-C12, N-CoCo, N-Tallow and N-C18.....	56
Figure 4. DTG curves from conventional TGA studies of N-2Htallow, N-2CoCo, and N-2C18.....	57
Figure 5. Temperature dependent MS results of the evolution products for N-CoCo...	58
Figure 6. Temperature dependent MS results for the evolution products for N-C18....	59
Figure 7. 3D FTIR results for the decomposition of N-CoCo.....	60
Figure 8. 3D FTIR results for the decomposition of N-C18.....	61
Figure 9. FTIR spectra of N-CoCo at 25°C and pyrolyzed at 500°C.....	62
Figure 10. FTIR spectra of N-C18 at 25°C and pyrolyzed at 500°C.....	63
Figure 11. DTG curves from conventional TGA for trimethyl alkyl quaternary ammonium chlorides (TMO, TMD, TMC, and TMT).....	64
Figure 12. DTG curves comparing pure alkyl quaternary ammonium chloride (TMO) and the corresponding OLS (N-C18).....	65
Figure 13. DTG curves for N-CoCo as-received and after 3, 6, and 9 hours of Soxhlet extraction with ethanol.....	66
Figure 14. Comparison of the total organic content experimentally determined from TGA and predicted from MER with regards to the interlayer spacing determined from X-ray diffraction.....	67
Figure 15. In situ small angle scattering from the degradation of N-2Htallow-A and N-2Htallow-C (position of basal reflection).....	68

Figure 16. In situ small angle scattering from the degradation of N-2Htallow-A and N-2Htallow-C (FWHM of basal reflection).....	68
Figure 17. DSC curve of N-2HTallow-C from heating at 5°C/min.....	69
Figure 18. DTG curves comparing quaternary ammonium montmorillonite (N-4C8) and quaternary phosphonium montmorillonite (P-4C8).....	70
Figure 19. DTG curves from TGA studies of quaternary phosphonium bromides (TBOPBr and TPhPBr).....	71
Figure 20. DTG curves from TGA studies of quaternary phosphonium montmorillonites (P-C12, P-C14, P-C-16, P-C18, P-4Ph and P-4C8).....	72
Figure 21. Temperature dependent MS results of the evolution products for P-C12...	73
Figure 22. Temperature dependent MS results of the evolution products for P-4Ph....	74
Figure 23. Temperature dependent FTIR evolution spectra for P-C18.....	75
Figure 24. Temperature dependent FTIR evolution spectra for P-4Ph.....	76
Figure 25. Comparison of the relative rate of change (derivative) of the mass loss (DTG) and peak area (FTIR: $\text{CH}_2 = v_{\text{as}}\text{CH}_2$ and $v_s\text{CH}_2$; $\text{CH}_3 = v_{\text{as}}\text{CH}_3$ and $v_s\text{CH}_3$) for P-C18.....	77
Figure 26. The change of layer distance (d_{001}) as a function of temperature from in-situ high temperature x-ray diffraction for P-C12 and P-C18.....	78
Figure 27. DSC result for P-C18.....	79
Figure 28. DSC result for P-C12.....	80
Figure 29. DSC result for TBOPBr.....	81
Figure 30. Change in $\square_{\text{as}}(\text{CH}_2)$ and $\square_s(\text{CH}_2)$ for P-C18 as a function of temperature....	
82	
Figure 31. The reaction system of PS-MMT nanocomposites through suspension polymerization.....	83
Figure 32. XRD curves of (a) Polystyrene, and (b) PS-TMOMMT, (c) PS-TMTMMT, (d) PS-TMCMMMT, (e) PS-TMDMMT with 5.0 wt% of organo-MMT.....	84
Figure 33a. TEM image of PS-TMOMMT nanocomposite.....	85
Figure 33b. TEM image of PS-TMDMMT nanocomposite.....	86
Figure 34. DSC curves of (a) Polystyrene, and PS-TMOMMT nanocomposites with	

different TMOMMT content (b) 1.0 wt%, (c) 2.5 wt%, (d) 5.0 wt%, (e) 7.5 wt%, (f) 10.0wt%.....	87
Figure 35. DTG curves of (a) Polystyrene, and PS-TMOMMT nanocomposites with different TMOMMT content (b) 1.0 wt%, (c) 2.5 wt%, (d) 5.0 wt%, (e) 7.5 wt%, (f) 10.0 wt%.....	88
Figure 36. DTG curves of PS and PS-TMOMMT nanocomposites with different TMOMMT content in air atmosphere.....	89
Figure 37. DMA (storage modulus) curves of (a) Polystyrene, and PS-TMOMMT nanocomposites with different TMOMMT content (b) 2.5 wt%, (c) 5.0 wt%, (d) 7.5 wt%, (e) 10.0 wt%.....	90
Figure 38. Comparison of DMA results of (a) PS-TMDMMT, (b) PS-TMCMMT, (c) PS-TMTMMT, and (d) PS-TMOMMT nanocomposites with 5.0 wt% organo-MMT.....	91
Figure 39. Comparison of TGA results of PS, PS-P-C18 nanocomposite and PS-N-C18 nanocomposite.....	92

LIST OF SCHEMES

	PAGE
1 Nucleophilic substitution reaction for tetraalkyl phosphonium.....	93
2 Possible reaction mechanism (1) for tetraphenyl phosphonium.....	94
3 Possible reaction mechanism (2) for tetraphenyl phosphonium.....	95
4 Possible reaction mechanism (3) for tetraphenyl phosphonium.....	96

1. Objectives

The focus of this project is the determination of the relationship between the molecular structure and thermal stability (decomposition temperature, rate, and the degradation products) of organically modified clays. Modern thermal analysis techniques combined with infrared spectroscopy and mass spectrometry (TGA-FTIR-MS coupled with a GC/MS system) were used to obtain information regarding the weight changes and degradation products from the materials used in this study. Currently, there is a concern over the specific high-temperature (200-400°C) chemistry that occurs between these clays and polymers. It is highly probable that decomposition occurs and degrades the molecular structure during processing. Thus, the high temperature stability and degradation mechanisms of organically modified clays need to be determined. The effects of chemical variation (alkyl chain length and number of alkyls) of organic modifiers, the cation exchange capacity and morphology of clays, the electronic and counter ion variations, and nitrogen substitution in the clays on the thermal stability of organically modified clays was tested in this study. Finally, examination of the properties of clay-filled nanocomposites and the determination of the influence of clays on the matrix properties was explored.

2. Status of Effort

In the past three years, the detailed non-oxidative thermal degradation chemistry of montmorillonite and quaternary ammonium/phosphonium modified montmorillonite has been examined for the first time. In addition, the effect of the presence of nanoclays on the properties of polystyrene nanocomposites has also been addressed.

The initial degradation of the ammonium surfactant generally proceeds by a Hoffmann (β -elimination) process. However, when present in the montmorillonite, additional mechanisms, such as nucleophilic substitution, are observed. The multiple pathways are attributed to the chemically heterogeneous morphology of the layered silicate. Catalytic sites on the aluminosilicate layer reduce the thermal stability of a fraction of the surfactants by an average of 15-25°C. Depending on the analysis technique and procedure employed, the on-set temperature of non-isothermal degradation varies between 165 and 200°C. The release of organic compounds is staged and associated with retardation of product transfer arising from the pseudo two-dimensional morphology of the montmorillonite.

The initial degradation of the alkyl phosphonium modified montmorillonite (P-MMTs) follows potentially two reaction pathways – β -elimination [E_β] and nucleophilic displacement at phosphorus [$S_N(P)$] – reflecting the multiple environments of the surfactant in the silicate. Aryl P-MMT decomposition proceeds via either a reductive elimination through a five-coordinate intermediate or a radical generation through homologous cleavage of the P-phenyl bond. In conjunction with this, the thermal stability of the P-MMT depends to a greater degree on the architecture of the phosphonium surfactant than previously reported for N-MMTs. Additionally, the interlayer environment of the montmorillonite has a more severe effect on stability of the phosphonium surfactant than previously reported for ammonium-modified montmorillonite (N-MMT). Nonetheless, the overall thermal stability of P-MMT is higher than N-MMT.

The synthesis route for suspension polymerization was successfully developed and the synthesis parameters were optimized. The exfoliated Polystyrene-MMT (PS-MMT) nanocomposites were prepared and their properties were evaluated. The results of X-ray diffraction (XRD) and Transmission Electron Microscopy (TEM) indicated that exfoliated nanocomposites were achieved. The effect of organic modifiers (surfactants) on the properties of the synthesized nanocomposites was studied. It was found that polystyrene-MMT nanocomposite with 5.0 wt% of organo-MMT gave the greatest improvement in thermal stability, and polystyrene-MMT nanocomposites with 7.5 wt% of organo-MMT showed the greatest improvement in mechanical properties, compared with those of pure polystyrene (PS) under our experimental conditions. The alkyl chain length of the surfactant used in fabricating organo-MMT affects the synthesized PS nanocomposites, the longer the alkyl chain length that the surfactant has, the higher the glass transition temperature of the PS nanocomposite. However, the organoclay in the nanocomposites seems to play a dual role: (a) as a nanofiller leading to an increase of the storage modulus and (b) as a plasticizer leading to a decrease of the storage modulus. This results in a lower storage modulus of PS-TMOMMT and PS-TMTMMT nanocomposites than that of PS-TMDMMT and PS-TMCMMT nanocomposites.

In general, the fundamental degradation chemistry of organically layered silicates (OLS) was elucidated in this research work. The observations have implications about the understanding of factors impacting the interfacial strength between polymer and silicate and the subsequent impact on mechanical properties, as well as clarifying the role (advantageous or detrimental) of the decomposition products in the fundamental thermodynamic and kinetic aspects of polymer melt intercalation.

3. Accomplishments/New Findings

3.1. Materials Selection and Experimental

Synthesis of Organically Modified Montmorillonite (N-MMT and P-MMT)

Quaternary ammonium/phosphonium modified montmorillonites (N-MMT/P-MMT) were fabricated following conventional procedures by a cation-exchange reaction between the layered silicates and excess ammonium salts. In brief, the quaternary ammonium salt was added to a purified montmorillonite slurry. The mixture was stirred vigorously at 80°C for 24 hours. A white precipitate was isolated by filtration, then washed with a mixture of hot ethanol and deionized water until an AgNO_3 test indicated the absence of halide anions. The filter cake was then dried at room temperature, ground, and further dried at 70-80°C under vacuum for 24 hours. The final powder products (organically modified MMT) were then stored inside desiccators.

Synthesis of Polystyrene-Montmorillonite Nanocomposites by Suspension Polymerization

The polyvinylacetate (PVA) dispersion agent was dissolved in 400 mL deionized water at 80°C. The initiator, benzoyl peroxide (BPO), was first mixed with the styrene monomer at room temperature, and the organo-montmorillonite was then added into the mixture until well mixed. The mixture of styrene-BPO-organo-MMT was then added into

the PVA aqueous solution for the polymerization process. The solution was mechanically stirred and the reaction temperature was maintained at 80°C. After 8 hours of suspension polymerization, the precipitated products were filtered and then washed with deionized water. The polystyrene-MMT nanocomposites were obtained by drying overnight under vacuum at 50°C.

Thermogravimetric Analysis (TGA)

Thermogravimetric analysis (conventional and high resolution) was conducted with a TA Instruments TGA2950 (TA Instruments, New Castle, Delaware, USA) in an ultra high purity (UHP) nitrogen atmosphere, heating from room temperature to 1000°C (2°C/min for conventional TGA in the determination of the onset decomposition temperature). In addition, TGA experiments were also performed with a heating rate 1°C/min and 5°C/min for kinetic studies in the determination of the activation energy associated with mass evolution at different temperature stages. TGA measures the amount and rate of change in the weight of a material as a function of temperature or time in a controlled atmosphere. Measurements are used primarily to determine the composition of materials and to predict their thermal stability at temperatures up to 1000°C. High resolution TGA (HR-TGA) (TA Instruments, New Castle, Delaware, USA) was also employed in this study. HR-TGA differs from conventional TGA in that the heating rate is coupled to mass loss such that the sample temperature is not raised until the gaseous evolution at a particular temperature is completed. The instrument was calibrated following ASTM standard method E1582-93 before the sample test, using indium, tin, zinc, and silver as the calibration standards. The standard error, σ , for T_{onset} and T_{max} is 1.5 and 1°C, respectively.

Thermogravimetry (TG) Coupled with Fourier Transform Infra-red (FTIR) Spectroscopy (TG/FTIR)

The TG/FTIR system used consisted of a DuPont Instruments Model 951 Thermogravimetric Analyzer (TA Instruments, New Castle, Delaware, USA) interfaced with a Perkin-Elmer 1600 Fourier Transform Infrared Spectrometer (Perkin-Elmer Corp., Shelton, CT, USA). The Model 951 system has a horizontal quartz tube furnace which allows large amounts of samples to be placed in the furnace. A ball joint connection allows easy access for introducing samples. A custom-made heated connector prevents condensation of decomposition products. The ball and socket joints, and Teflon connector are wrapped with a heating coil which is controlled by a variable autotransformer. The samples are heated at a given heating rate from room temperature to the desired temperatures in either an inert gas such as ultra-high-purity nitrogen or an oxidizing gas such as air or oxygen. The purge gas (100 mL/min) flow carries the decomposition products from the TGA through a 70 mL sample cell with KBr crystal windows. The cell is placed in the IR scanning path for detection of the decomposition products and is kept at 150°C by a wrapped heating tape to prevent possible condensation. The IR detection ranges between 450 cm^{-1} and 4500 cm^{-1} . The detailed setup information is given elsewhere. [1]

Thermogravimetry (TG) Coupled with Mass Spectrometry (MS) (TG/MS)

The TG/MS system consists of a TA2960 TGA/DTA (TA Instruments, New Castle, Delaware, USA) interfaced with a Fisons VG Thermolab Mass Spectrometer (VG Gas

Analysis Systems, Cheshire, England) using a heated capillary transfer line. The sample is heated from ambient temperature to the desired temperature, under a flowing (100 mL/min) nitrogen (UHP grade) or air. The capillary transfer line was heated to 220°C, and the inlet port on the mass spectrometer is heated to 150°C. The capillary inlet (1.8 m) is constructed from fused silicon encased within a stainless-steel sheath. It is then covered with PTFE and then with a red fiberglass sheathing. Such construction allows for good mechanical strength and the means to resistively heat the long capillary line. Another major advantage of this interface is that it produces a partial pressure in the MS ion source proportional to that in the atmospheric pressure gas sample at the inlet probe. The Fisons unit is based on the quadrupole design with a 1-300 atomic mass units (amu) mass range. The sample gas from the interface is ionized at 70 eV. The system is operated at a pressure of 1×10^{-6} torr and this MS system is equipped with an NIST library database for MS analysis. The detailed setup information is given elsewhere. [1]

Pyrolysis Coupled with Gas Chromatography (GC) Coupled with Mass Spectrometry (MS) (Pyrolysis/GC-MS)

The Pyrolysis/GC-MS system consists of a LECO Pegasus II GC/MS system and a ThermEx™ Inlet System (LECO Corporation, St. Joseph, MI, USA). The Pegasus II GC/MS system includes a time-of-flight mass spectrometer (LECO Corporation, St. Joseph, MI, USA) and a HP 6890 High Speed Gas Chromatograph (Agilent Technologies, Palo Alto, CA, USA). The advantage of time-of-flight mass spectrometry is its potential for tremendously fast acquisition rates. By combining TOF technology, LECO's Pegasus II GC/MS achieves the fastest acquisition rate without loss of data integrity. The ThermEx™ Inlet System is designed to heat small quantities of solid samples in a quartz Pyrocell™ and transfer the volatilized sample components to a heated capillary GC injection port. The carrier gas connections and seals have been designed to provide a leak-free system for operation with the GC-MS system. The associated gas chromatograph has a capillary injector capable of operating in the split mode and an oven configured with a cryogenic option (liquid nitrogen). During the sample-heating period, evolved volatiles are condensed at the column head by maintaining the GC oven at cryogenic temperature. Once the sample has been heated to the desired temperature in the ThermEx™ system and all out-gassed components condensed at the column head, the cryogenic system is heated very rapidly to vaporize the components and inject them into the GC column for analysis. The GC capillary column used was DB-5 with a size of 10 m x 0.18 mm x 0.18 µm. The GC oven program was set as follows: ramp from 40°C to 325°C with a heating rate of 25°C/min and hold for 1 minute. The injection temperature was 275°C. The detailed setup information is given elsewhere. [1]

Differential Scanning Calorimetry (DSC)

Differential Scanning Calorimetry (DSC) is used to measure the temperatures and heat flows associated with transitions in materials as a function of temperature. DSC experiments were performed using a TA 2920 DSC (TA Instruments, New Castle, DE, USA) with heating from 0°C to 200°C at a rate of 5°C/min under flowing ultra high purity (UHP) nitrogen with a flow rate of 50 mL/min. The instrument was calibrated following ASTM standard methods E967-97 and E968-83 before the DSC experiments.

Thermomechanical Analysis (TMA)

Thermomechanical analysis (TMA) is used to measure linear or volumetric changes in the dimensions of a sample as a function of time, temperature, and force. This data provides valuable information about the coefficient of thermal expansion, glass transition temperature, and softening/melting temperatures. Thermal expansion and contraction behavior of polymer layered silicate nanocomposites were examined using a TA 2940 TMA (TA Instruments, New Castle, DE, USA) with a heating rate of 5°C/min from 25°C to 300°C. The expansion probe was employed in the determination of the coefficient of thermal expansion (CTE) of polymer samples. The instrument was calibrated following ASTM standard method E1363-90 before the TMA experiments.

Dynamic Mechanical Analysis (DMA)

Dynamic mechanical analysis (DMA) was used to measure the modulus (stiffness) and damping (energy dissipation) properties of materials as the materials deform under periodic stress. The mechanical properties (including storage modulus and loss modulus) of polystyrene/polystyrene-MMT nanocomposites were examined on a TA 2980 DMA (TA Instruments, New Castle, DE, USA). The samples were analyzed using a single cantilever clamp from 25°C to 300°C with a heating rate of 5°C/min at 1Hz.

Transmission Electron Microscopy (TEM)

The microstructure of nanocomposites was imaged using a JEM-100LX, JEOL Transmission Electron Microscopy (TEM) (JEOL USA, Inc., Peabody, MA, USA) under an accelerating voltage of 200 kV. The PS-MMT nanocomposite samples were sectioned into ultra thin slices at room temperature using a microtome equipped with a diamond knife and was then mounted on a copper grid for analysis.

Thermo-Infra-red Spectroscopy (Thermo-IR)

FTIR spectra of samples in pressed KBr pellets were recorded on a Perkin-Elmer 2000 series Infrared Spectrometer (Perkin-Elmer Corp., Shelton, CT, USA). The IR detection range was 450-4500 cm^{-1} with a resolution of 4 cm^{-1} . Data analysis was performed using GRAMS-2000 software (Thermo Galactic, Salem, NH, USA). Samples were prepared for FTIR spectrometry by mixing KBr and sample and at a mass ratio 50:1. The KBr was dried in a vacuum oven for 24 hrs before use. Both samples and KBr were ground into a fine powder using an agate mortar. Upon thorough mixing of samples and KBr powder, KBr-sample pellets with a 13 mm diameter were then prepared using a hydraulic press under 6 tons pressure.

X-ray Diffractometer (XRD)

Standard wide angle x-ray diffraction data was collected using a Thermo-ARL X'TRA X-Ray Diffractometer (XRD) (Thermo-ARL, Ecublens, Switzerland) with an intrinsic Peltier detector system using Cu K_α radiation. The powder samples were placed in a copper holder (25 mm x 25 mm^2), and scanned from 1° to 15° with a scanning rate of 1°/min. In-situ, high temperature x-ray diffraction experiments were also carried out on a Thermo-ARL X'TRA XRD diffractometer in a high temperature chamber with a heating rate of 5°C/min from 50°C to 400°C under vacuum conditions.

Molecular Weight Measurements

The polystyrene extracted from PS-MMT nanocomposites was examined with a Waters Model 150 Gel Permeation Chromatography (GPC) (Waters, Milford, MA, USA). Due to the presence of MMT, PS-MMT nanocomposites cannot be directly injected into the GPC system for molecular weight analysis. Therefore, polystyrene has to be extracted from PS-MMT nanocomposites before GPC analysis. The extraction process was conducted for 24 hours on a Soxtec extraction system (Tecator, Sweden) using tetrahydrofuran (THF) as the solvent. Molecular weights were calibrated by comparison to narrow molecular weight distribution (MWD) PS samples using eight standards from Polymer Laboratories.

3.2. Thermal Degradation Chemistry Of Quaternary Ammonium Modified Layered Silicates

Six alkyl quaternary ammonium chlorides ($R_3R'N^+Cl$ and $R_2R'N^+Cl$) were utilized to fabricate various quaternary ammonium modified montmorillonites (N-MMT) from a base Na^+ montmorillonite (cloisite Na^+ ; cation exchange capacity (CEC) = 92 meq/100 g; mean formula unit $Na_{0.65}[Al,Fe]_4Si_8O_{20}(OH)_2$, from Southern Clay Products, Inc.). The alkyl quaternary ammonium surfactants, mean molecular weights, milli-equivalent exchange ratios (MER), intended organic content and interlayer distance (d_{001}) of the OLSs are listed in Table 1. Coco, tallow and hydrogenated tallow quaternary ammonium surfactants are derived from natural products and are commonly utilized in commercial organically modified layered silicates (OLSSs). They consist of a mixture of quaternary ammonium salts with various lengths of saturated and unsaturated alkyl chains. The nominal compositions of these natural products are summarized in Table 2.

The N-MMTs were fabricated following conventional procedures by a cation-exchange reaction between the layered silicates and excess ammonium salts. In brief, the quaternary ammonium salt is added to purified montmorillonite slurry, the flocculated product is removed by filtration, dried and milled. Loss on ignition (LOI) results suggest that less than 5% unexchanged quaternary surfactant is present at the standard exchange level (MER = 95 meq/100 g of montmorillonite) generally used in this study. In some instances, subsequent washing of the OLSs consisted of slurring the exchanged montmorillonite in methanol, decanting and repeating for a total of three washings, or refluxing in ethanol in a soxhlet apparatus for 3-9 hours. The final organic content after washing with methanol corresponded to the CEC of the montmorillonite. However, soxhlet extraction of N-CoCo resulted in an organic content ~15% lower than CEC. This implies that the original exchange reaction was not complete (a fraction of Na^+ still remained within the interlayer) or that the washing procedure introduced a fraction of acidic protons which reduced the effective CEC of the aluminosilicate.

Characterization of Decomposition

In general, thermal degradation of the nanoscale organic-inorganic hybrid materials is a complex process. Initially, to qualify the organic decomposition processes, the general characteristics of pristine Na^+ montmorillonite and a representative alkyl quaternary ammonium montmorillonite was compared.

DTG (Derivative Thermogravimetry) curves of pristine montmorillonite and a typical alkyl quaternary ammonium montmorillonite (N-CoCo) are shown in Figures 1 and 2. The high-resolution (HR) DTG data further differentiate the various overlapping events. Note that because high-resolution TGA uses varying heating rates and effectively isothermal holds at a mass-loss event, decomposition temperatures, as defined by the peak in the DTG curve, will be lower than observed in conventional TGA.

Decomposition of the pristine montmorillonite corresponds to that given in previous reports, which generally identify two regions below 1000°C [2]. Free (absorbed) water residing between montmorillonite crystallites, and interlayer water residing between the aluminosilicate layers and comprising the hydration spheres of the cations evolve between 100-400°C [3, 4]. Between 500 and 1000°C, dehydroxylation of the aluminosilicate lattice occurs. In conjunction, the crystal structure has been observed to initially transform into spinel, cristobolite, mullite and/or pyroxenes (enstatite) [4]. At temperatures greater than 1300°C, mullite, cristobolite and cordierite were formed and subsequently melted at temperatures beyond 1500°C (mullite 1850°C, pure cristobolite 1728°C and cordierite ~1550°C) [5].

Thermal decomposition of the N-MMT (N-CoCo as an example here) is conveniently considered in four regions. Briefly, evolution of absorbed water and gaseous species occurs below 180°C (Region I). Organic substances evolve from 200°C to 500°C (Region II). Dehydroxylation of the aluminosilicate occurs from 500°C to 700°C (Region III) and evolution of products associated with residual organic carbonaceous residue occurs between 700°C and 1000°C (Region IV). Although conventional PLSN service environments would not include the temperatures in Regions III and IV, the complete degradation behavior of the OLS at these extreme temperatures has implications to the utilization of exfoliated OLSs as flame-retardant and ablation additives.

For both the organic-modified montmorillonite (N-CoCo) and the sodium montmorillonite (Cloisite Na^+) (MMT), the initial mass loss is dominated by water. For Cloisite Na^+ , release of water begins around 40°C, peaks at 62°C and continues until about 300°C. The HR-DTG curve resolves the lower temperature event into a two-step process (peak loss rates at 26°C and 57°C) with a third event at 288°C. This broad temperature regime reflects the numerous environments of water in montmorillonite. Weakly bonded, physiabsorbed water and free water pockets within the aggregate structure evolve at the lowest temperatures, while water within the interlayer and strongly bonded water of hydration (Na^+) evolve at progressively higher temperatures. In contrast, evolution of water and physiabsorbed gases in the N-MMTs (N-CoCo in this case) is generally complete by 40-60°C. The water is weakly physiabsorbed or associated with free water pockets within the aggregate structure. Note that although an OLS is conventionally considered hydrophobic because of the addition of alkyl ammonium cations, water absorption to aluminosilicate still occurs on the exterior of the aggregates and depends on environmental conditions, such as relative humidity. In this instance, approximately 1-2 wt% water is contained in the N-MMT powders. It is interesting to note that this concentration of polar additives has been shown to be sufficient to alter the intercalation response, implying careful attention to the initial water content of the OLS may be necessary for reproducibility in nanocomposite synthesis. [6]

At temperatures between 200 and 500°C, the organic constituent in the N-MMT begins to decompose, as seen in the TGA curve (Figures 3 and 4). Figures 3 and 4

summarize the DTG curves for the trimethyl alkyl montmorillonites (N-CoCo, N-Tallow, N-C12, and N-C18) and the dimethyl dialkyl montmorillonites (N-2CoCo, N-2HTallow and N-2C18). The overlapping DTG peaks for N-MMT at this temperature range indicate the release of organic substances is staged, arising from different mechanisms. In general, all the organic-modified montmorillonites decompose in a similar fashion. They exhibit three to four DTG peaks, a lower temperature event resulting in a sharp DTG peak around 200°C, and 2 to 3 closely overlapping higher temperature events producing a broad DTG peak between 300 and 400°C. Portions of the MS spectra of the evolution products from N-CoCo and N-C18 are shown in Figures 5 and 6. Water ($m/z = 18$), CO_2 ($m/z = 44$), $\text{NCH}_2(\text{CH}_3)_2$ ($m/z = 58$), alkene fragments ($m/z = 55, 69, 83$), and alkane fragments ($m/z = 57, 71, 85$) are evolved between 200 and 400°C. C-H vibrations at wavenumbers 2629, 2853, and 1478 cm^{-1} from TG/FTIR spectra (Figures 7 and 8) further illustrate the release of alkyl and alkene species at these temperatures. Additionally, as with the DTG experiments, the MS and FTIR results also indicate that the evolution of organic species is staged, as reflected by the overlapping peaks between 200 and 400°C. Furthermore, CO_2 ($m/z = 44$) evolution indicates oxidation of residual organic material within the N-MMT begins shortly after general mass loss via alkenes and alkanes and ends before general dehydroxylation of the aluminosilicate begins (as evidenced by the observation of H_2O ($m/z = 18$) from 500-900°C). Additional experiments on pristine montmorillonite indicate that the abrupt release of CO_2 at 400°C may also associate with a small fraction of insoluble metal carbonate impurities. Verification that complete removal of alkyl groups occurs before extensive dehydroxylation is provided by FTIR spectra of pyrolyzed N-CoCo (Figure 9) and N-C18 (Figure 10). After annealing at 500°C, the organic C-H vibrations (wavenumbers = 2629, 2853, 1478 cm^{-1}) disappear while OH vibrations (wavenumbers = 3690, 3620 and 1636 cm^{-1}) remain unchanged in frequency or relative intensity. Note that the absorbed water (wavenumbers = 3470 cm^{-1} and 1636 cm^{-1}) should be completely removed during the annealing process. However, the absorbed water vibrations can still be seen from FTIR spectra of annealed N-CoCo and N-C18, indicating the re-hydration behavior of OLS by quickly absorbing moisture from the atmosphere when it is exposed. Therefore, the pre-drying step is necessary to carefully control water content before the OLS is used for nanocomposite synthesis.

From 450°C to 700°C, dehydroxylation of the crystal lattice occurs for Cloisite Na^+ . TG-MS results have confirmed the major decomposition product for Cloisite Na^+ is water, which corresponds to numerous previous investigations of dehydration reactions in natural montmorillonite and smectites [7-9]. Determination of the break between the evolution of interlayer H_2O and structural -OH, though, is not always straightforward [10] (as illustrated in Figure 1), because molecular water can be bound at fairly high temperatures in defect structures and structural hydroxyl can be released at relatively low temperatures due to these same structural perturbations. The HR-DTG curve reveals a finite break as well as additional detail, indicating that dehydroxylation occurs in three major steps (445°C, 508°C, and 563°C), possibly reflecting the local environment of the crystallographic hydroxyls.

For N-CoCo, dehydroxylation and oxidation of the carbonaceous residue occur in two general events between 500 and 1000°C. As with the Cloisite Na^+ , HR-DTG further resolves the mass loss into discrete events, in this instance at least 6 events. TG-MS spectra (Figures 5 and 6) indicate water and CO_2 are evolved at the lower temperatures, implying carbonaceous residue from the alkyls factors into the dehydroxylation of the crystal lattice.

At the higher temperatures, an increased amount of CO₂ is released, beginning around 600°C and peaking at 800°C. Metallic species within the aluminosilicate potentially catalyzes a reaction between the carbonaceous residue and the oxygen in the crystal structure of the dehydroxylated montmorillonite, yielding CO₂ [11].

Onset Temperature of Surfactant Degradation

Processing of PLS nanocomposites, as well as the initial melt blending of the OLS and polymer, normally occurs in excess of 150°C and are near the thermal stability limits of the organic modifiers. The architecture of the quaternary ammonium ion is nominally chosen to optimize compatibility with a given polymer resin. However, its molecular structure also determines the thermal stability of the OLS. Not only will the thermal degradation of the organic modifier alter the carefully tailored surface compatibility, but also the resulting products may play a major and yet to be determined role in the formation of exfoliated nanostructures or the physical characteristics of the final PLS nanocomposites. Thus, the onset temperature and products of thermal decomposition from 150-350°C are key processing factors to ascertain the degree of chemical and structural change that occurs between room temperature characterized OLS and OLS within the final polymer nanocomposite system.

A reproducible procedure to quantify a temperature index for the thermal stability of the OLS and subsequent connection to the parent alkyl ammonium salt has yet to be developed and generally accepted. Normally, the temperature at a given mass loss or the temperature at the maximum rate of mass loss (peak in DTG) is used. However, overlapping events can introduce large uncertainties in the procedures. Furthermore, the later approach drastically overestimates the onset of chemical changes since it represents the temperature of greatest mass loss.

Table 3 summarizes various onset temperatures and temperatures at maximum mass loss for the N-MMTs. As an alternative to the conventional procedures, the onset temperature was also determined as the point where the derivative weight loss is 0.001%/°C over the value of the lower-temperature, steady-state, plateau (heating rate of 2°C/min in UHP nitrogen atmosphere). As with conventional approaches, low temperature evolution of small quantities of water and absorbed gases complicate determination of a lower temperature plateau region, increasing the uncertainty in determining the onset of organic decomposition. Thus after careful analysis of the volatiles by MS, a pre-drying step within the TGA (140°C isothermal hold for 60 min, followed by rapid cooling to 60°C before TGA analysis at 2°C/min) to remove water and absorbed gases was found to be useful in increasing the reliability of the onset temperature. The precision between experiments using this procedure is $\pm 1.5^\circ\text{C}$. In contrast, in absence of the pre-drying step, the onset temperatures were unrealistically low (120-140°C) because of evolution of physiabsorbed water. Note that the use of the temperature at maximum mass loss drastically overestimated the onset and that temperature was very sensitive to the heating rate. For example, the maximum mass loss for HR-TGA was 25-30°C lower than conventional TGA (e.g. Figures 1 and 2). However, the on-set temperature determined by the deviation of the DTG curve was comparable ($\Delta T \sim 3\text{-}5^\circ\text{C}$) to conventional TGA and HR-TGA.

Alone, TGA is of limited utility, since chemical identification of the volatiles is not possible. Used in conjunction with mass spectrometry, though, enables direct identification

of the release temperature of alkyl degradation products within a background of other gaseous volatiles. The initial fragment of quaternary ammonium degradation was found to be $m/z = 58$ ($NCH_2(CH_3)_2$) and was used as an additional index of the onset of organic decomposition. In general, this onset temperature is approximately 15-20°C higher than that determined by TGA, even though the heating rates in the experiments were identical (2°C/min). This underscores the general difficulty in using TGA alone to unequivocally identify the onset of degradation within a heterogeneous environment containing various mechanisms that produce or evolve volatiles at comparable temperatures, such as in the aluminosilicates where the quantity and stability of physiabsorbed water and gaseous products depend on prior process history.

Table 3 also summarizes temperatures associated with the higher temperature events. The DTG traces generally consist of a sharp peak (used to define T_{max}) superimposed on a broader peak (Figure 5). The relative location of the sharper event with respect to the broader events is sensitive to the heating rate of the experiment (Figures 1 and 2). The lowest derivative weight loss between the first and compound second DTG peaks (as well as the MS traces) was assigned as the onset temperature for these events. There is excellent agreement between the MS and TGA results.

Overall, irrespective of architecture (trimethyl or dimethyl), chain length, surfactant mixture, and exchanged ratio, the initial onset temperatures for decomposition of the surfactants within the N-MMTs are comparable (~155°C by DTG and ~175°C by TG-MS) with no apparent trends. This conservative estimate (non-isothermal, non-thermal oxidative) is relatively low compared to processing temperatures. Thus, idealized surfactant structures do not persist throughout the OLS, and thus the PLS nanocomposite, after temperature excursions approaching 180-200°C. However, it can not be stressed enough that property enhancements of PLS nanocomposites relative to the neat resins are commonly observed even though they have experienced temperature excursions greater than 180-200°C in processing and fabrication. Thus, the absolute role of the surfactant to the final PLS nanocomposite properties is not completely understood. Possibly, the property enhancements may even be greater if more stable OLSs were utilized.

As a final point, the overall stability of the surfactant decreases when intercalated into montmorillonite. Figure 11 shows the DTG for the four trimethyl alkyl quaternary ammonium salts used for N-CoCo, N-Tallow, N-C12, and N-C18 and the various on-set temperatures are summarized in Table 3. Overall, mass loss is very similar for these surfactants. Release of water from the surfactant structure (intercalated within the ionic region of the lamellar surfactant salt structure) occurs between 50°C and 100°C. Decomposition of the organic material occurs in one event between 200°C and 250°C, roughly corresponding to the lower temperature event in the N-MMT. Direct comparison of the thermal decomposition events of a N-MMT (N-C18) and the corresponding trimethyl alkyl surfactant (TMO) is depicted in Figure 12. The maximum rate of mass loss and on-set temperature for these surfactants are consistently 15-25°C higher than the first events in the N-MMT. This indicates that the Lewis or Bronsted acid sites in the aluminosilicate have a catalytic effect on the initial stages of decomposition of the organic within the N-MMT. Additionally, the single step decomposition of the surfactant salts in contrast to the multi-step process of the surfactant within the N-MMT implies that the presence of the nanoscopic

dimensions of the interlayer drastically influences reaction kinetics, product transfer and volatilization.

Initial Mass Loss of N-MMT

The initial mass loss event from the TGA experiments coincides with the upper temperature environments conventionally encountered by PLS nanocomposites. In contrast to the on-set temperature, the fraction of organic material evolved during the first event depends on certain aspects of the OLS, such as surfactant architecture, the MER and, especially, the degree of washing. Table 4 summarizes the mass loss associated with different temperature regimes, the total organic mass loss and the fraction of organic material evolved during the initial temperature event. Note that the experimentally determined organic content in the N-MMTs agrees within 1.0% percentage of what was anticipated from the MERs (Table 1). Conditioning the N-MMT either by Soxhlet extraction (N-CoCo-A, N-CoCo-B, N-CoCo-C) or repeated methanol washings (N-2HTallow-B1 and N-2HTallow-C1) significantly reduces the magnitude of the initial mass loss event. For example, Figure 13 compares the DTG curves for N-CoCo washed with ethanol via Soxhlet extraction, showing that the first event continually decreased with increased Soxhlet extraction. At first, it is tempting, especially on the basis of these TGA analyses of the N-MMT and alkyl ammonium chloride salts, to speculate that the initial event in N-MMT decomposition is associated with degradation of the excess surfactant above CEC that resides exterior to the layers. Removal of this surfactant by repeated washings and corresponding reduction in magnitude of the initial event would then imply that the intercalated surfactants are stabilized by confinement within the interlayer and degrade during the higher temperature events. However, further examination of the results indicates this initial hypothesis is not correct.

Comparison of layer repeat distance and total organic content indicates that the majority of the excess surfactant in these systems (i.e. equivalence of surfactant greater than the cation exchange capacity of the montmorillonite) is contained within the interlayer – not physiabsorbed in the exterior of the crystallites or contained in voids within the OLS aggregate structure. Figure 14 compares the interlayer spacing (x-ray diffraction) to the total organic content experimentally determined from TGA studies and predicted from MER. The linear correlation indicates that the majority of the excess surfactant resides within the interlayer, irrespective of architecture. This is consistent with previous investigations of OLSs with long chain quaternary alkyl surfactants [12], and the staging only occurs for shorter alkyl chains and lower interlayer surfactant densities [13-15]. Thus, for these preparation procedures, over-exchanged montmorillonites do not have a substantially greater fraction of surfactant residing outside the interlayer than do montmorillonites exchanged at equivalence. The surfactant molecules reside in the confined interlayer environment, whether directly associated with the aluminosilicate or a chloride anion.

Overall, the fraction of organic material released during the initial event is strongly correlated to initial interlayer spacing and surfactant architecture (Tables 1 and 3). For a given surfactant architecture, the initial fraction of organic material evolved decreases with the interlayer spacing of the OLSs. For example, interlayer spacing decreases with decreasing MER (N-2HTallow-A, N-2HTallow-B, N-2HTallow-C), shorter alkyls (N-C18 and N-Tallow; N-C12 and N-CoCo) or removal of surfactant in excess of CEC (methanol washing of N-2HTallow-B ($d_{001} = 3.25$) yielding N-2HTallow-B1 ($d_{001} = 2.50$)). These

correspond to a lower fraction of mass evolved in the first event. Additionally, a smaller fraction of mass is evolved from N-MMTs containing dimethyl than trimethyl surfactants (e.g., N-2HTallow-C and N-Tallow). Note that dimethyl N-MMTs generally have larger interlayer spacings than trimethyl N-MMTs, but a smaller fraction of organic material is evolved from the former in the initial event.

This overall behavior is consistent with the nanoscopic dimensions of the interlayer altering product transfer, product concentration, and thus the efficiency of secondary reactions, but not necessarily chemical stability of the intercalates. A smaller gallery height is expected to retard the rate of volatile evolution of the long chain decomposition products and thus decrease the fraction of mass detected in the first event. The larger number of long alkyl chains in the interlayer for dimethyl surfactants (two long chain alkyls per surfactant), relative to trimethyl surfactants (one long chain alkyl per surfactant), will result in a larger fraction of higher molecular weight products within the interlayer upon decomposition. This will also decrease the mean interlayer mobility, thus decreasing the rate of volatile release and detection, even though the interlayer spacing is larger. This picture is consistent with the similarity of on-set temperatures irrespective of surfactant architecture, initial MER or degree of washing. Thus, a detailed understanding of the morphology of the aluminosilicate and the decomposition products are critical in understanding the decomposition process of N-MMTs.

TGA and related techniques preferentially reflect decomposition events that produce volatiles. If the material structure, such as a thermally stable stacking of plates and associated nanoscale lamellar slits, inhibits or alters the release rate of volatiles, thermal decomposition events and detection of escaped volatiles do not necessarily have to coincide. Thus, the role of morphology and the decomposition products themselves need to be carefully examined in considering the implications of the initial mass loss event in the N-MMTs.

Structural Changes During N-MMT Decomposition

Alkyl salts are lamellar ionic crystals comprised of alternating layers of paraffinic alkyl chains and of ionic groups and associated water of hydration. Upon degradation around 200°C, the entire structure is rapidly and completely destroyed. In contrast, the layered morphology of aluminosilicate persists throughout the surfactant decomposition event, kinetically (and catalytically) altering the reaction pathway.

In situ x-ray diffraction of the decomposition process yielding the layer repeat distance (d_{001}) and the full-width-at-half-maximum (FWHM) of the basal reflection is summarized in Figures 15 and 16 for N-2HTallow-A and N-2HTallow-C. The FWHM is inversely proportional to the extent of layer registry through the Scherrer equation. The smaller FWHM, the narrower the peak reflection and the more ordered the layer stack. These dimethyl dehydrogenated tallow montmorillonites exhibit the same decomposition processes as previously discussed and differ only in the amount of surfactant present in the structure (MER = 140 for N-2HTallow-A and 95 for N-2HTallow-C). The majority of the excess surfactant resides in the interlayer (larger layer repeat distance, d_{001}) and results in a larger initial weight loss (Table 4).

The initial increase in layer repeat distance (d_{001}) and layer registry ($\propto FWHM^{-1}$) from 50-100°C is due to melting of the intercalated surfactant, which creates a fluid-like environment between the layers, enabling local relaxation of residual stress and packing

imperfections associated with prior process history. The melting behavior of the surfactant is also suggested from DSC data shown in Figure 17 (N-2HTallow-C). A strong exothermic transition at 50°C and a weak, broad exothermic transition at a temperature around 80-100°C are observed from DSC curve. The broad transition is associated with the loss of physiabsorbed water on the OLS surfaces, which disappeared upon re-heating. The strong transition, on the other hand, is attributed to 'melting' of the surfactants in the interlayers. In general, this behavior agrees with previous observations of other alkyl ammonium smectites [12, 16-17]. The slight increase in d_{001} from 100°C to 200°C is attributed to thermal expansion of the structure normal to the layers. From 200°C to 280°C, an increase in d_{001} and a decrease in layer registry (increase in FWHM) accompany the first OLS degradation event. These changes in the organization of the aluminosilicate layers reflect the production of volatiles and associated increase of internal pressure within the interlayer, leading to the expansion of the structure, layer disorder and potentially defect generation. This verifies that the initial decomposition event is not restricted to unconfined surfactant (i.e. external to the interlayer), but also includes intercalated, confined surfactant.

Note that the *in situ* observation that gallery height increases with decomposition contrasts with previous studies that indicate the gallery height decreases after decomposition. For example, previous studies of the structure of surface char on combusted nanocomposites revealed a collapse of layer spacing upon thermal decomposition of the hybrid structure [18]. Taken together, these studies indicate that the organization of the aluminosilicate layers appears to be, initially, disorder during thermal decomposition, and depending on the decomposition route and temperature, collapses to varying degrees after completion of volatile release. Thus, utilization of interlayer decomposition and production of volatiles to increase interlayer pressure, resulting in effectively increasing layer separation by gaseous expansion, provides a new, although unproven, paradigm for surfactant design for enhancing exfoliation in melt-processed polymer nanocomposites.

Degradation Products of N-MMTs

A list of products determined by pyrolysis/GC-MS from N-C18 during the 1st and 2nd thermal events and from TMO is summarized in Table 5. These are generally representative of the products from the other trimethyl alkyl OLSs and ammonium salts.

Degradation of TMO yields long chain tertiary amines, long chain alpha-olefins and 1-chloro alkanes. GC-MS at the beginning (200°C), maximum mass loss (250°C), and completion (300°C) of the decomposition process indicated that the same type of fragments (tertiary amines, alpha-olefins and 1-chloro alkanes) are presented throughout, with an increased number of shorter chain fragments at the higher temperatures. Decomposition of ammonium salts generally proceeds by a Hoffmann elimination reaction or an S_N2 nucleophilic substitution reaction. Hoffmann elimination occurs in the presence of a basic anion, such as a β -carbon of the quaternary ammonium, yielding an olefinic and a tertiary amino group [19, 20]. Nucleophilic attack at elevated temperatures of the chloride on R₄N⁺ favors the reverse of the quaternary ammonium synthesis, yielding RCl and R₃N. For neat TMO, the later is probably favored, although a fraction of olefins is detected.

For the OLS, the proximity of the Lewis base sites and the basic aluminosilicate surface to the intercalated alkyl quaternary ammonium molecule is conducive to enhancing (lowering the energy of) the Hoffmann elimination reaction, as seen by the lower on-set

temperature for the N-MMT and increased olefinic production. N-C18 contains unexchanged surfactant, as verified by the presence of 1-chloroalkanes in the degradation products. The additional presence of the branched alkanes implies auxiliary secondary reactions, such as olefinic addition, occur between products within the OLS, complicating a simple explanation of product generation based on the current observations.

During the higher temperature decomposition events of N-C18, long chain tertiary amines are observed along with shorter chain olefins, branched olefins, and aldehydes. Confined within montmorillonite's lamellar crystal structure, the initial products undergo successive secondary reactions, such as alkyl chain scission, free radical condensation, and additions to olefinic groups. The presence of oxygen and other metals in the structure of montmorillonite may serve as catalysts to enable the oxidative cleavage of alkenes to produce aldehydes at elevated temperatures.

To further understand the multi-decomposition steps related to the different decomposition products of organo-MMT, kinetic analysis of activation energy of each degradation step for N-C18 was conducted. The calculation of activation energy is based on TGA results for N-C18 with different heating rates (1°C/min, 2°C/min and 5°C/min). The detailed activation energy calculation procedure can be found in ASTM standard method E1641-99. The results suggested that the activation energy for the second series of events is 50-100 kJ/mole higher than the first event (156-162 kJ/mole). This is well in agreement with the GC-MS results where alkyl scission and condensation occur at high temperatures.

Summary

In general, the decreased stability, different decomposition products, and accompanying higher temperature events observed during N-MMT decomposition attest to the major role of the aluminosilicate chemistry and morphology in the thermal decomposition process of the organic intercalates.

Hindrance of molecular reorientation and mass transport within the nanoscopic interlayer will alter reaction kinetics and increase the transient concentration of products. These effects will enable alternative reaction pathways, secondary reactions, radical termination by the aluminosilicate surface and possibly increase the propensity for reverse reactions. Nyden and co-workers observed similar confinement effects on decomposition reactions within a slit using molecular dynamic simulations [21]. The fundamental stability of C-N linkage, though, will be determined less by the nanoscopic environment than by the local kinetic energy (reflected by the temperature), presence of catalytic species, and local concentration of co-reactants (such as O₂). The oxidative stability of a molecule may increase due to the role of confining morphology in modifying oxygen transport, but for the non-oxidative decomposition examined here, there is no reason *a priori* to suspect that localization of the surfactant within the interlayer will increase the thermal stability. For example, XRD data indicate that structural (and by inference chemical) changes occur within the interlayer during the first event. In actuality, the decrease in onset temperature of the OLSs relative to the ammonium salts indicates that catalytic sites on the aluminosilicate surface (whether at the layer edge or on the siloxane surface) decrease the stability of surfactant in close proximity to these sites.

Since the local environment does not increase the energetic stability of the alkylammonium, the elevated temperature events and the relative amount of mass loss during

the initial decomposition event must reflect the influence of the aluminosilicate structure on the reaction kinetics and the mobility of decomposition products. Overall then, a picture emerges as to the thermochemical events in the OLS and near the aluminosilicate surface as observed by analysis of volatile products.

Initial decomposition of the surfactant via Hoffmann elimination or nucleophilic substitution reaction occurs within and exterior to the interlayers at temperatures comparable to (or less than) the decomposition temperature of the pristine quaternary ammonium salt. The mass evolution occurring in the initial event originates from 'unconfined' surfactants, whether associated with the layers or small molecular anions. These "unconfined" surfactants reside outside the interlayers, such as those complexed at the exterior of the crystallites or within void spaces and inside the interlayers but within proximity of the terminus of the gallery. The onset observed will be directly related to the thermal stability of the surfactant and the catalytic influence of the aluminosilicate. The relative magnitude of the observed mass loss will depend on factors affecting mass transfer of the products, such as defect concentration, perfection of layer stacking, crystallite size and packing density of the aggregate. These factors, with the exception of layer size, are dependent on the processing history of the OLS. Furthermore, this implies that further examination of the initial decomposition process within the interlayers will require solid-state characterization techniques, such as *in situ*, elevated temperature FTIR spectrum of the solid, rather than analysis of the volatile product stream.

As the temperature increases, the higher molecular weight products that are trapped within the interlayers undergo further reactions (C-C scission, oxidation and dehydrogenation), radical cross-linking, or cyclization reactions. On average, increased temperature will favor production and increasing evolution of smaller molecular weight species and thus the additional higher temperature DTG peaks and associated lower molecular weight species in the mass spectrum and pyrolysis/GC results. Occurrence of these higher energy processes is further verified by the increased activation energy associated with mass evolution during these later events. Overall, these processes parallel those observed in petroleum cracking using MCMs (Multi-Chip Modules) and pillared clays [22, 23].

The implication of these conclusions to determine the thermal stability of N-MMTs in exfoliated PLS nanocomposites warrants comment. As previously mentioned, the magnitude of the initial mass loss detected by TGA reflects more the condition of the OLS crystallite structure than any chemical enhancement of thermal stability. Since an exfoliated OLS does not possess morphological features associated with the inorganic lamellar stack that would confine product transport, the non-oxidative thermal stability of the surfactants will at best be comparable to the stability of the parent surfactant if catalytic effects of the aluminosilicate are minimal. Along similar lines, the degradation species produced are expected to parallel those of the parent surfactant or those produced during the initial mass loss event of the OLS. Since the products observed during the higher temperature degradation events are related to retardation of degradation products and subsequent secondary reactions among products, they are not anticipated to be present in exfoliated PLS nanocomposites. Overall, the presence of long-chain alkane and alkene products from the decomposition of the surfactant may lead to detrimental interfacial plasticization or advantageous secondary cross-linking reactions (1-olefins and associated radicals) with the polymer. Determination of the

importance of these factors on the interfacial strength between polymer and silicate and subsequent impact on mechanical properties requires additional investigation.

Finally, verification that surfactant decomposition can occur at relatively low temperatures with respect to those conventionally used in melt processing implies that the interfacial energetics between the OLS and an intercalating polymer may be significantly different, and more complex, than originally intended by selection of the organic modifier for the OLS. Additionally, the production of non-tethered and long chain molecules, and of radical species that can form cross-links, increases the complexity of determining chain dynamics near the OLS surface and molecular interpretation of rheological phenomenon. Further investigation is crucial to clarify the role (advantageous or detrimental) of these small molecular products in the fundamental thermodynamic and kinetic aspects of polymer melt intercalation.

3.3. Thermal Degradation Chemistry Of Quaternary Ammonium Modified Layered Silicates

Optimal dispersion of the nano-constituents, such as montmorillonite (a commonly used layered silicate), in a polymer requires carefully chosen surface modification to lower the surface energy of the inorganic and impart organophilicity. For montmorillonites and comparable layered silicates, this is achieved via an ionic exchange reaction between the naturally occurring alkali metal cations residing between the aluminosilicate layers and alkyl-ammonium surfactants. However, the commonly used ammonium surfactants have limited thermal stability, in some cases less than the nominal processing temperature of the polymer resin. Furthermore, the interfacial chemistry at elevated temperature complicates fundamental studies attempting to establish specific requirements for the montmorillonite/surfactant/polymer interface that is necessary for optimal dispersion and property enhancements.

Phosphonium compounds are widely used as stabilizers in many applications and offer unique additional opportunities for polymer-layered silicate nanocomposites [24]. For example, mono- and bisphosphonium salts are used as flame retardants for textiles and paper, stabilization agents for polyacrylonitrile fibers to sunlight and heat, heat stabilizers for nylon and the condensation additives with organic dyes to wash-fast colors. Thus, the use of phosphonium salts as organic modifiers to layered silicates may further enhance the thermal and flammability properties of polymer nanocomposites.

Six quaternary phosphonium salts were used to fabricate phosphonium based organo-montmorillonites (P-MMT). Tributyltetradecyl phosphonium bromide was used as received from Cytec Industries, Inc.; other quaternary phosphonium compounds, including triphenyldodecyl phosphonium bromide, tributylhexadecyl phosphonium bromide, tributyloctadecyl phosphonium bromide, tetraphenyl phosphonium bromide, and tetraoctyl phosphonium bromide, were used as received from Aldrich, Inc. In addition, for the purpose of comparison, tetraoctyl ammonium bromide, received from Aldrich, Inc., was also used to fabricate the OLS.

Thermal Stability of P-MMTs

Non-isothermal decomposition of quaternary phosphonium modified montmorillonite (Figure 18), e.g. tetraoctyl phosphonium modified montmorillonite) can be conveniently

considered in four regions, overall similar to that observed for quaternary ammonium modified montmorillonite (Figure 18), e.g. tetraoctyl ammonium modified montmorillonite). Briefly, evolution of absorbed water and gaseous species occurs below 180°C (Region I). Organic substances evolve from 250°C to 500°C (Region II). Dehydroxylation of the aluminosilicate occurs from 500°C to 700°C (Region III) and evolution of products associated with residual organic carbonaceous residue occurs between 700°C and 1000°C (Region IV). The most important regions influencing the PLSN service environment are Region I and II, where the release of small molecules associated with fabrication and storage of the P-MMT or the evolution of decomposition products from the P-MMT may modify interfacial energies between the silicate and polymer.

Figures 19 and 20 summarize the derivative thermogravimetry (DTG) curves of two phosphonium surfactants (tetraphenyl phosphonium bromide and tributyloctadecyl phosphonium bromide) and six quaternary phosphonium montmorillonites (P-C12, P-C14, P-C16, P-C18, P-4Ph, P-4C8). Table 6 summarizes the relative mass loss at various temperatures for the modified montmorillonites. Although the decomposition temperature varies for the different phosphonium salts, single step decomposition is clearly observed. In contrast, the surfactant within the montmorillonite exhibits three to four discrete events in which the first event accounts for 30-50% of the total organic mass loss, dependent on the P-MMT. The multiple events are attributed to the nanoscopic dimensions of the interlayer which influences the reaction kinetics, product transfer and volatilization. For example, previous studies have shown that the rate and magnitude of the mass loss associated with the first event (first DTG peak) depend on process history, N-MMT morphology and excess surfactant [25]. However, this event does not simply reflect the quantity of excess surfactant since the relative mass loss is substantially greater than the amount of excess surfactant (1-2%). Overall though, the multi-events shown in the DTG curve should result from the complex interplay of process history and interdependence of the characteristics of the various decomposition events.

Table 7 summarizes the onset decomposition temperatures and the temperature at maximum rate of mass loss for the P-MMTs, using the procedure established in the previous study [25], which was detailed in the previous chapter. A pre-anneal at 140°C was necessary to remove physiabsorbed water and gases to ensure reproducible estimate of the onset decomposition temperature. The onset temperature and maximum rate of mass loss for the pure phosphonium surfactants are consistently 70-80°C higher than the first events in the P-MMT, as qualitatively observed in Figures 19 and 20. The decrease in the thermal stability of the surfactant has been attributed to the presence of Lewis and Bronsted acid sites within the aluminosilicate layer [25]. Note that these studies indicated that the onset decomposition temperature determined by the initial deviation of the DTG curve from baseline underestimates the decomposition onset determined by the initial appearance of decomposition products in the MS-TGA technique [25]. Furthermore, the onset decomposition temperature determined from the TGA experiment is dependent on the heating rate employed. The higher the heating rate that is used, the higher the onset decomposition temperature will be. Thus, qualitative comparison of onset temperatures necessitates similar experimental techniques and conditions, and these values serve as a lower-bound estimate for non-isothermal stability.

Figure 21 shows TG/MS results for P-C12. Water ($m/z = 18$), CO_2 ($m/z = 44$), alkene fragments ($m/z = 55, 69, 83$), and alkane fragments ($m/z = 57, 71$, and 85) are evolved between 300 and 500°C . As with the DTG studies, the staged evolution profiles for organic species evidenced by the overlapping peaks between 300 and 500°C were clearly observed. Furthermore, CO_2 ($m/z = 44$) evolution indicates the oxidation of residual organic within the P-MMT at high temperature ($\sim 600^\circ\text{C}$). The oxidation event is also confirmed by the evolution profile of H_2O with a peak at temperature around 600°C . For P-4Ph, an aryl quaternary ammonium modified MMT, the similar decomposition behavior was observed from TG/MS results, as seen in Figure 22. Aromatic fragments, such as $m/z = 76, 153, 154$, were evolved in the staged fashion, reflecting the three DTG peaks in the temperature range between 250 - 600°C in TGA results (Figure 20). The evolution of water and CO_2 at high temperatures (600 - 900°C) proves the presence of the oxidation reaction inside the MMT nanoscopic structure. Overall, TGA and MS results for P-MMTs are comparable with each other, both showing the staged degradation process for the intercalated organic modifier inside P-MMT. Moreover, the multi-step decomposition process observed in P-MMTs is in agreement with that from N-MMTs, indicating the effect of the presence of nanoscopic dimensions of the interlayer in OLS on the products decomposition, transport and volatilization.

Thermo-IR-spectroscopy was used to examine the structural evolution of P-MMT, providing complementary information to the TGA studies with regard to the chemical aspects of the solid residue. Figure 23 illustrates the temperature dependent IR spectrum profiles for P-C18. The absorption spectra of layered silicates have been broadly surveyed [26-28]. Briefly, structural OH groups exhibit absorptions at 3600 to 3700 cm^{-1} , whereas the water shows absorptions at lower frequencies, 3400 cm^{-1} and 1640 cm^{-1} . Frequencies between 1150 and 400 cm^{-1} are described as "lattice vibrations" [26-28]. The absorptions at 1062 and 1054 cm^{-1} is attributed to Si-O in-plane vibration. Absorption bands at $926, 896$, and 802 cm^{-1} are attributed to R-O-H bending vibration. The strong absorption in the region below 550 cm^{-1} arises principally from in-plane vibrations of octahedral ions and their adjacent oxygen layers [4].

For the aluminosilicate layer, the structural OH groups, apparent by the O-H stretching at 3675 cm^{-1} and R-O-H bending at $926, 896$, and 802 cm^{-1} , are resolved up to 500°C . The disappearance of hydroxyls is attributed to the destruction of the octahedral layer via dehydroxylation of the crystal structure [26-28]. Absorbed water content, associated with the broad absorption at 3400 cm^{-1} and 1640 cm^{-1} , gradually decreases with increasing temperatures and disappears at 250°C . Finally, bands observed between 3000 cm^{-1} and 2800 cm^{-1} (CH_2 and CH_3 stretching) and at 728 cm^{-1} ($(\text{CH}_2)_n$ rocking) which are associated with alkyl groups, decrease in intensity and disappear at around 450°C . For the aryl phosphonium modified MMT (e.g., P-4Ph), bands associated with aromatic rings, such as 3090 cm^{-1} (aromatic C-H stretching), $763\text{ cm}^{-1}, 730\text{ cm}^{-1}, 697\text{ cm}^{-1}$ (group frequencies of benzene derivatives – C-H out-of-plane vibrations), and $1620\text{ cm}^{-1}, 1500\text{ cm}^{-1}$, and 1456 cm^{-1} (group frequencies of aromatic ring – skeletal in-plane ring vibrations), are observed in the FTIR spectrum as shown in Figure 24. The intensity of IR bands from aromatic systems decreases with an increase in temperature, and these IR bands finally disappear around 450°C .

Note that alkane fragments with different length cannot be differentiated from temperature dependent thermal-IR spectra (Figure 23) since they all have the same C-H stretching and deformation frequencies. In addition, no C=C stretching vibration (1680-1620cm⁻¹) from alkenes (one of products from decomposition of surfactant) is observed from the IR spectrum. In contrast to the strong C-H absorption, the C=C stretching vibration gives rise only to weak bands in the infra-red in non-conjugated compounds (Bellamy, 1960). This, together with the relatively low local concentration of OLS (KBr:OLS = 50:1) which in turn produces even smaller amount of alkenes, results in insufficient resolution in the IR to pick out the C=C bond absorption.

The relative change in the absorbance of a band is proportional to the relative concentration of the chemical moiety. Figure 25 compares the DTG data for P-C18 to the relative change in the total area of the asymmetric and symmetric CH₂ and CH₃ vibrations (heating rate for both thermal FTIR and TGA experiments is 5°C/min). Note that since vibronic bands are broadened by increased temperature, the total area of the absorbance is more reflective of relative compositional change than the absorbance maximum. The thermal-IR results show a similar temperature dependent trend as the DTG data with an onset temperature of approximately 300°C (note that the heating rate is greater than discussed in Tables 6 and 7). Resolvable peaks in the FTIR spectra are present only up to ~ 400°C and are absent for the higher temperature events observed in the DTG. These higher temperature events account for ~50% of the organic mass loss, implying that the organic mass remaining after the first DTG event is carbonaceous residue devoid of alkanes. There is a substantial char yield for simple alkanes, again reflecting the influence of the nanoscopic dimensions of the layered silicate on the thermal degradation characteristics.

The subsequent decomposition of the carbonaceous char occurs during the higher temperature DTG events as well as during Region III and IV (see Figure 18). The relative amount of char retained above 500°C (Table 6: difference between percent mass loss from 120-500°C and percent total organic content) depends directly on the architecture of the phosphonium surfactant, where increased content of higher char-yielding aromatic moieties lead to greater char retention within the P-MMT at higher temperatures. Above 500°C, tributyl alkyl P-MMTs contain ~1-2%; tetraoctyl P-MMT contains ~8%; triaryl alkyl P-MMT contains ~22% and tetraphenyl P-MMT contains ~40%.

In situ x-ray diffraction of the decomposition process is shown in Figure 26 for P-C12 and P-C18. The initial increase in layer repeat distance (d₀₀₁) for P-C18 has been attributed to a melting transition of the intercalated surfactant between 70-100°C [12, 16, 17]. DSC results about the phase transition for both P-C18 (Figure 27) and P-C12 (Figure 28) are in very good agreement with the interlayer transition observed in XRD. An exothermic peak is clearly shown between 60-100°C, indicating the melting transition of intercalated surfactant. The additional DSC test on pure TBOPBr (used in fabrication of P-C18) further confirms that the surfactant is melted at a temperature around 70°C, as seen in Figure 29. The broad melting transition peak for surfactant inside the interlayers implies the disordered state of alkyl chains, and the possible presence of the defect rich packing alkyl chains. It is also noted that the magnitude of initial increase in d₀₀₁ for P-12 is relatively smaller than that for P-18. Previous FTIR and NMR studies [12, 16, and 17] indicate that short chain length and high temperature favor the disordered conformation. Therefore, the transition from an ordered conformation at room temperature to a disordered state at higher temperature is more

noticeable for P-18C than for P-12C, resulting in a more obvious increase in d_{001} between 70–100°C. The temperature dependence $\nu_{as}(CH_2)$ and $\nu_s(CH_2)$ from *in situ* FTIR results of P-C18 also confirmed the above observation (Figure 38). In general, the frequency of $\nu_{as}(CH_2)$ is sensitive to the gauche/trans conformer ratio [29–32], and the shifts in the CH_2 stretching band largely reflect changes in chain conformation, with the frequency shifting from lower frequencies for ordered, all-trans chains, to higher frequencies as the chain disordered (gauche/trans conformer ratio) increases [11]. Increased gauche conformations (increased disorder) lead to a more liquid-like state. Figure 30 shows the temperature dependence of $\nu_{as}(CH_2)$ and $\nu_s(CH_2)$ for P-C18. Clearly, as the temperature increases the frequency of the center of the peak shifts from low wavenumber (liquid-crystalline state) to higher frequencies before it finally reaches a plateau with a frequency approaching that of a liquid-like state.

Above 100°C, gallery height increases monotonically to ~370°C, which is comparable to the maximum rate of mass loss in TGA experiments and maximum rate of absorption change in FTIR experiments. Above 370°C, the gallery height starts to decrease with increasing temperatures, indicating the collapse of the interlayer gallery. This is substantially higher than the onset thermal decomposition temperature but comparable to the temperature of maximum rate of mass loss. These results suggest that the products from the initial decomposition process are retarded and trapped and that the restriction of volatiles suffices to create an internal pressure that maintains the interlayer distance even though mass is evolving.

Thermal Degradation Mechanism of P-MMTs

Pyrolysis products determined by pyrolysis/GC-MS from P-18C, P-4Ph and their corresponding phosphonium salts at temperatures of 250°C, 300°C, 350°C and 400°C are summarized in Tables 8 and 9. A step-by-step degradation pathway can be derived from the product distribution at the different temperatures. The decomposition behavior of the alkyl phosphonium montmorillonites, such as P-12C, is very similar to that of P-18C.

On account of the greater steric tolerance of the phosphorus atom and the participation of its low-lying d-orbitals in the processes of making and breaking chemical bonds, phosphonium salts are generally capable of undergoing a wider range of reactions and behave differently than their ammonium counterparts toward an external base (B). The following types of reactions have been established for tetraalkyl phosphonium salts under appropriate conditions, Scheme 1 [33]. (1) Nucleophilic substitution reaction at the α -carbon center, $[Sn(C)]$, where the attendant nucleophilic anion (e.g., halides) displaces the triphenylphosphine group. This is effectively the reverse of the quaternization reaction [34]. Since there is a change in oxidation state for the reactant (P at +5 oxidation state) to the product (P at +3 oxidation state), this reaction can also be regarded as a reductive elimination process. (2) β -elimination [35], E_β , where the β -proton is abstracted by a base in concert with the expulsion of triphenylphosphine from the α -carbon. (3) Substitution at phosphorus [36], $[Sn(P)]$, where an hydroxyl anion attacks the phosphorus center to form a five-coordinate intermediate, followed by comconitant separation of a phosphine oxide and an alkane. This reaction is primarily driven by the formation of a strong phosphoryl (P=O) bond. (4) α -elimination [37, 38], E_α , which is actually an α -proton abstraction process and the basis for the synthetically useful reaction for converting carbonyl compounds to olefins (Wittig reaction). Typically, this reaction requires a strong base such as alkyllithium or

aryllithium reagents. Thus, reactions (1)-(3) are most likely to occur as the primary processes during the thermal decomposition of quaternary phosphonium compounds either in neat state or intercalated within montmorillonite. Indeed, the pyrolysis/GC-MS of neat phosphonium salts indicated that both $[S_N(C)]$ and E_β elimination reactions are involved, confirmed by the presence of both alkenes and alkyl (or aryl) halides in the pyrolysis products. However, the $[S_N(C)]$ reaction is probably more favored in neat phosphonium salts, since the initial attack of the halide anion on the β -hydrogen is unfavored [39, 40].

Similar to the pristine salts, tertiary phosphine and long-chain olefins are observed as the decomposition products from the alkyl P-MMTs (e.g., P-C18), but at lower temperatures (250°C vs. 300°C). This indicates the occurrence of β -elimination mechanism upon degradation of P-MMT. Additionally, phosphine oxide and octadecane are also detected from P-C18, consistent with the $[S_N(P)]$ pathway associated with hydroxyls along the sheet edge. The absence of alkyl halides indicates that the $[S_N(C)]$ reaction is suppressed by the removal of the bromide anion and replacement by the aluminosilicate sheet. The neat negative charge of the aluminosilicate is dispersed over numerous bridging oxygens, depending on the crystallographic location of the isomorphic substitution [41, 42]. The weak Lewis basicity of the siloxane surface is thought to be insufficient to drive the $S_N(C)$ reaction.

In the case of tetraphenyl phosphonium, the primary thermal degradation mechanisms are expected to be different from the reaction pathways discussed above for the tetraalkyl analogs because of the following two reasons. First, the absence of α -hydrogen in the phenyl substituents precludes the occurrence of an α -elimination process. Secondly, the β -elimination process necessitates the formation of benzene whose formation is not favored energetically and requires the presence of a base much stronger than a hydroxide anion. Furthermore, at temperatures $>300^\circ\text{C}$, reaction pathways involving reactive intermediates, namely free radicals, are more probable. Thus, in the case of the neat salt, two possible reaction mechanisms may lead to the formation of bromobenzene, biphenyl, and triphenylphosphine as the thermal decomposition products. The first mechanism invokes the intermediacy of five-coordinate bromotetraphenylphosphorane (Scheme 2) that rapidly undergoes reductive elimination to form the resultant products that were observed except PPh_2Br , which may be unstable under the conditions and dissociate into a PPh_2 radical and a Br atom. Both can combine with phenyl radicals to form triphenylphosphine and bromobenzene. The second mechanism involves the homolysis of P-phenyl bond to generate triphenylphosphonium radical and phenyl radical, which can subsequently combine with either another phenyl radical to form biphenyl or a bromine atom to form PhBr (Scheme 3). The bromine atom is produced from the reduction of the triphenylphosphonium radical to triphenylphosphine by the attendant bromide.

Similar primary reaction mechanisms involving free radicals may be occurring when the tetraphenyl phosphonium is intercalated into montmorillonite. This is based on the fact that the expected products (PPh_3 and biphenyl) are observed in the temperature range of 250-350°C. In addition, the fact that benzene and phenol were not observed among the thermal degradation products lead us to propose an additional pathway as depicted in Scheme 4 to explain the generation of triphenylphosphine oxide. In essence, this pathway is similar to the $[S_N(P)]$ pathway described before for the tetraalkylphosphonium salts except that the phenyl substituent migrates to a silicon on the edge or at a defect site on the surface of montmorillonite with the concomitant release of triphenylphosphine oxide. Rapid homolytic

cleavage of Si-phenyl bond generates the phenyl radical and a silicon-based free-radical on the montmorillonite. The recombination of two phenyl radicals results in biphenyl product and the latter immobilized free-radical can conceivably reduce the nearby triphenylphosphonium radical to triphenylphosphine. Although the phenyl-migration step is driven by the formation of the phosphoryl bond, it occurs at higher temperatures ($\geq 300^{\circ}\text{C}$) because the Si-O bond (111 Kcal/mol) is relatively strong in comparison to the P=O bond (~130 Kcal/mol) [43] formed. The need to form a P=O bond in order to energetically compensate for the breaking of strong Si-O bond also provides the rationale for the migration of the phenyl group to silicon instead of to oxygen. The migration of the phenyl group to oxygen has been documented in the solution reaction of triphenylalkylphosphonium iodides ($\text{Ph}_3\text{PR}^+ \text{I}^-$) with methoxide, resulting in the isolation of Ph_2PR and PhOMe (anisole) [44]. The absence of phenol among the thermal degradation products lends support to the proposed phenyl-migration step.

As the temperature increases (400°C), shorter tertiary phosphines are observed along with shorter chain olefins, branched olefins, and aldehydes. This implies that after the initial decomposition step the evolved products, which are confined inside the montmorillonite's lamellar crystal structure, undergo additional and successive secondary reactions (olefinic addition, alkyl chain scission, and condensation) at higher temperatures. Furthermore, oxygen and other metals in the structure of montmorillonite may serve as catalysts to enable the oxidative cleavage of alkenes to produce aldehydes.

Summary

The decreased thermal stability, staged decomposition process and different products imply that the thermal decomposition process of phosphonium cations within the montmorillonite follows multiple reaction pathways due to the catalytic and morphological effects of the aluminosilicate matrix. In general, the non-isothermal decomposition behavior for P-MMT and N-MMT share similar characteristics. β -elimination and nucleophilic substitution occur in both cases. Additionally, the multi-step decomposition implies that the presence of the nanoscopic dimensions of the interlayer greatly affects the reaction kinetics and product transfer, ultimately resulting in a substantial carbonaceous yield. The major difference of the thermal decomposition behavior between P-MMT and N-MMT is that maximum rate of mass loss and onset temperature for the phosphonium surfactants are consistently $70\text{--}80^{\circ}\text{C}$ higher than the initial decomposition temperature in P-MMT, whereas only a $15\text{--}25^{\circ}\text{C}$ difference is observed between ammonium surfactants and N-MMT, indicating that the influence of the layered silicate is more substantial for phosphonium than for ammonium surfactants. At this point, there are insufficient data to specifically ascribe the observed catalytic effect to translational confinement or to specific crystallographic sites or defects in the aluminosilicate. Previous work showed that when the anion of the phosphonium was hydroxide, the first products of pyrolysis were detected at lower temperatures than when halides were anion [45]. This phenomenon was attributed to the formation of the highly stable P-O bond (phosphine oxide). The ammonium salts, however, cannot decompose by a substitution mechanism to produce amine oxide because the nitrogen atom has no vacant d orbitals of energy low enough to form a five-coordinate intermediate. As a result, phosphonium salts can be more easily attacked by edge OH and thus more susceptible to catalytic effects than ammonium salts.

Nevertheless, higher thermal stability was observed for P-MMT compared to N-MMT, irrespective of the additional effects of the aluminosilicate. Since the thermal stability of exchanged MMT is related to the thermal stability of the parent salts, the much higher initial decomposition temperature of the parent phosphonium salts, compared to the ammonium salts, compensates for the loss due to the influence of the aluminosilicate.

In contrast to previous studies on N-MMTs, the architecture of the phosphonium cation is reflected in the thermal stability of the P-MMTs. Comparison of P-C14, P-C16, and P-C18 indicates that the alkyl chain length does not influence the thermal stability of corresponding P-MMTs (Figure 20, Table 7), paralleling previous observation from alkyl N-MMTs and in agreement with the anticipated decomposition reactions. However, the stability of a longer chain, symmetric alkyl P-MMT, such as P-4C, is $\sim 30^{\circ}\text{C}$ greater than that of tributyl alkyl phosphonium MMTs, even though the stability of the salt is only slightly greater ($0\text{--}5^{\circ}\text{C}$). Similar dependence on architecture is not observed for N-MMTs. The initial decomposition temperature for tetraoctyl quaternary ammonium modified montmorillonite (N-4C8) and the corresponding salt is similar to other trimethyl alkyl ammonium MMTs and salts [25]. The increased stability of P-4C8 probably reflects increased steric effects around the P center, inhibiting the bimolecular reactions at the P [$\text{S}_\text{N}(\text{P})$] or the β -C [E_β]. The substantially greater stability of the tetraaryl phosphonium arises from the alternative decomposition pathways. When alkyl and aryl phosphonium are present, such as for triphenyl alkyl montmorillonite (P-C12), lower stability ($\sim 20^{\circ}\text{C}$) relative to tetraaryl phosphonium is observed. Nonetheless, the thermal stability of alkyl-aryl P-MMT is $\sim 15^{\circ}\text{C}$ greater than that of alkyl P-MMTs. The steric hindrance provided by the phenyl group is probably the major contributor to this behavior. Alternatively, the possibility of $\text{p}\pi\text{-d}\pi$ interactions between the P and phenyl groups, resulting in the delocalization of the positive charge, can also diminish the susceptibility of the alkyl chain to β -elimination, increasing the thermal stability of P-C12.

Overall, four distinct interlayer environments are present between room temperature and the temperature at which the interlayer collapses, and the latter is divided into two regions described by DTG. From room temperature to 70°C , the interlayer contains solid-like, paraffinic surfactants (i) [12]. Subsequently, melting of the long chain alkyls results in a dynamic, liquid like interlayer (ii). Depending on the chain length, architecture, and surfactant density the first environment may not occur. At temperatures around 200°C , decomposition of the surfactant begins in the vicinity of the P (or N), resulting in an interlayer containing small volatile and long chain molecules that are not associated with the aluminosilicate layer (iii). Finally, complete evolution of decomposition products at temperatures in excess of $350\text{--}380^{\circ}\text{C}$ leads to gallery collapse and the retention of a substantial fraction of organic mass as carbonaceous char (iv).

The presence of environment (iii) and (iv) is not well documented in the literature. The creation of mobile products, from the surfactant initially translationally confined within the interlayer, may provide an additional entropic driving force for polymer intercalation. In contrast, the disappearance of the compatibility between the aluminosilicate and polymer will inhibit polymer inclusion. The role of these products in nanocomposite formation has not been considered and future studies are needed. Furthermore, in some instances the decomposition products, such as the acidic proton arising from β -elimination, may serve to further degrade other organic moieties near the aluminosilicate surface, effectively creating a

self-catalyzing decomposition. Finally, the enhanced carbonaceous yield must influence the self-passivation response [46, 47] and enhanced flammability [48] characteristics of PLSNs. Minimal information is available on the impact of layered silicate morphology, whether simply an organically modified layered silicate or the modified layered silicate is dispersed in a polymer, on the extent to which the carbonaceous yield is enhanced.

Overall, the superior improvement in thermal stability for P-MMT compared to N-MMT, along with the well-known properties of phosphorus compounds, such as flame retardancy and heat stabilization, are advantages to the utilization of P-MMT in various polymer nanocomposites. In contrast to N-MMTs, the degradation pathways and thermal stability depend on surfactant architecture. However, the stability is substantially decreased (70-80°C) with respect to that the parent phosphonium salt. Thus, further studies of the specific influence of the interlayer environment and aluminosilicate surface on reaction pathways are needed.

3.4. Synthesis and Characterization of Polystyrene-Organo-Montmorillonite Nanocomposites Prepared by Suspension Polymerization

Suspension polymerization is a commonly used method for free radical polymerization of vinyl monomers. Here, PVA was used as a dispersion agent, which can surround the styrene monomer, BPO, and organically modified montmorillonite in the deionized water environment, as shown in Figure 31. The mixing procedure for organo-MMT is critical for obtaining the homogeneous nanocomposite products. Initially, organo-MMT was dispersed into the aqueous phase with PVA first before the mixture of monomer and then BPO was added into the aqueous phase for polymerization. However, it was found that two-phase products were produced. One phase contained polystyrene only as the homopolymer product. The other phase, on the other hand, contained both polystyrene and organo-MMT as the PS-MMT nanocomposite product. It is believed that some of the styrene monomer did not have enough time to interact with organo-MMT during the polymerization process since organo-MMT was dissolved into the aqueous phase first. To improve the interaction between styrene monomer and organo-MMT, organo-MMT was dispersed into the organic phase, monomer-BPO solution, instead of the aqueous PVA solution. This change resulted in a great improvement in the homogeneity of the PS-MMT nanocomposite. The final product was a truly single-phase polystyrene-MMT nanocomposite, confirmed by TGA, TEM, and XRD techniques.

The typical polymerization procedure first involves the dissolution of the dispersion agent (PVA) in 400 mL deionized water at 80°C under constant stirring. Subsequently, a mixture of benzoyl peroxide (BPO) initiator, styrene monomer, and the organo-montmorillonite, which is pre-mixed at room temperature, was added into the PVA solution for polymerization. The mixture solution was mechanically stirred and the reaction temperature was maintained at 80°C. After 8 hours of suspension polymerization, the precipitated products were filtered, washed with deionized water, and then dried under vacuum overnight at 50°C.

One of the important experimental parameters is the mole ratio of monomer and initiator. If there is too much initiator used in the synthesis experiment, the chain length of polymer will be small, resulting in a low molecular weight polymer. However, if there is not

enough initiator in the polymerization solution system, longer experiment time will be required to finish the polymerization process. In order to synthesize the polymer-MMT nanocomposites with the proper molecular weight in a reasonable experimental time range (4 hrs to 8 hrs), various monomer and initiator mole ratios were employed and tested in the preliminary experiments. It was then found that the mole ratio of 100:1 (monomer to initiator) gave the best results in our experimental conditions. Therefore, the monomer-to-initiator-mole ratio of 100:1 was employed in all suspension free radical polymerization experiments in this study. GPC results shown in a later section confirmed that the suspension free radical polymerization experiments conducted in this study is consistent, giving a relatively high MW and good polydispersity index.

Four alkyl quaternary ammonium chlorides ($R_3R'N^+Cl^-$, used as received from Akzo Nobel Chemicals, Inc.), trimethyldodecyl quaternary ammonium chloride (TMD), trimethyloctadecyl quaternary ammonium chloride (TMO), trimethylcoco quaternary ammonium chloride (TMC), and trimethyltallow quaternary ammonium chloride (TMT), were utilized to fabricate various organically modified layered silicates (OLS) from a base Na^+ Montmorillonite (Cloisite Na^+ , cation exchange capacity, CEC = 92 meq/100g, Southern Clay Products, Inc.). Tributyoctadecyl phosphonium bromide was also used in fabricating P-MMT which was then used for synthesizing the PS nanocomposite. Poly(vinyl alcohol) (PVA) (MW = 77,000~79,000), benzoyl peroxide (BPO), and styrene monomer were obtained from Aldrich Co., Ltd. All of the above materials were used as received without any further treatment.

The Effect of MMT Content on the Properties of PS-MMT Nanocomposites

The suspension polymerization was used to synthesize polystyrene-organo montmorillonite (PS-MMT) nanocomposites. PVA is a dispersion agent, which can surround styrene, BPO and organophilic montmorillonite in the deionized water (Figure 31). Polymerization occurs inside the PVA vacuole, and the PS-clay nanocomposite is the powder products. Figure 32 illustrates the XRD pattern of PS-TMOMMT and PS-TMCMMT nanocomposites with 5.0 wt% organo-MMT content. There are no MMT peaks identified from both PS-MMT nanocomposites, suggesting that either the MMT silicate sheets were exfoliated in PS-MMT nanocomposite or because of a much too large spacing between the layers (i.e. exceeding 8 nm in the case of ordered exfoliated structure). However, the silicate exfoliation is confirmed and supported by TEM micrographs as seen in Figure 33a and 33b. Clearly, PS-TMOMMT (Figure 33a) and PS-TMDMMT (Figure 33b) nanocomposites show a well dispersed (exfoliated) although some 2-3 layer stacks can still be observed in TEM micrographs. A similar exfoliated structure can also be observed for PS-TMCMMT and PS-TMTMMT nanocomposites.

Table 10 summarized the results of PS-TMOMMT and PS-TMDMMT nanocomposites containing varying amounts of organo montmorillonite. It was found that both the yield and the activity increased with the increase of clay content in the nanocomposite. However, after the organo montmorillonite contents increased to 10.0%, both the yield and the activity decreased. The organo montmorillonite content also affects the glass transition temperature (T_g) and decomposition temperature (T_d) of PS-MMT nanocomposite, which will be discussed in detail in the following section.

Figure 34 shows the comparison of DSC result of pure PS and of PS-TMOMMT nanocomposites. The glass transition temperature (T_g) of pure PS occurs at 91°C. Clearly, with the increase of organo-MMT content up to 5.0 wt%, T_g of the nanocomposite increases. However, the T_g of the nanocomposite decreases to 100.8°C when the organo-MMT content increases to 7.5 wt% and continues to decrease to 92.8°C when the organo-MMT content reaches 10.0 wt%. The increase in T_g is tentatively ascribed to the confinement of the polymer chains adjacent to MMT interlayers that prevent the segmental motion of the polymer chains. On the other hand, the apparent decrease in T_g when organo-MMT loading is at 7.5 and at 10.0 wt% may be attributed to the high viscosity of organo-MMT-styrene dispersion that affects the diffusion of initiator molecules and chain propagation during polymerization. The phenomenon of T_g decrease in a high organo-MMT loading nanocomposite system was also observed by Fu and Qutubuddin [49]. Similar trends can also be observed from PS-TMDMMT nanocomposites as detailed in Table 2. With increase of TMDMMT content, the T_g of nanocomposites increases from 92.5°C with 1.0 wt% TMDMMT to 94.8°C with 5.0 wt% TMDMMT. However, further increase in TMDMMT leads to a decrease in the T_g to 92.7°C with 7.5 wt% TMDMMT loading and 89.8°C with 10.0 wt% TMDMMT loading.

An important characteristic of polymers is their stability at elevated temperatures. Figure 35 shows TGA results of the pure PS and the PS-TMOMMT nanocomposites in a nitrogen atmosphere. Thermal degradation of PS and PS-TMOMMT nanocomposites proceeds in a single step. The content of TMOMMT has a large influence on the decomposition temperature. In general, all PS-TMOMMT nanocomposites have a higher decomposition temperature in a nitrogen atmosphere than the virgin PS, and the nanocomposite with a 5.0 wt% of TMOMMT has the highest decomposition temperature among the five PS-TMOMMT nanocomposites. When TMOMMT content increases to 7.5 wt% and 10.0 wt%, the decomposition temperature of PS-TMOMMT decreases slightly. The influences of organo-MMT content on the decomposition temperature can also be indicated by the data from PS-TMDMMT nanocomposites summarized in Table 10. Similar to PS-TMOMMT nanocomposites, the peak decomposition temperature for PS-TMDMMT nanocomposites increase with an increase of TMDMMT content up to 5.0 wt%. However, with further increase in TMDMMT content to 7.5 and 10.0 wt%, the peak decomposition temperature starts to decrease, although the T_d (in nitrogen atmosphere) for nanocomposites with a 10.0 wt% organo-MMT content still illustrates an increase compared to the virgin PS. Overall, an increase of 10-20°C was observed in the decomposition temperature in a nitrogen atmosphere for PM-MMT nanocomposites, depending on the various organo-MMT contents.

In contrast to the behavior in nitrogen, PS-MMT nanocomposites illustrated a different degradation behavior in an oxygen atmosphere. As shown in Figure 36, PS-TMOMMT nanocomposites appear to decompose in two steps, a broad DTG peak between 300-370°C and a sharp DTG peak at around 395°C super-imposed on the broad DTG peak. Note that the pure PS still decomposes in one step with a peak temperature at 363°C. This implies that the presence of interaction between TMOMMT and PS serves to stabilize the nanocomposite. The formation of the ammonium clays char during the degradation process may play a key role here to retain the polymer and delay the polymer degradation. Recent studies in the fire performance of Polystyrene and Poly(methyl methacrylate) nanocomposites indicate a silicate layer reassembles into a multilayer char after the polymer

burns away [50, 51]. The suggested clay nanocomposites function mechanism involves the formation of a char that serves as a barrier to both mass and energy transport. It was also noted that the increase in the T_d in an air atmosphere is greater than that in a nitrogen atmosphere for PS-MMT nanocomposites compared to the virgin PS, with a 30-35°C increase in an air atmosphere vs only 10-20°C increase in a nitrogen atmosphere. This further shows the nanoscale silicate layers not only act as mass transport barriers to prevent out-diffusion of the volatile decomposition products, but serve as insulators to slow the energy transport.

Dynamic mechanical analysis (DMA) was used to measure the viscoelastic properties of PS-MMT nanocomposites as a function of temperature. In this measurement the in-phase and out-of-phase components of the stress are measured while a sinusoidal strain is applied to the sample. From the in-phase and out-of-phase components the storage (E') and loss modulus (E''), respectively, can be calculated. The ratio $E''/E' = \tan \delta$ is a measure of the energy lost to the energy stored per cycle of deformation and has a maximum at the thermal transition. Figure 37 illustrates the temperature dependence of the storage modulus for pristine PS and PS-TMOMMT nanocomposites with different TMOMMT content. With an increase in TMOMMT content E' increases significantly, as expected. At 25°C, there is about a 15% increase in storage modulus for PS-TMOMMT with 1.0 wt% of TMOMMT, and about 106% increase for PS-TMOMMT with 7.5 wt% of TMOMMT. Interestingly enough, the storage modulus of the nanocomposite decreases when the TMOMMT content reaches 10.0 wt% compared to that with 7.5 wt% TMOMMT, and has only about 20% increase compared to that of pure PS. This may be attributed to the dispersion of organophilic MMT in PS affecting the diffusion of initiator molecules, and the presence of silicate sheets blocking the chain propagation during polymerization. The result from DMA experiments is in agreement with the previous observations from the DSC and TGA experiments, in which the thermal stability of nanocomposites with 10.0 wt% organophilic MMT starts to decrease. A similar trend was also observed for PS-TMDMMT nanocomposites, in which 24% and 164% increases in E' were observed for nanocomposites with 1.0 wt% and 7.5 wt%, but only a 25% increase in E' was observed for PS-MMT nanocomposite with 10 wt% TMDMMT.

Overall, the results from TGA, DSC, and DMA experiments in the present study are in agreement with those from other reported research [49, 52, and 53]. The PS-MMT nanocomposites exhibited higher glass transition temperatures, higher decomposition temperatures, and higher storage modulus compared to the virgin polystyrene. The established suspension free radical polymerization method is an effective route in synthesizing polystyrene-MMT nanocomposites, from which an exfoliated nanocomposite structure was achieved.

The Effect of Surfactants on the Properties of PS-MMT Nanocomposites

Two other organophilic montmorillonites, TMCMMT and TMTMMT, were also employed to fabricate PS-MMT nanocomposites to understand the effect of different surfactants on the properties of the synthesized nanocomposites. PS-TMCMMT and PS-TMTMMT nanocomposites were prepared using 5.0 wt% TMCMMT and TMTMMT, and compared with PS-TMOMMT and PS-TMDMMT nanocomposites. Note that the alkyl chain length of the four alkyl quaternary ammonium salts used to fabricate organophilic

MMT decreases in the order of TMO > TMT > TMC > TMD. As in the PS-TMOMMT nanocomposite, no feature of the MMT peak was shown in XRD results for the other three PS nanocomposites, as illustrated in Figure 32, indicating the exfoliated structure of all four PS-MMT nanocomposites.

Table 11 summarized the comparison of properties of the four PS nanocomposites. Generally, PS-TMOMMT shows the highest decomposition temperature among the four nanocomposites, and the others have rather similar decomposition temperatures, as examined by TGA. Not surprisingly, PS-TMOMMT has the highest glass transition temperature, and with a decrease of alkyl chain length of surfactants, the T_g of the corresponding PS nanocomposites decreases. This indicates that PS-TMOMMT has the best compatibility with polystyrene. The above trend is also confirmed by Tan Delta results from DMA experiments, as shown in Figure 38, again from which the PS-TMOMMT nanocomposite gives the highest T_g among the four PS-nanocomposites.

Interestingly enough, by examining storage modulus curves in Figure 38, it was found that the four PS nanocomposites can be classified into two groups. The first group is PS-TMOMMT and PS-TMTMMT with E' values around 700 MPa at 25°C. The other group is PS-TMDMMT and PS-TMCMMT with E' values around 890 MPa at 25°C. PS nanocomposites containing organophilic MMT fabricated with shorter alkyl chain length surfactants (TMD and TMC) show the higher storage modulus values than those fabricated with relatively longer alkyl chain length surfactants (TMO and TMT). To understand whether it is the molecular weight difference that leads to the different storage modulus results, the obtained PS-MMT nanocomposites were extracted with tetrahydrofuran (THF) for 24 hours in a Soxhlet extraction apparatus. The molecular weights and polydispersed particles of the extracted polymers were measured by GPC and the results listed in Table 12. All the M_w values exhibited by the extracted polymer are in the order of 10^4 g/mol and are comparable with each other. Similar M_w , M_n and M_w/M_n ratios for all four samples indicate consistent suspension polymerization experiments in this study. Hence, the difference in storage modulus between PS-TMOMMT, PS-TMTMMT and PS-TMDMMT, PS-TMCMMT did not result from the difference in the molecular weights of the nanocomposites.

Another possibility which could affect the storage modulus value for the composite samples, is the uniformity of the distribution of nanofillers in the polymer matrix. Theoretically, at a given temperature, higher storage modulus results from the better nanofiller dispersion. DMA results, therefore, would indicate that TMDMMT and TMCMMT have a better dispersion than TMOMMT and TMTMMT during the suspension polymerization process. However, further examination of the results indicates the above conclusion is not correct. A simple and old, but effective and reliable, experiment was conducted, where a known amount of organoclay was placed on the bottom of each of a series of cylinders, then styrene monomer added at a 10:1 weight ratio to the clay, thoroughly mixed and allowed to set overnight. This experiment showed that TMOMMT and TMTMMT have much better swelling properties compared to TMDMMT and TMCMMT. It is well known that the presence of organoclay in nanocomposites will greatly improve the stiffness of materials leading to a higher storage modulus. On the other hand, it is possible that these organoclays may also serve as the plasticizer in nanocomposites, resulting in a decrease in storage modulus. Note that polystyrene is much more compatible with TMOMMT and TMTMMT and the better compatible plasticizer will improve the flexibility

of the materials. If so, the storage modulus obtained from DMA experiments is a compromised value resulting from both raising storage modulus by the role of nanoclay as the nanofiller and decreasing storage modulus by the role of nanoclay as the plasticizer. Recall the DMA results for both PS-TMOMMT and PS-TMDMMT nanocomposites with varied organoclay contents presented in the first section, where the storage modulus of nanocomposites with 10 wt% organoclay was smaller than the nanocomposites with 7.5 wt% organoclay. Considering the plasticizing effect based on the above assumption, the decrease in storage modulus could be attributed to the plasticizing effect as the dominant factor over the nanofiller effect for organoclay in the PS nanocomposite with 10.0 wt% organoclay.

Comparison of the Thermal Stability of PS-N-MMT and PS-P-MMT Nanocomposites

The concept to utilize phosphonium salts in PLSN as organic modifiers to layered silicates, instead of ammonium salts, is to take advantage of their unique property as stabilizers in many applications. Many phosphonium salts are of interest as flame retardants for a variety of thermoplastic polymers [54]. For example, phosphonium salts are used as flame retardants for textiles and heat stabilizers for nylon. Thus, the use of phosphonium salts as organic modifiers to layered silicates may further enhance the thermal and flammability properties of polymer nanocomposites.

The results of TGA experiments conducted in a nitrogen atmosphere of virgin PS, PS-N-C18 (PS nanocomposite synthesized using N-C18) nanocomposites, and PS-P-C18 (PS nanocomposite synthesized using P-C18) nanocomposites are presented in Figure 39. Clearly, the thermal stability of the nanocomposite is enhanced with respect to that of the virgin polystyrene, irrespective of the type of organo-MMT employed. Generally, the maximum decomposition temperature (T_d) of PS nanocomposites is about 20-25°C higher than that of virgin polymer. The type of organic modifier, either ammonium or phosphonium, makes no significant difference in the T_d , although the T_d of PS-P-C-18 is slightly higher than that of PS-N-C18. However, close examination of the TGA curve for the phosphonium nanocomposite (PS-P-C18) reveals a second step in the degradation, which is absent in both PS and PS-N-C18. Furthermore, the complete burn-out temperature for PS-P-C18 is clearly higher than that for PS-N-C18, due to the presence of the slow second decomposition step for PS-P-C18. This phenomenon can be attributed to the different char-forming behavior between ammonium based PS nanocomposites and phosphonium based PS nanocomposites.

The “two-stage theory of polymer combustion” suggests that the polymer must be volatized before combustion can occur. Therefore, two modes of actions for a flame retardant can be visualized. (1) A flame retardant may act in the gas phase by inhibiting exothermic oxidation reactions in the flame, thus reducing the energy feedback to the polymer surface which, in turn, renders the materials less flammable. Traditionally, halogen-containing compounds are widely employed as flame-retardant compounds involved in the inhibition of gas-phase chain reactions which occur in the combustion zone of the polymer flame. (2) A flame retardant may also act in the solid phase by formation of a barrier to energy and mass transport. This barrier prevents heat transfer back to the pyrolyzing polymer and inhibits the generation of volatiles. Char can be considered as a flame retardant

of this type. The role of OLS as a heat stabilizer and flame retardant falls into the second category by forming a char layer (carbonaceous residue) during polymer decomposition.

The observation of char layer formation for the nanocomposite samples was previously reported by Gilman [55]. He found that the nanocomposite structure present in the resulting char appears to enhance the performance of the char through reinforcement of the char layer, just as the nanostructure enhances the properties of the polymer. This multi-layered silicate structure acts as an excellent insulator and mass transport barrier, slowing the escape of the volatile products generated as the nylon-6 in the nanocomposite decomposes.

In the case of the ammonium-based PS nanocomposite, the clay char formation occurs at a temperature lower than that of polymer degradation, due to the relatively low thermal stability. Therefore, the formed char layer can be destroyed by the time the polymer degrades, resulting in less effectiveness in preventing heat and mass transfer. On the other hand, the higher decomposition temperature of the phosphonium-modified MMT renders the formation of char at a much higher temperature than does the relatively low decomposition temperature of the ammonium-modified MMT. This will allow the formed char to have more opportune time to retain the polymer before completely breaking up. Evidently, in the sense of flame proofing, P-MMT is a better choice than N-MMT for making PLSN with greater thermal stability and fire retardancy.

3.5. Conclusions

Thermal Stability and Degradation Mechanisms of OLS

The thermal stability of organically modified layered silicates (OLS) play a key role in the synthesis and processing of polymer-layered silicate (PLS) nanocomposites. The non-oxidative thermal degradation of montmorillonite, alkyl quaternary ammonium modified montmorillonite, and alkyl and aryl quaternary phosphonium modified montmorillonite were examined in detail for the first time using TG/FTIR/MS and Pyrolysis/GC-MS. Analysis of the products by GC-MS indicates that the initial degradation of the ammonium surfactant, whether in the N-MMT or the parent ammonium salt, follows a Hoffmann elimination process and that the architecture (trimethyl or dimethyl), chain length, surfactant mixture, exchange ratio, and preconditioning (washing), do not alter the initial onset temperatures. Catalytic sites on the aluminosilicate layer reduce the thermal stability of a fraction of the surfactants and lead to an average decrease of 15-25°C in the onset temperature, relative to the parent alkyl quaternary ammonium salt. On the other hand, the initial degradation of the alkyl P-MMTs follows potentially two reaction pathways – β -elimination [E_β] and nucleophilic displacement at phosphorus [$S_N(P)$] – reflecting the multiple environments of the surfactant in the silicate. Aryl P-MMT decomposition proceeds via either reductive elimination through a five-coordinate intermediate or radical generation through homologous cleavage of the P-phenyl bond. In conjunction, the thermal stability of the P-MMT depends to a greater degree on the architecture of the phosphonium surfactant than that of N-MMTs. Additionally, the interlayer environment of the montmorillonite has a more profound effect on the stability of the phosphonium surfactant than previously reported for ammonium-modified montmorillonite (N-MMT). Nonetheless, the overall thermal stability of P-MMT is higher than that of N-MMT. Finally, the release of organic compounds from the OLS is

staged and is associated with retardation of the product transfer arising from the morphology of the OLS.

Overall, four distinct interlayer environments are present between room temperature and the temperature at which the interlayer collapses. From room temperature to 70°C, the interlayer contains solid-like, paraffinic surfactants (i) (Vaia, et al. 1994). Subsequently, melting of the long chain alkyls results in a dynamic, liquid-like interlayer (ii). Depending on the chain length, architecture, and surfactant density, the first environment may not occur. At temperatures around 200°C, decomposition of the surfactant begins in the vicinity of the P (or N), resulting in an interlayer containing small volatiles and long chain molecules that are not associated with the aluminosilicate layer (iii). Finally, complete evolution of decomposition products at temperatures in excess of 350-380°C leads to gallery collapse and the retention of a substantial fraction of organic mass as carbonaceous char (iv).

Synthesis and Characterization of PS-MMT Nanocomposites

The first synthesis of well-dispersed (exfoliated) PS-MMT via *in situ* suspension free radical polymerization has been described. From XRD and TEM results, PS-MMT nanocomposites appear to have a well-dispersed (exfoliated) structure. The results showed that the PS-MMT nanocomposites have improved thermal stability and enhanced mechanical properties over virgin PS as evidenced by TGA, DSC, TMA, and DMA results. It was found that the alkyl chain length of the surfactant used in fabricating organo-MMT influences the mechanical properties of the synthesized PS-MMT nanocomposites. The longer the alkyl chain length of the surfactant, the higher the glass transition temperature of the synthesized PS nanocomposite. The results indicate that the organoclay in the nanocomposites seems to play dual roles: (a) as nanofiller, leading to the increase of storage modulus, and (b) as plasticizer, leading to the decrease of storage modulus. This results in lower storage moduli for PS-TMOMMT and PS-TMTMMT nanocomposites than for PS-TMDMMT and PS-TMCMMT nanocomposites. In addition, it was found that P-MMT based PS nanocomposites show better thermal stability and fire-retardant properties than N-MMT-based PS nanocomposites. This is attributed to the higher decomposition temperature of P-MMTs as compared to that of N-MMTs.

3.6. References

1. Xie, W., Pan W.-P. *Journal of Thermal Analysis and Calorimetry* **2001**, *65*, 669-685.
2. Brindley, G. W.; Brown, G. "Crystal Structure of Clay Minerals and Their X-ray identification", Mineralogical Society; London, 1980.
3. Greene-Kelly, R. In "The Differential Thermal Investigation of Clays", Mackenzie, R. C., Ed.; Mineralogical Society, London, 1957.
4. Grim, R. E. "Clay Mineralogy", McGraw-Hill, New York, 1968.
5. Kingery, W. D.; Bowen, H. K.; Uhlmann, D. R. "Introduction to Ceramics", Wiley and Sons, New York, 1976.
6. Burnside, S. D.; Giannelis, E. P. *Chem. Mater.* **1995**, *7*, 1597-1600.
7. Koster van Groos, A. F.; Guggenheim, S. *Am. Miner.* **1984**, *69*, 872-879.
8. Greene-Kelly, R. *Miner. Mag.* **1955**, *30*, 604-615.
9. Grim, R. E.; Bradley, W. F. *Amer. Min.* **1948**, *33*, 50-59.

10. Stucki, J. W.; Bish, D. L.; Duffy, C. J. "CMS workshop lecture, thermal analysis in clay science", Vol. 3, The Clay Minerals Society, 1990.
11. Chou, C. C.; McAtee, J. L., Jr. *Clays Clay Miner.* **1969**, *17*, 339-346.
12. Vaia, R. A.; Teukolsky, R. K.; Giannelis, E. P. *Chem. Mater.* **1994**, *6*, 1017-1022.
13. Lagaly, G.; Beneke, K.; Weiss, A. *Am. Miner.* **1975**, *60*, 642-649.
14. Beneke, K.; Lagaly, G. *Am. Miner.* **1983**, *68*, 818.
15. Beneke, K.; Lagaly, G. *Am. Miner.* **1977**, *62*, 763.
16. Wang L.Q.; Liu, J.; Exarhos, G.J.; Flanigan, K.Y.; Bordia, R. *J. Phys. Chem. B* **2000**, *104*, 2810-2816.
17. Hackett, E.; Manias, E.; Giannelis, E. P. *Chem. Mater.* **2000**, *12*, 2161.
18. Gilman, J. W., *Appl. Clay Sci.* **1999**, *15*, 31-49.
19. Cope, A. C.; Trumbull, E. R. In "Organic Reactions 11", John Wiley and Sons, New York, 1960.
20. March, J. "Advanced Organic Chemistry, Reactions, Mechanisms and Structures", 4ed; John Wiley and Sons, New York, 1992.
21. Nyden, M. R.; Gilman, J. W. *Comput. Theor. Poly. Sci.* **1997**, *7*, 191.
22. Ward, J. W. *Fuel Processing Technol.* **1993**, *35*, 55-85.
23. Hagg, W.O. In "Zeolites and Related Microporous Materials: State of the Art 1994", Vol 84(PA-C), 1375-1394, Weitkamp, J., Ed.; Elsevier, Amsterdam, 1994.
24. Kosolapoff, G. M.; Maier, L. "Organic Phosphorus Compounds", Vol 2, John Wiley & Sons, Inc., New York, 1972.
25. Xie, W.; Pan, W.-P.; Hunter, D.; Vaia, R. *Chem. Mater.* **2001** *13*, 2979.
26. Farmer, V. C.; Russell, J. D. *Spectrochim. Acta* **1964**, *20*, 1149-1173.
27. Miller, G. J. *J. Phys. Chem.* **1961**, *65*, 800.
28. Dukan, J. F.; and Foster, P. K. *J. Am. Ceram. Soc.* **1974**, *57*, 57.
29. Snyder, R. G.; Strauss, H. L.; Elliger, C. A. *J. Phys. Chem.* **1982**, *86*, 5145-5150.
30. Kawai, T.; Umemura, J.; Takenaka, T.; Kodama, M.; Seki, S. *J. Colloid Interface Sci.* **1995**, *103*, 56.
31. Wang, W.; Li, L.; Xi, A. *J. Colloid Interface Sci.* **1993**, *155*, 369-373.
32. Weers, J. G.; Scheuing, D. R. In "Fourier Transform Infrared Spectroscopy in Colloid and Interface Science"; Scheuing, D. R., Ed.; ACS Symposium Ser. 447; American Chemical Society: Washington, DC, 1990, 87-122.
33. Hudson, R. F. "Structure and Mechanism in Organo-Phosphorus Chemistry", Academic Press, New York, 1965.
34. Goldwhite, H. "Introduction to phosphorus chemistry", Cambridge University Press, Cambridge, 1981.
35. Fenton, G. W.; Ingold, C. K. *J. Chem. Soc.* **1929**, 2342.
36. Hey, L.; Ingold, C. K. *J. Chem. Soc.* **1933**, 531.
37. Wittig, G.; Geissler, G. *Ann. Chem. Liebigs* **1953**, *580*, 44.
38. Schollkopf, U. *Angew. Chem.* **1959**, *71*, 260.
39. Claereboudt, J.; Claeys, M; Geise, H.; Gijbels, R.; Vertes, A. *J. Am. Soc. Mass. Spec.* **1993**, *4*, 798.
40. Cristau, H. J.; Plenat, F. In "The Chemistry of Organophosphorus Compounds", Vol. 3, John Wiley and Sons, New York, 1994.
41. Bleam, W. F.; Hoffmann, R. "Inorg. Chem." **1988**, *27*, 3180-3186.

42. Bleam, W. F.; Hoffmann, R. *Phys. Chem. Minerals* **1988**, *15*, 398-408.
43. Corbridge, D. E. C. "Phosphorus: An Outline of its Chemistry, Biochemistry and Technology", Elsevier Science Publishers, Amsterdam, The Netherlands, 1990.
44. Grayson, M.; Keough, P. T. *J. Am. Chem. Soc.* **1960**, *82*, 3919.
45. Abraham, S. J.; Criddle, W. J. *J. Anal. Appl. Pyrol.* **1985**, *7*, 337.
46. Vaia, R. A.; Price, G.; Ruth, P. N.; Nguyen, H. T.; Lichtenhan, A. *Appl. Clay Sci.* **1999**, *15 (1)*, 67-92.
47. Fong, H.; Vaia, R.A; Sanders, J.H.; Lincoln, D.; Vreugdenhil A.J.; Liu, W; Bultman, J.; Chen, C. *Chem. Mater.* **2001**, *13*, 4123-4129.
48. Zanetti, M.; Camino, G. In "The Proceedings of Tenth International Conference – Additives 2001", Hilton Head Island, South Carolina, 2001, 1-9.
49. Fu, X.; Qutubuddin, S. *Polymer* **2001**, *42*, 807-813.
50. Gilman, J. W.; Jackson, C. L.; Morgan, A. B.; Harris, R., Jr.; Manias, E.; Giannelis, E. P.; Wuthenow, M.; Hilton, D.; Philips, S. H. *Chem. Mater.* **2000**, *12*, 1866-1873.
51. Zhu, J.; Morgan, A. B.; Lamelas, F. J.; Wilkie, C. A. *Chem. Mater.* **2001**, *13*, 3774-3780.
52. Chen, G.; Liu, S.; Chen, S.; Qi, Z. *Macromol. Chem. Phys.* **2001**, *202*, 1189-1193.
53. Hasegawa, N.; Okamoto, H.; Kawasumi, M.; Usuhi, A. *J. Appl. Poly. Sci.* **1999**, *74*, 3359-3364.
54. Granzow, A. "Flame retardation by phosphorus compounds", *Acc. Chem. Res.* **1978**, *11*, 177-183.
55. Gilman, J.W.; Kashivagi, T.; Nyden, M.; Brown, J.E.T.; Jackson, C.L.; Lomakin, S.; Giannelis, E.P.; Manias, E. "Chemistry and Technology of Polymer Additives", Chapter 14, Almalaika, S.; Golovoy, A.; Wilkie, C.A., Eds., Blackwell Science Ltd., Oxford, 1999.

4. Personnel Supported

Faculty:

WEI-PING PAN, Department of Chemistry, Western Kentucky University, Bowling Green, KY 42101.
 Tel: (270) 780-2532, Fax: (270)780-2569, Email: wei-ping.pan@wku.edu

JOHN T. RILEY, Department of Chemistry, Western Kentucky University, Bowling Green, KY 42101.
 Tel: (270) 780-2568, Fax: (270)780-2569, Email: john.riley@wku.edu

CHARLES W.M. LEE, Department of Chemistry, Western Kentucky University, Bowling Green, KY 42101.
 Tel: (270) 745-3943, Fax: (270) 745-5361, Email: charles.lee@wku.edu

Graduate Students:

WEI XIE, Department of Chemistry, Western Kentucky University and Department of Chemistry, University of Louisville, Louisville, KY; Ph.D. Dissertation, "Thermal Degradation Chemistry of Organically Modified Layered Silicates and Properties of Polystyrene-Montmorillonite Nanocomposites", December, 2002.

LAURA WELLS, Department of Chemistry, Western Kentucky University, Bowling Green, KY 42101

QUENTIN J. LINEBERRY, Department of Chemistry, Western Kentucky University, Bowling Green, KY 42101

5. Publications

- (1) Xie, W., Hwu, J., Jiang, G., Buthelezi, T., Pan, W.-P. "A Study of The Effect of Surfactants on The Properties of Polystyrene-Montmorillonite Nanocomposites", *Polymer Engineering & Science* **2003**, *43*(1), 214-222.
- (2) Xie, W., Xie, R., Pan, W.-P., Hunter, D., Koene, B., Tan, L.-S., Vaia, R. "Thermal Stability of Quaternary Phosphonium Modified Montmorillonites", *Chemistry of Materials* **2002**, *14*(11), 4837-4845.
- (3) Xie, W., Gao, Z., Pan, W.-P., Hunter, D., Singh, A., Vaia, R. "Thermal Degradation Chemistry of Alkyl Quaternary Ammonium Montmorillonite", *Chemistry of Materials* **2001**, *13*, 2979-2990.

6. Interactions/Transitions

6.a. *Participation/presentations at meetings, conferences, seminars, etc.*

- (1) Pan, W.-P. "A Study of the Effect of Surfactants on The Properties of Polystyrene-Montmorillonite Nanocomposites" in the Proceedings of Ninth Annual International Conference on Composites Engineering, San Diego, CA, 2002.
- (2) Lineberry, Q., Xie, W., Pan, W.-P. "Synthesis and Characterization of Polystyrene-Montmorillonite Nanocomposites by Suspension Polymerization", Proceedings of the 30th Conference on North American Thermal Analysis Society, St. Louis, Missouri, Sep 24-26, 2001, P257-263.
- (3) Xie, W., Pan, W.-P., Vaia, R. "A Study of Thermal Degradation Mechanism of Organically Modified Montmorillonite", Proceedings of the 30th Conference on North American Thermal Analysis Society, St. Louis, Missouri, Sep 24-26, 2001, P264-269.
- (4) Pan, W.-P., "Thermal Degradation Chemistry of Alkyl Quaternary Ammonium Montmorillonite" in the Proceedings of EPSCoR Conference, Bowling Green, Kentucky, 2001.
- (5) Gao, Z., Zou, D., Xie, W., Pan, W.-P. "The Study of Decomposition Mechanism of Organic Modified Clay by ThermexTM Inlet and GC/TOFMS Technique," Proceedings of the 28th Conference on North American Thermal Analysis Society, Orlando, FL, USA, Oct 4-6, 2000, P517-522.
- (6) Gao, Z., Xie, W., Pan, W.-P. "The preparation and Characterization of Clay Filled PMMA Nanocomposite" in the Proceedings of 12th International Congress on Thermal Analysis and Calorimetry, Copenhagen, Denmark, 2000.

- (7) Xie, W., Gao, Z., Pan, W.-P., Vaia, R., Hunter, D., and Singh, A. "Characterization of Organically Modified Montmorillonite by Thermal Techniques," The Proceedings of the American Chemical Society, Division of Polymeric Materials: Science and Engineering, San Francisco, USA, March 26-30, 2000, P284-289
- (8) Pan, W.-P. "A Study of Organic Modified Montmorillonite by Thermal Techniques" in the Proceedings of EPSCoR Conference, Lexington, Kentucky, 2000.

6.b. Consultative and advisory functions to other laboratories and agencies.

Daily email with Dr. Richard Vaia at WPAFB and Mr. Doug Hunter at Southern Clay Products, Inc. for discussion of the project work, including technical and scientific issues.

Wei-Ping Pan, Wei Xie and Laura Wells visited Captain Dr. Richard Vaia at Wright-Patterson on June 17, 2000.

Wei-Ping Pan, Wei Xie and Quentin Lineberry visited Dr. Sandi Campbell, Polymer Branch, Materials Division, NASA Glenn Research Center, on August 8, 2001. Dr. Wei-Ping Pan gave a seminar about the degradation chemistry of organically modified montmorillonites.

7. New discoveries, inventions, or patent disclosures

N/A

8. Honors/Awards

Pan, W.-P., Awarded the title of Fellow of the North American Thermal Analysis Society, 1997.

9. Appendix

- 9.1. List of Tables
- 9.2. List of Figures
- 9.3. List of Schemes

Table 1. Alkyl Quaternary Ammonium Modified Montmorillonites.

N:MMTs	Surfactant ^a	Surfactant Molecular Weight (g/mole)	Milli-equivalent Exchange Ratio, MER (meq/100g)	Fraction Organic Content	d ₀₀₁ (nm)
N-Coco	TMC	238.6	95	0.185	1.44
N-Tallow	TMT	301.7	95	0.223	1.80
N-C12	TMD	228.5	95	0.178	1.50
N-C18	TMO	312.7	95	0.229	1.82
N-2CoCo	DMDC	403.0	95	0.277	1.86
N-2HTallow-A	DMDHT	529.3	140	0.426	3.48
N-2HTallow-B	DMDHT	529.3	120	0.388	3.25
N-2HTallow-C	DMDHT	529.3	95	0.335	2.60
N-2C18	DMDO	550.7	95	0.340	2.66

^aTMC: trimethylcoco ammonium chloride; TMT: trimethyltallow ammonium chloride; TMD: trimethyldodecyl ammonium chloride; TMO: trimethyloctadecyl ammonium chloride; DMDC: dimethylidicoco ammonium chloride;

DMDHT: dimethylidihydrogenatedtallow ammonium chloride; DMDO: dimethyldioctadecyl ammonium chloride.

Table 2. Composition of Natural Product Alkyls.

	CoCo		Tallow		Hydrogenated Tallow	
	n^a	$\bar{n}^b = 12.72$		$\bar{n}^b = 17.22$		$\bar{n}^b = 17.22$
saturated	8	6				
	10	7				
	12	51				
	14	19	3			
	15		0.5			
	16	9	29			
	17		1			
	18	2	20			
	14'		0.5			
	16'	6	2			
unsaturated	18'		44			
				3		
					3	

^an: number of carbon atoms per alkyl chain.

^b \bar{n} : mean number of carbons per chain.

Table 3. Decomposition Temperatures in UHP N₂.

	TGA, °C			MS, °C		
	T _{onset, 1}	T _{max, 1}	T _{onset, 2}	T _{max, 2}	T _{onset, 1}	T _{onset, 2}
Trimethyl alkyl						
N-CoCo	151 (120 ^c)	226	263 (258 ^c)	383	167	252
N-CoCo-A ^a	163	232	249	378		
N-CoCo-B ^a	177	235	246	382		
N-CoCo-C ^a	178	* ^d	* ^d	383		
N-Tallow	150 (139 ^c)	226	262 (263 ^c)	375	177	268
N-C12	151 (128 ^c)	224	258 (259 ^c)	384	178	258
N-C18	143 (135 ^c)	223	259 (260 ^c)	368	164	244
TMC	177	241				
TMT	179	238				
TMD	181	245				
TMO	187	242				
Dimethyl dialkyl						
N-2CoCo	137	238	262	291, 366 ^c		
N-2HTallow-A	157	242	260	300, 388 ^c		
N-2HTallow-B	155	247	255	301, 370 ^c		
N-2HTallow-B1 ^b	160	* ^d	* ^d	293, 349 ^c		
N-2HTallow-C	154	231	243	277, 344 ^c		
N-2HTallow-C1 ^b	161	* ^d	* ^d	293, 348 ^c		
N-2C18	161	230	244	287, 346 ^c		

^a Soxlet extract with ethanol for a) 3 hrs, b) 6 hrs and c) 9 hrs.

^b Washed three times with methanol.

^c Onset temperature determined before pre-drying OLS at 140°C.

^d Magnitude of initial event too small to allow estimation of temperature.

^e Second and third decomposition peaks.

Table 4. Relative Mass Loss (TGA) During Decomposition of the N-MMTs.

Trimethyl alkyl	% Mass loss		% Total Organic	Fraction Organic Evolved in 1 st Event
	<120°C	120-450°C		
N-CoCo	0.90	17.6	4.9	19.00
N-CoCo-A ^a	0.63	13.0	1.6	15.60
N-CoCo-B ^a	0.50	14.1	1.0	15.08
N-CoCo-C ^a	0.61	14.2	0.7	15.09
N-Tallow	0.78	23.0	8.0	23.93
N-C12	1.19	17.8	4.8	19.16
N-C18	1.64	23.7	9.0	23.88
Dimethyl dialkyl				
N-2CoCo	0.33	24.7	7.4	26.00
N-2HTallow-A	0.60	40.0	7.7	41.52
N-2HTallow-B	0.57	38.8	4.0	38.85
N-2HTallow-B1 ^b	0.48	32.1	0.3	32.06
N-2HTallow-C	0.72	31.9	2.6	32.77
N-2HTallow-C1 ^b	0.49	31.3	0.3	31.66

^a Soxhlet extracted with ethanol for a) 3 hrs, b) 6 hrs, c) 9 hrs.

^b Washing three times with methanol.

Table 5. Representative Organic Species Evolved from N-C18 and TMO (Pyrolysis/GC-MS).

Sample ID	200°C	400°C
N-C18	<p>alkane, linear 1-chloro branched alkane</p> <p>Tridecane, 3-methyl-, C₁₄H₃₀</p> <p>C₁₃H₃₃N, C₁₇H₃₇N</p>	<p>C₁₆H₃₃Cl, C₁₈H₃₇Cl</p> <p>C₁₅H₃₃N, C₁₇H₃₇N</p> <p>C₁₈H₃₉N</p>
	<p>tertiary amine, N,N-dimethyl- primary amine, linear</p> <p>linear alkene, 1- linear alkene, n-</p>	<p>C₁₆H₃₂, C₁₇H₃₄</p> <p>C₉H₁₈, C₁₀H₂₀, C₁₄H₂₆, C₁₇H₃₄</p> <p>3-Nonene, (E)- [C₉H₁₈], 2-Decene, (Z)- [C₁₀H₂₀], 3-Undecene, (E)- [C₁₁H₂₂], 5- Dodecene, (Z)- [C₁₂H₂₄], 3-Tridecene, (Z)- [C₁₃H₂₆], 6-Tridecene [C₁₃H₂₆], 3-Octadecene, (E)- [C₁₈H₃₆], 3-Octadecene, (E)- [C₁₈H₃₆]</p> <p>1-Octene, 3-methyl- [C₉H₁₈], 3-Heptene, 2,6- dimethyl- [C₉H₁₈], 4-Nonene, 2-methyl [C₁₀H₂₀], 1-Octene, 3,7-dimethyl-, [C₁₀H₂₀], 4- Undecene, 10-methyl, (E)- [C₁₂H₂₄]</p>
	<p>linear aldehyde</p> <p>branched aldehyde</p>	<p>C₁₄H₂₈O, C₁₅H₃₀O, C₁₆H₃₂O</p> <p>E-15-Hepdecenal [C₁₇H₃₂O]</p>
TMO	<p>alkane, linear 1-chloro</p> <p>tertiary amine, N,N-dimethyl- linear alkene, 1-</p>	<p>C₁₃H₂₇Cl, C₁₆H₃₃Cl, C₁₈H₃₇Cl</p> <p>C₉H₂₁N, C₁₀H₂₃N, C₁₅H₃₃N, C₁₇H₃₇N</p> <p>C₁₀H₂₀, C₁₂H₂₄</p>

Table 6. Properties and Relative Mass Losses (TGA) During Decomposition of the P-MMTs.

Sample ID	Surfactants ^a	Milli-equivalent	d_{001}	% Mass loss ^b			% Total Organic
				Exchange Ratio, MER (nm)	<120°C	120-500°C	
				(meq/100g)			
P-C12	TPhDPBr	95	1.82	0.55	21.72	11.38	27.14
P-C14	TBTBBr	95	1.93	0.49	25.35	8.04	25.50
P-C16	TBHPBr	95	2.04	0.53	26.24	9.84	26.49
P-C18	TBOPBr	95	2.18	0.41	36.98	21.82	37.13
P-4Ph	TPhPBr	95	1.88	1.89	15.29	7.97	25.66
P-4C8	TOPBr	95	2.20	0.45	22.11	7.98	24.71
N-4C8	TONBr	95	2.21	0.47	24.97	8.62	27.08

^aTPhDPBr: triphenyldodecyl phosphonium bromide; TBTPBr: tributyltetradecyl phosphonium bromide; TBHPBr: tributylhexadecyl phosphonium bromide;

TBOPBr: tributyoctadecyl phosphonium bromide; TPhPBr: tetraphenyl phosphonium bromide;

TOPBr: tetraoctyl phosphonium bromide; TONBr: tetraoctyl ammonium bromide.

^b1st event refers to first organic decomposition peak corresponding to mass loss between $T_{onset,1}$ and $T_{onset,2}$ (see Table 2 for definition).

Table 7. Decomposition Temperatures in UHP N₂.

	TGA, °C			
	T _{onset, 1}	T _{max, 1}	T _{onset, 2} ^a	T _{max, 2} ^b
<u>P- MMT</u>				
P-C12	210 (215 ^c)	301	341	355
P-C14	192 (188 ^c)	367	383	415
P-C16	193 (191 ^c)	321	382	408
P-C18	196 (181 ^c)	369	407	429
P-4Ph	230 (230 ^c)	347	386	409
P-4C8	226 (227 ^c)	360	377	446
TBTPBr	252	363		
TBOPBr	262	363		
TPhPBr	309	407		
TOPBr	262	362		
<u>N- MMT</u>				
N-4C8	162 (157 ^a)	266	289	327
TONBr	170	212		

^a T_{onset, 2} refers to peak valley temperature between 1st peak and 2nd peak in the DTG curve.

^b T_{max, 2} refers to peak maximum temperature of 2nd DTG peak.

^c Onset temperature determined before pre-drying OLS at 140°C.

Table 8. Representative Organic Species Evolved from P-C18 and TBOPBr (Pyrolysis/GC-MS).

	250°C	300°C	350°C	400°C
P-C18				
alkane, linear	$C_{18}H_{38}$	C_8H_{18} , C_9H_{20} , $C_{13}H_{28}$, $C_{16}H_{34}$, $C_{17}H_{36}$	C_8H_{18} , C_9H_{20} , $C_{12}H_{26}$, $C_{13}H_{28}$, $C_{14}H_{30}$	$C_{10}H_{22}$, $C_{12}H_{26}$, $C_{13}H_{28}$, $C_{17}H_{36}$
alkane, branched	Decane, 2,5,9-trimethyl- [C ₁₃ H ₂₈]	Tridecane, 4-methyl- [C ₁₄ H ₃₀]	Tridecane, 4-methyl- [C ₁₄ H ₃₀]	Tridecane, 4-methyl- [C ₁₄ H ₃₀]
Phosphine	$C_{12}H_{27}P$	$C_{12}H_{27}P$	$C_{12}H_{27}P$	$C_{12}H_{27}P$
Phosphine oxide	$C_{12}H_{27}OP$	$C_{12}H_{27}OP$	$C_{12}H_{27}OP$	$C_{12}H_{27}OP$
linear alkene, 1-	$C_{12}H_{24}$, $C_{13}H_{26}$, $C_{14}H_{28}$, $C_{18}H_{36}$	$C_{12}H_{24}$, $C_{13}H_{26}$, $C_{14}H_{28}$, $C_{17}H_{34}$, $C_{18}H_{36}$	C_7H_{14} , C_8H_{16} , C_9H_{18} , $C_{10}H_{20}$, $C_{12}H_{24}$, $C_{13}H_{26}$, $C_{14}H_{28}$, $C_{15}H_{30}$, $C_{17}H_{34}$, $C_{18}H_{36}$	C_8H_{16} , C_9H_{18} , $C_{10}H_{20}$, $C_{11}H_{22}$, $C_{12}H_{24}$, $C_{13}H_{26}$, $C_{14}H_{28}$, $C_{15}H_{30}$, $C_{17}H_{34}$, $C_{18}H_{36}$
linear alkene, n-			4-Dodecene, (E)- [C ₁₂ H ₂₄] 7-Hexadecene, (Z)- [C ₁₆ H ₃₂]	4-Dodecene, (E)- [C ₁₂ H ₂₄] 7-Hexadecene, (Z)- [C ₁₆ H ₃₂]
linear aldehyde	$C_{16}H_{32}O$	$C_{16}H_{32}O$	$C_{16}H_{32}O$	$C_{16}H_{32}O$
TBOPBr				
alkane, 1-bromo	C_4H_9Br , $C_{18}H_{37}Br$	C_4H_9Br , $C_{15}H_{21}Br$, $C_{18}H_{37}Br$	C_4H_9Br , $C_{15}H_{31}Br$, $C_{18}H_{37}Br$	C_4H_9Br , $C_{15}H_{31}Br$, $C_{18}H_{37}Br$
linear alkene, 1-	$C_{17}H_{34}$, $C_{18}H_{36}$	C_8H_{16} , $C_{11}H_{22}$, $C_{15}H_{30}$, $C_{18}H_{36}$	C_8H_{16} , $C_{11}H_{22}$, $C_{15}H_{30}$, $C_{18}H_{36}$	C_8H_{16} , $C_{11}H_{22}$, $C_{15}H_{30}$, $C_{18}H_{36}$
Phosphine	$C_{12}H_{27}P$	$C_{12}H_{27}P$	$C_{12}H_{27}P$	$C_{12}H_{27}P$

Table 9. Representative Organic Species Evolved from P-4Ph and TPhPBr (Pyrolysis/GC-MS).

Aryl	250°C	300°C*	300°C*	P-4Ph		350°C	400°C
				250°C	300°C*		
				Biphenyl [C ₁₂ H ₁₀]	Biphenyl [C ₁₂ H ₁₀]; o-Terphenyl [C ₁₈ H ₁₄]; m-Terphenyl [C ₁₈ H ₁₄]	Biphenyl [C ₁₂ H ₁₀]; Acenaphthene [C ₁₂ H ₁₀]; o-Terphenyl [C ₁₈ H ₁₄]; m-Terphenyl [C ₁₈ H ₁₄]; p-Terphenyl [C ₁₈ H ₁₄]; Triphenylene [C ₁₈ H ₁₂]; Phosphine, triphenyl [C ₁₈ H ₁₅ P]	
Phosphine				Phosphine, triphenyl [C ₁₈ H ₁₅ P]	Phosphine, triphenyl [C ₁₈ H ₁₅ P]	Phosphine, triphenyl [C ₁₈ H ₁₅ P]	
Phosphine oxide				Triphenylphosphine oxide [C ₁₈ H ₁₅ OP]	Triphenylphosphine oxide [C ₁₈ H ₁₅ OP]	Triphenylphosphine oxide [C ₁₈ H ₁₅ OP]	
				TPhPBr	C ₆ H ₅ Br	C ₆ H ₅ Br	
					Biphenyl [C ₁₂ H ₁₀]	1,1'-Biphenyl, 2-bromo- [C ₁₂ H ₉ Br]	
Aryl					Biphenyl [C ₁₂ H ₁₀]	Biphenyl [C ₁₂ H ₁₀]; o-Terphenyl [C ₁₈ H ₁₄]; Triphenylene [C ₁₈ H ₁₂]; Phosphine, triphenyl [C ₁₈ H ₁₅ P]	
Phosphine					Phosphine, triphenyl [C ₁₈ H ₁₅ P]	Phosphine, triphenyl [C ₁₈ H ₁₅ P]	

* The reaction temperature for TPhPBr is 310°C.

Table 10. The Effect of Organophilic-Montmorillonite Content on the Properties of PS-Montmorillonite Nanocomposites^a.

ID	PS-TMO-MMT				PS-TMD-MMT			
	MMT (%)	Yield ^b (%)	Act. ^c ($\times 10^3$)	T _g (°C)	T _d ^a (°C)	Yield ^b (%)	Act. ^c ($\times 10^3$)	T _g (°C)
0	82.7	2.15	91.0	404.2	82.7	2.16	91.0	404.2
1.0	93.4	2.44	100.0	417.1	93.2	2.40	92.5	412.5
2.5	92.3	2.46	102.3	420.8	92.5	2.42	94.2	418.0
5.0	89.2	2.49	102.8	425.8	89.4	2.48	94.8	421.3
7.5	88.3	2.48	100.8	420.0	88.1	2.40	92.7	420.9
10.0	78.9	2.24	92.8	412.3	80.3	2.30	89.8	420.6

a : DI-water = 400 mL, PVA = 0.4 g, styrene = 0.2 mole, BPO = 1×10^{-3} mole, reaction temperature = 80°C, reaction time = 8 hrs.

b : Yield % = (weight of product)/(weight of styrene + weight of organoclay).

c : Activity = (weight of product)/(mole of BPO \times hrs).

d : T_d = maximum decomposition temperature in DTG curve.

Table 11. The Effect of Surfactants on the Properties of PS-Montmorillonite Nanocomposites^a.

Properties	PS-TMO-MMT	PS-TMT-MMT	PS-TMC-MMT	PS-TMD-MMT
T _d (°C)	425.8	423.1	422.0	421.3
T _g (°C)	102.8	95.7	94.9	94.8
Storage Modulus ^b	709.1	686.7	896.0	887.3
E' (MPa)				

^aOrganic-MMT content is 5.0 wt%

^bStorage Modulus (E'): measured at 25°C

Table 12. Average Molecular Weights and Polydispersed Particles of PS-MMT Nanocomposites.

Sample ID	Organic-MMT Content (wt %)	M _n x 10 ⁻³ (g/mol)	M _w x 10 ⁻³ (g/mol)	M _w /M _n
PS-TMO-MMT	5.0	34	88	2.58
PS-TMT-MMT	5.0	39	95	2.42
PS-TMC-MMT	5.0	43	100	2.50
PS-TMD-MMT	5.0	39	87	2.24

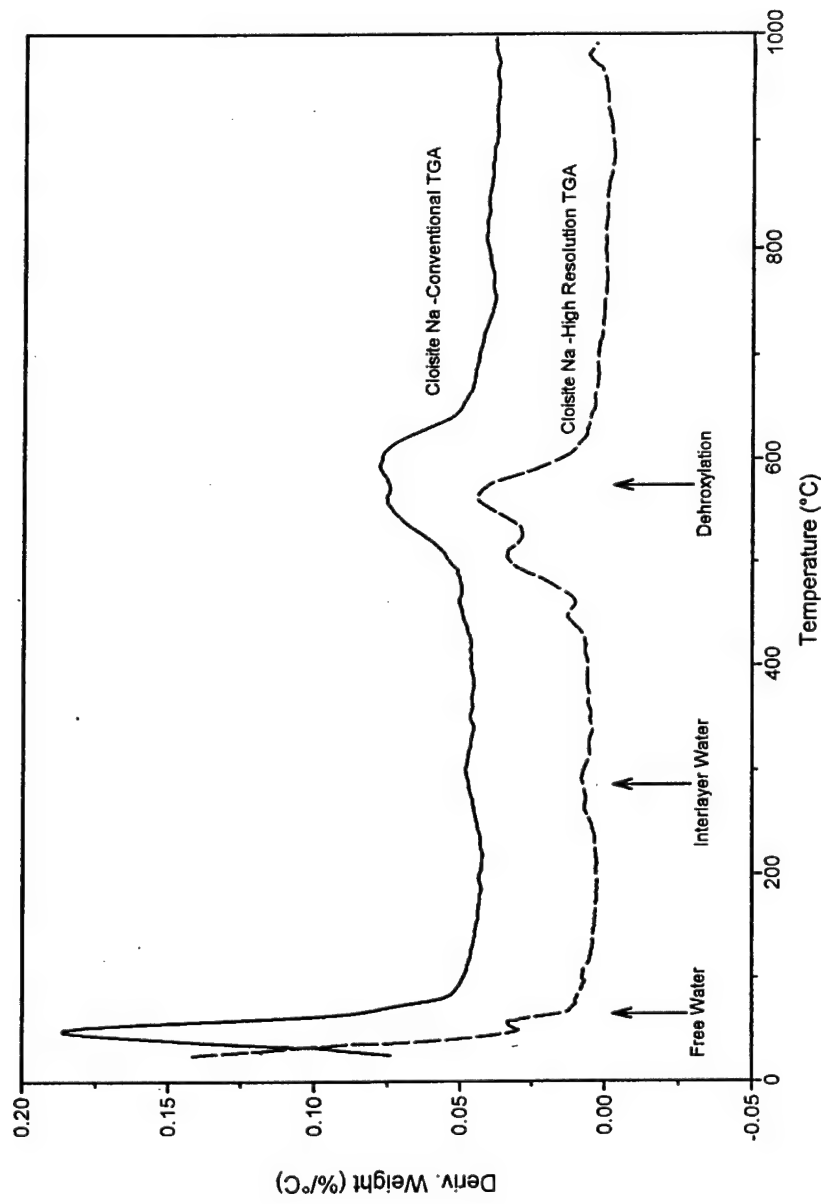


Figure 1. DTG curves from conventional and high resolution TGA studies of pristine montmorillonite.

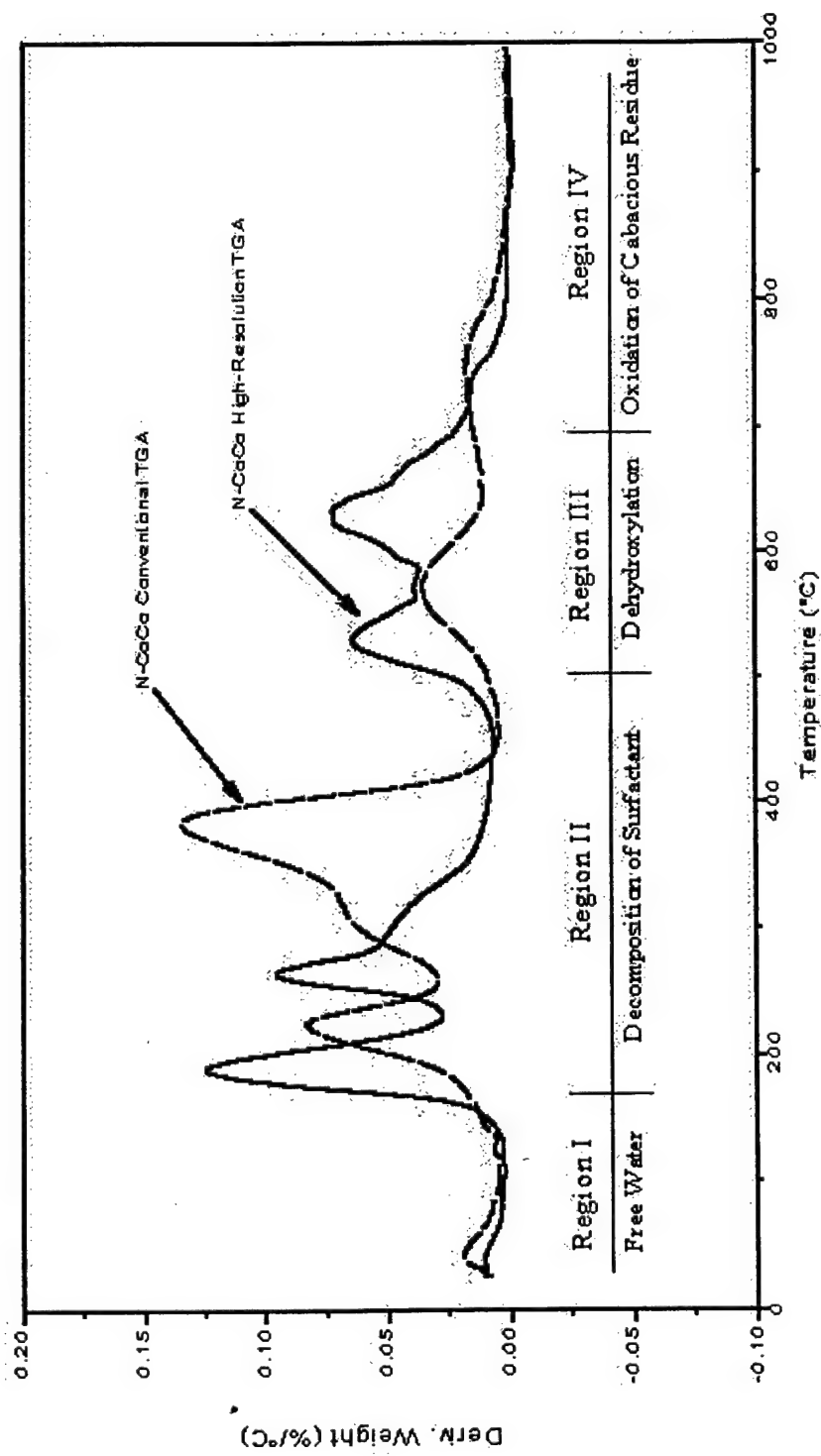


Figure 2. DTG curves from conventional and high resolution TGA studies of N-CoCo.

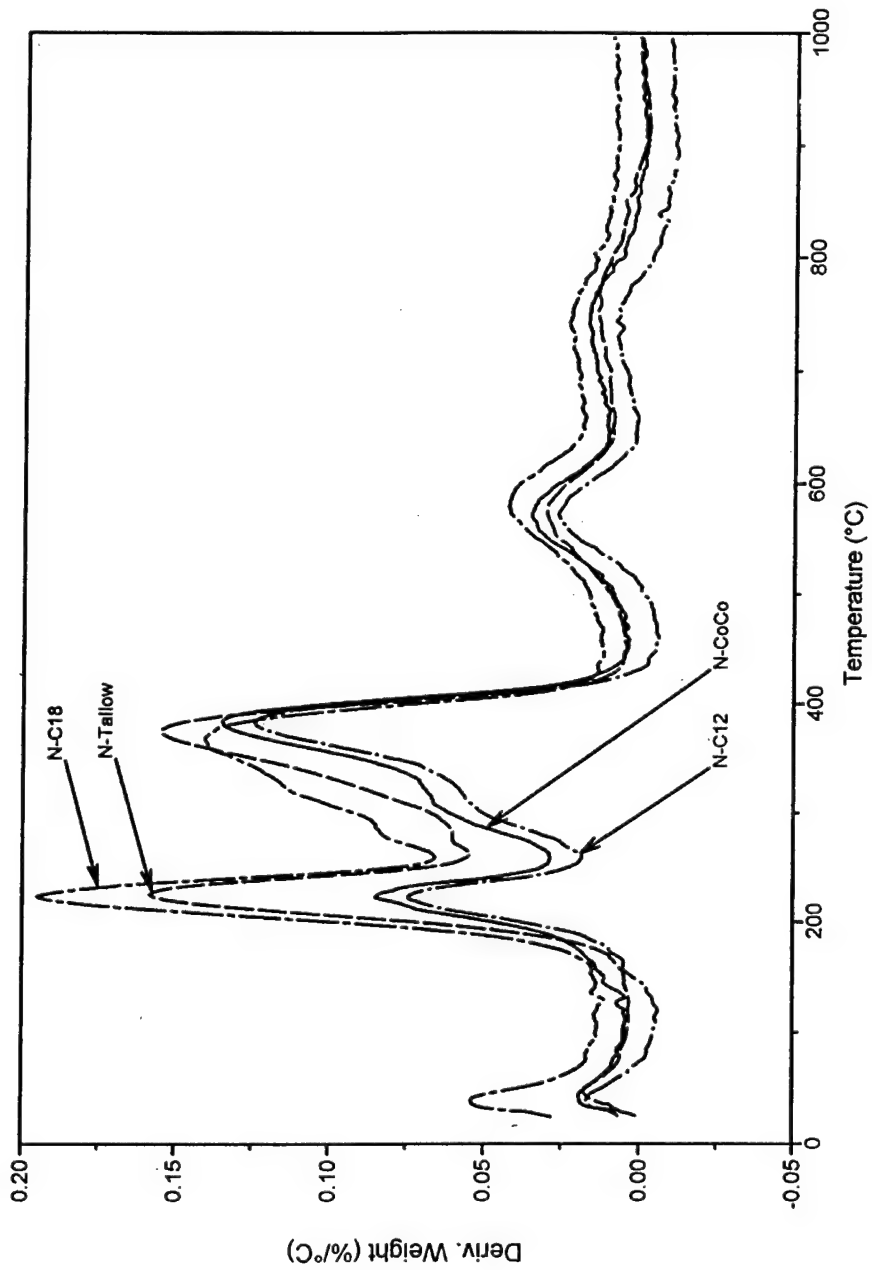


Figure 3. DTG curves from conventional TGA studies of N-C12, N-CoCo, N-Tallow and N-C18.

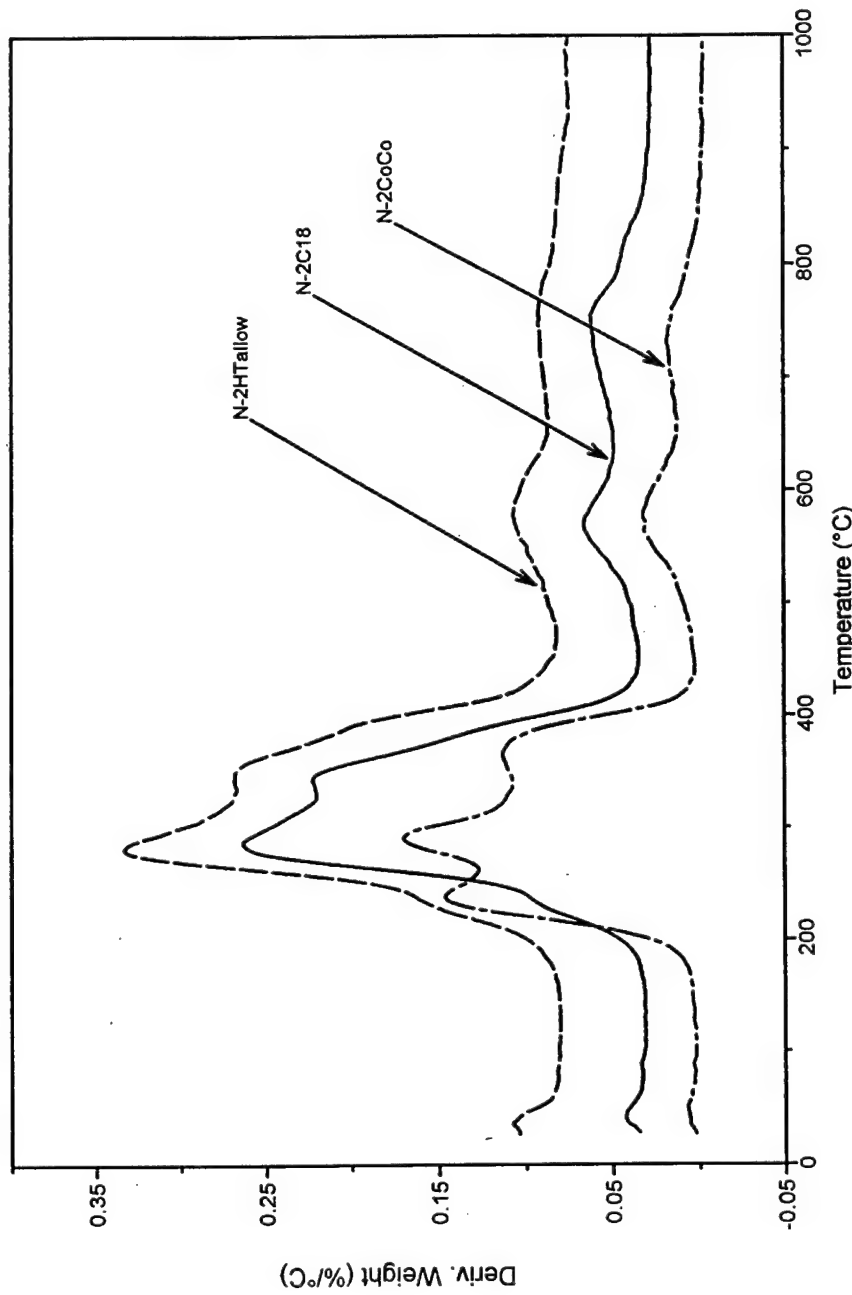


Figure 4. DTG curves from conventional TGA studies of N-2Htallow, N-2CoCo, and N-2C18.

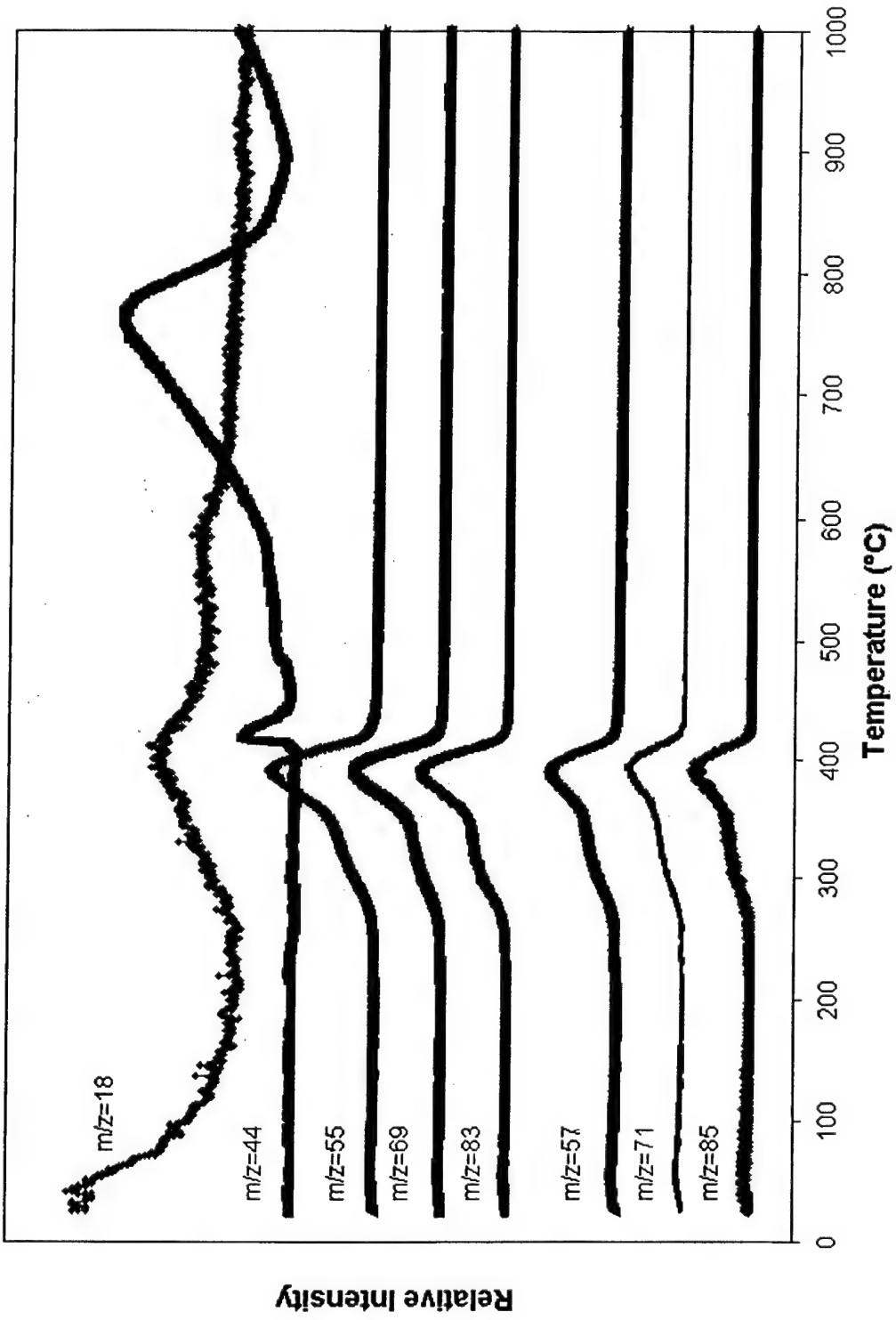


Figure 5. Temperature dependent MS results of the evolution products for N-CoCo.

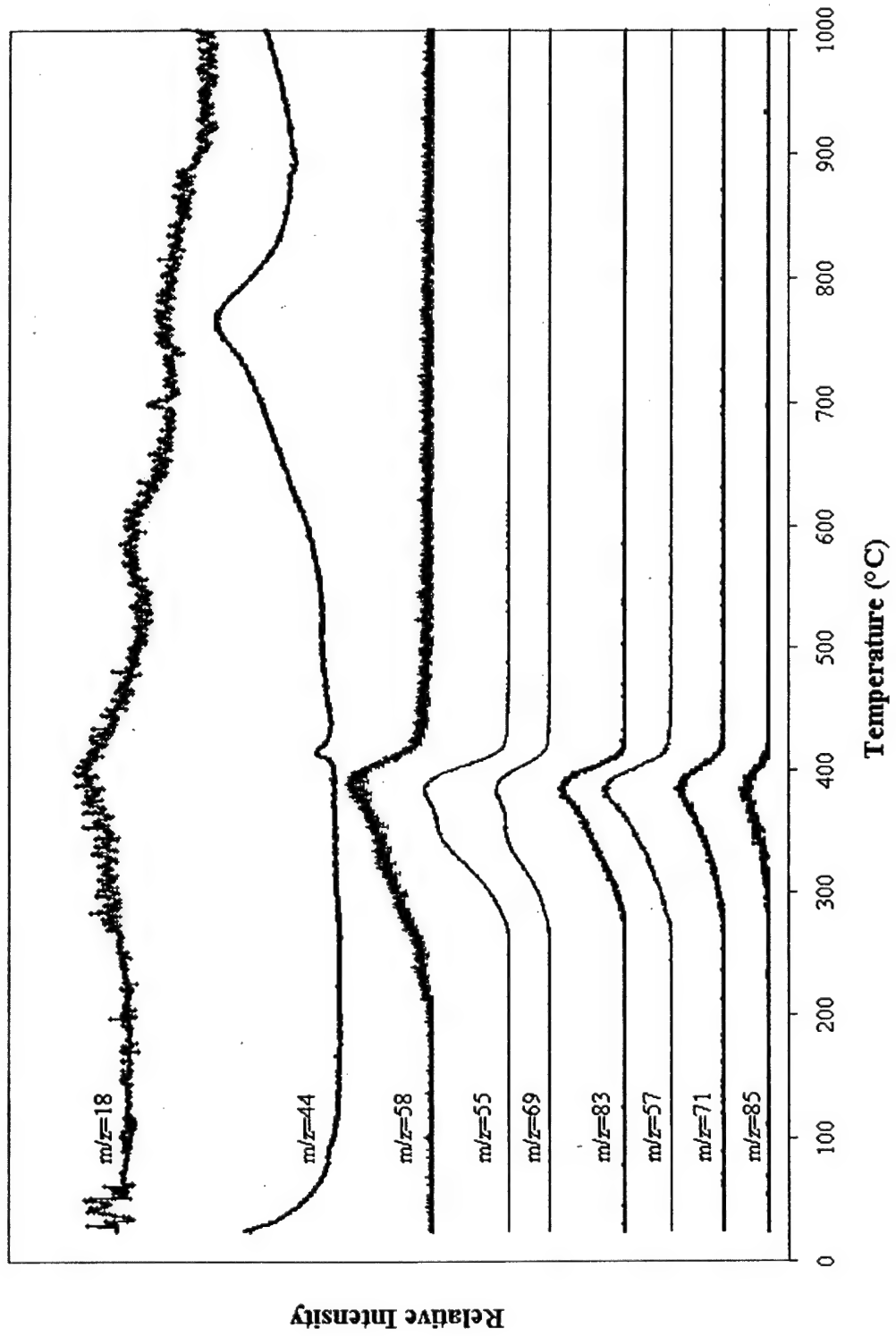


Figure 6. Temperature dependent MS results for the evolution products for N-C18.

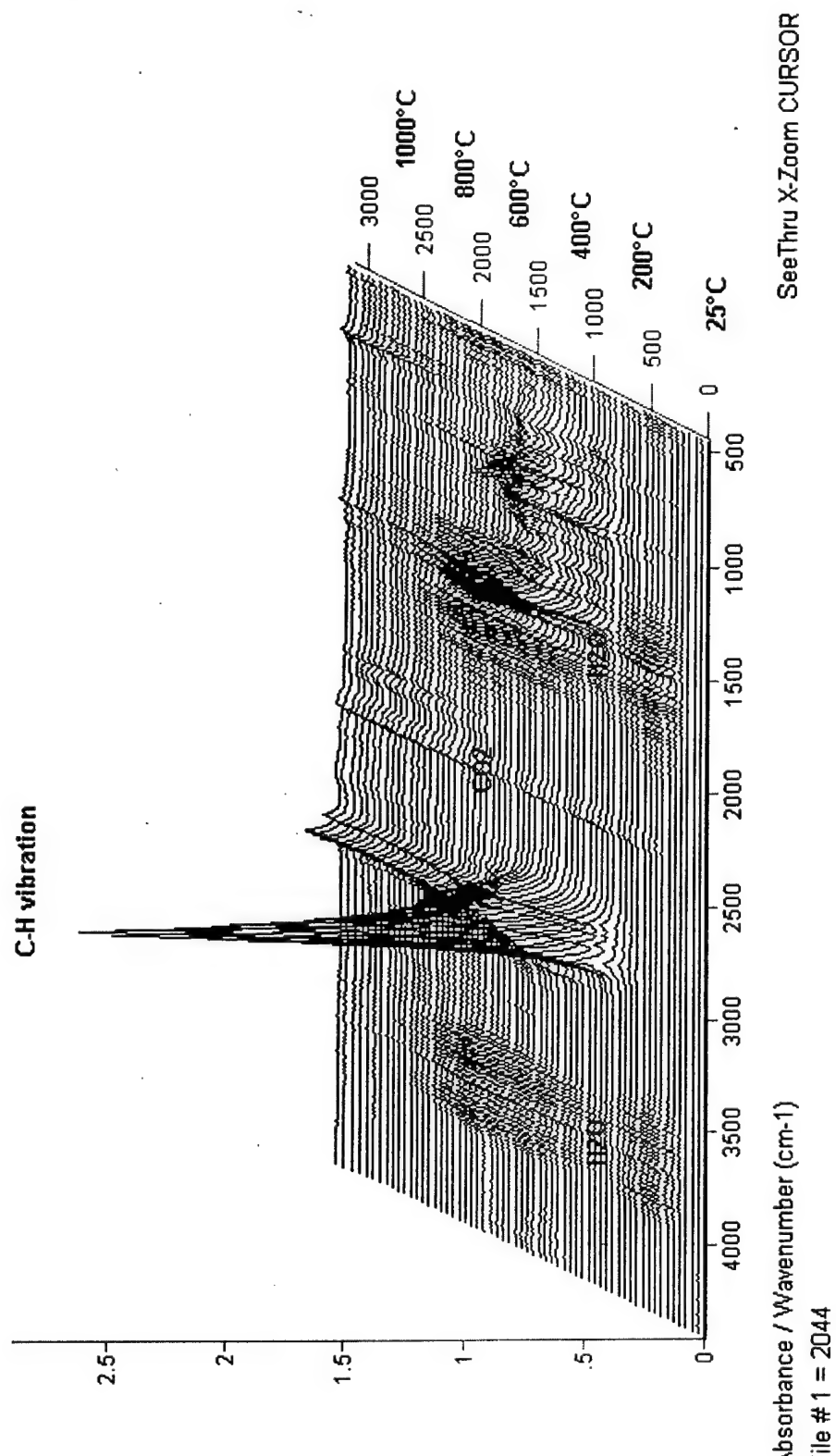


Figure 7. 3D FTIR results for the decomposition of N-CoCo.

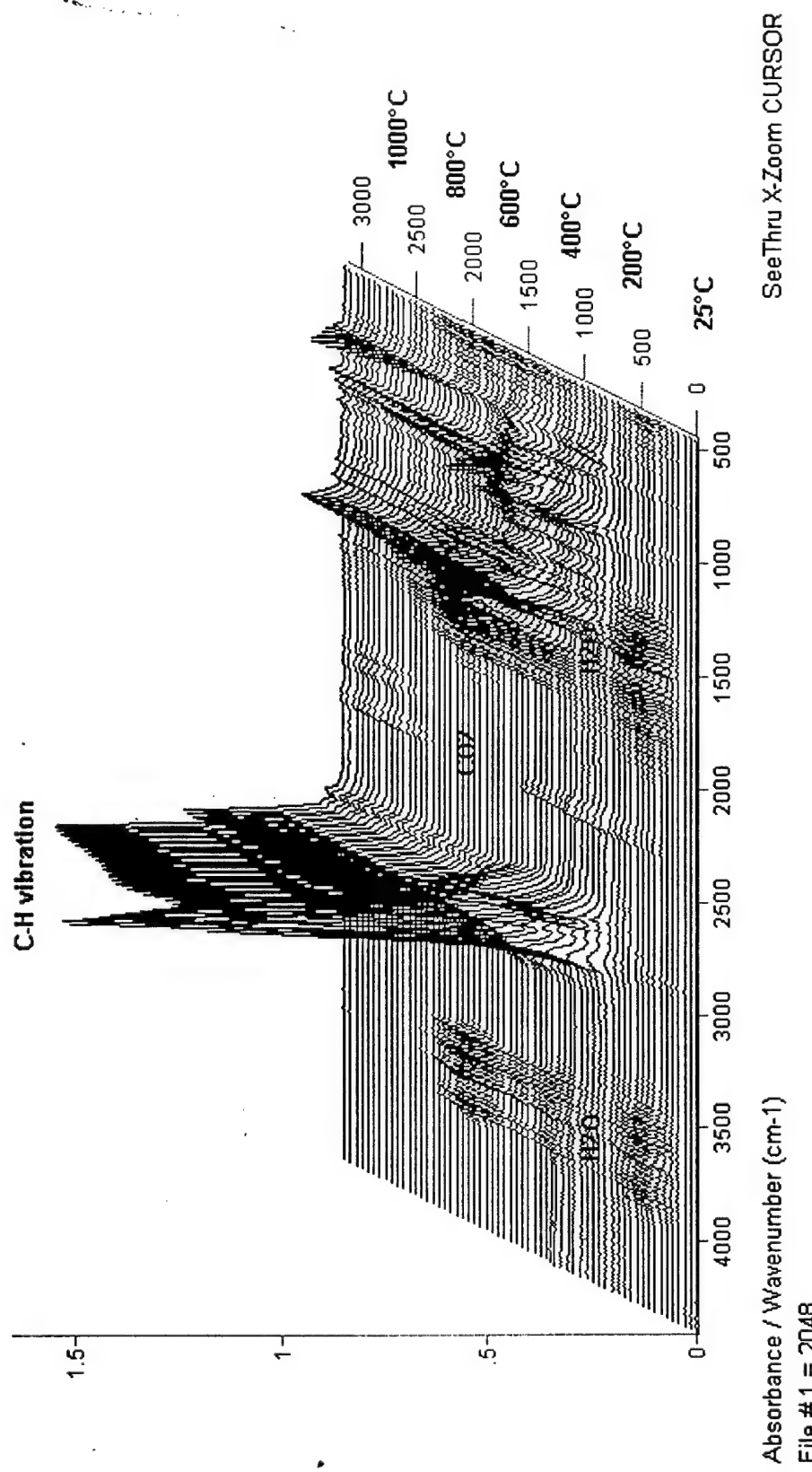


Figure 8. 3D FTIR results for the decomposition of N-C18.

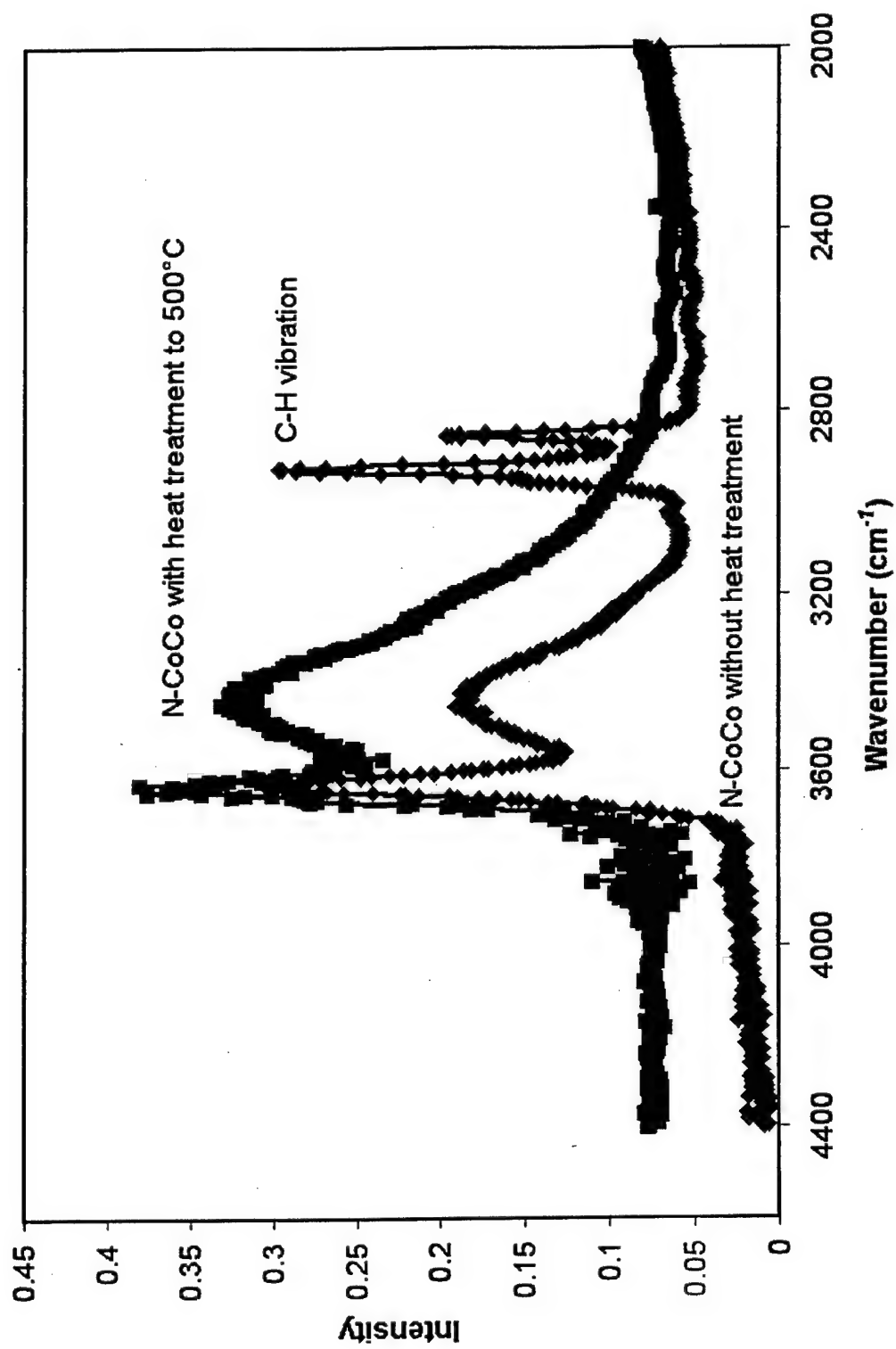


Figure 9. FTIR spectra of N-CoCo at 25°C and pyrolyzed at 500°C.

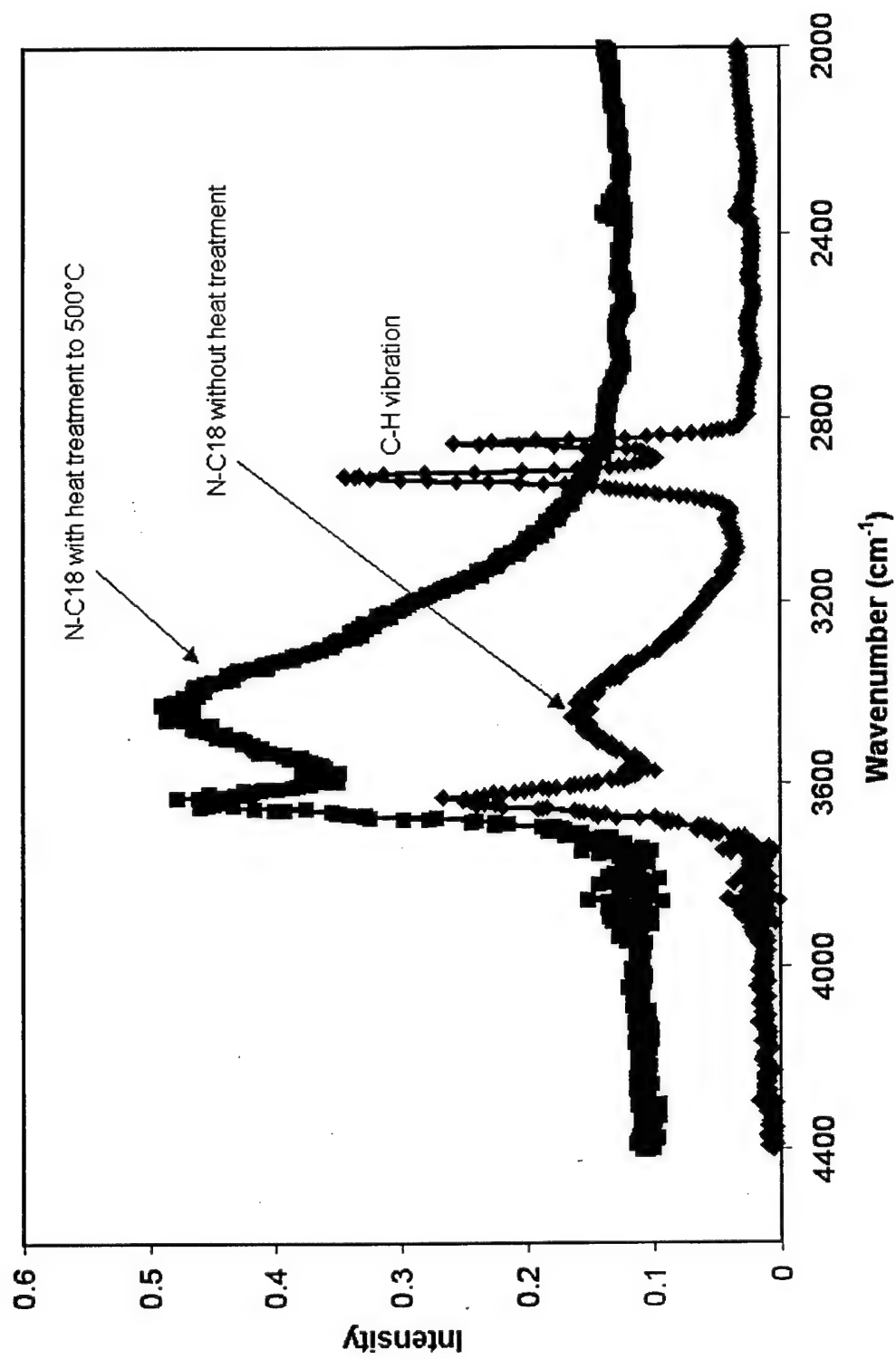


Figure 10. FTIR spectra of N-C18 at 25°C and pyrolyzed at 500°C.

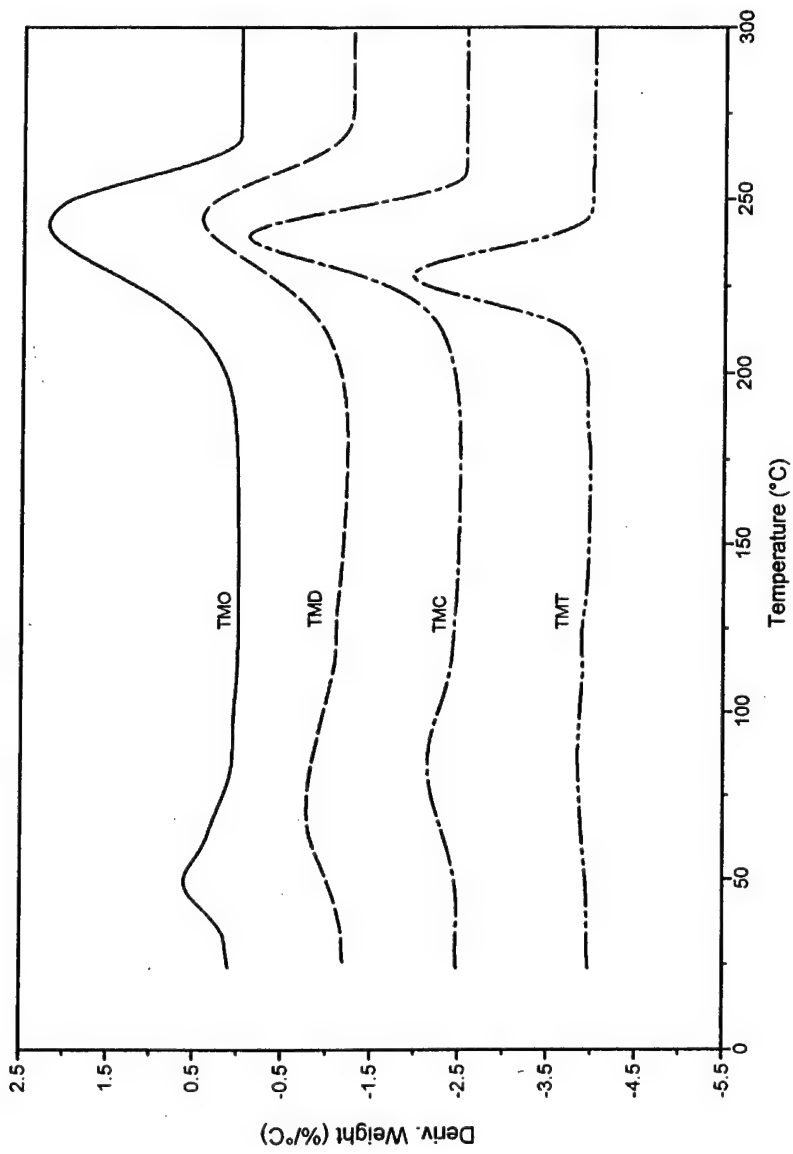


Figure 11. DTG curves from conventional TGA for trimethyl alkyl quaternary ammonium chlorides (TMO, TMD, TMC, and TMT).

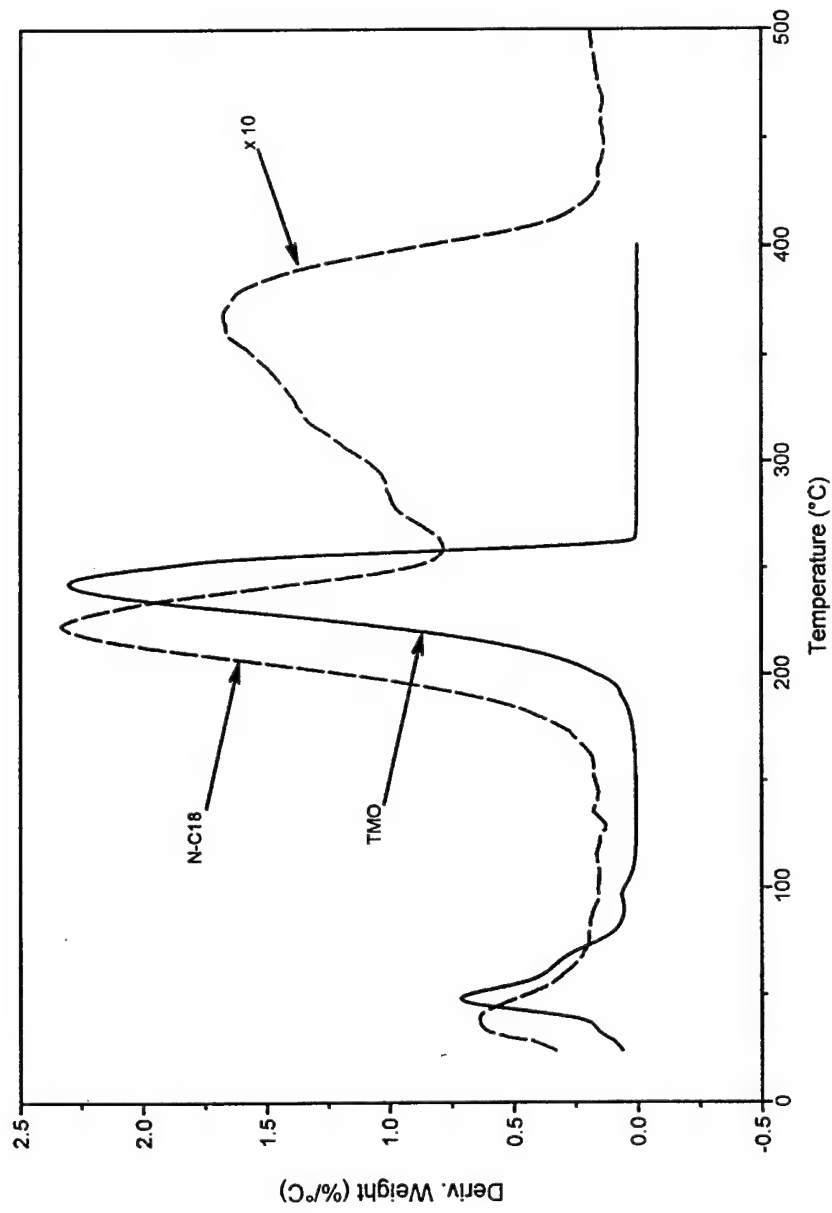


Figure 12. DTG curves comparing pure alkyl quaternary ammonium chloride (TMO) and the corresponding OLS (N-C18).

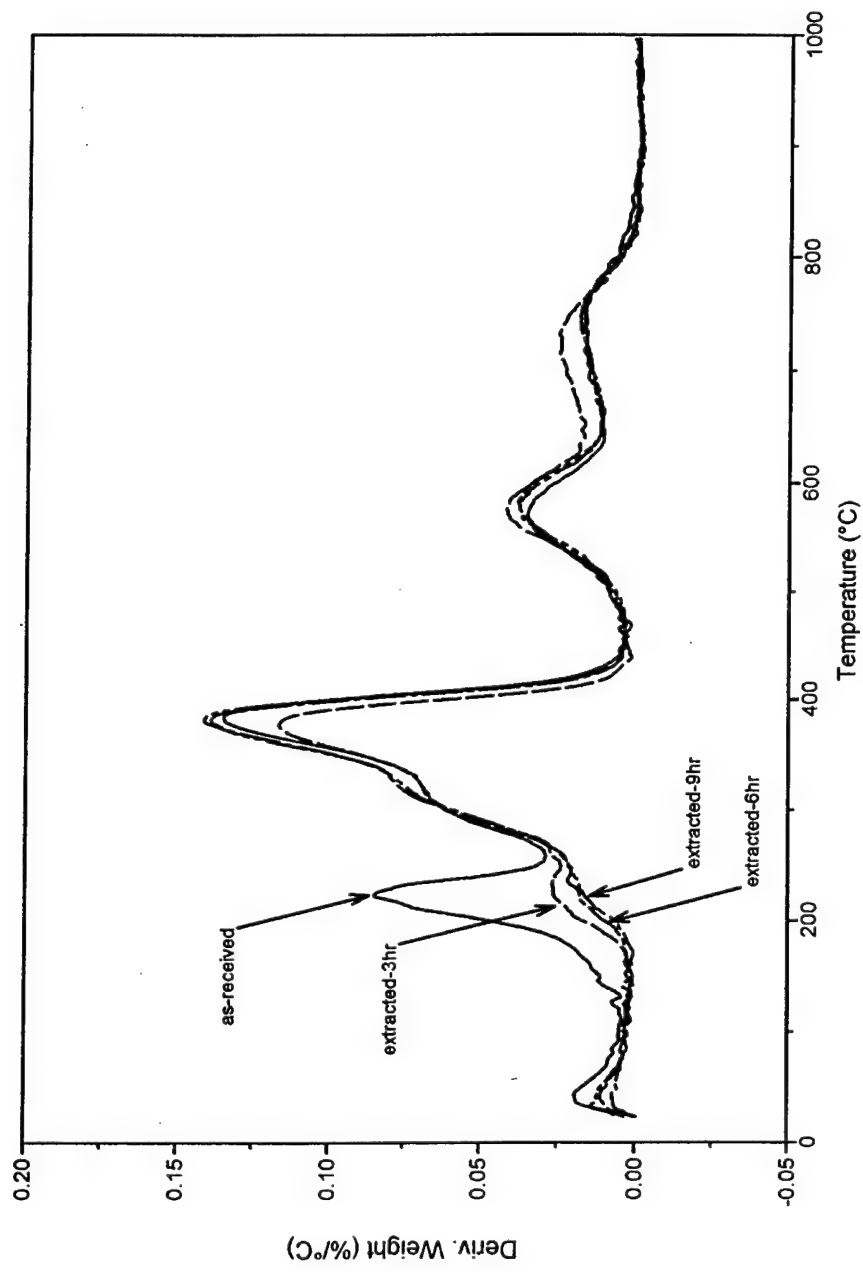


Figure 13. DTG curves for N-CoCo as-received and after 3, 6, and 9 hours of Soxhlet extraction with ethanol.

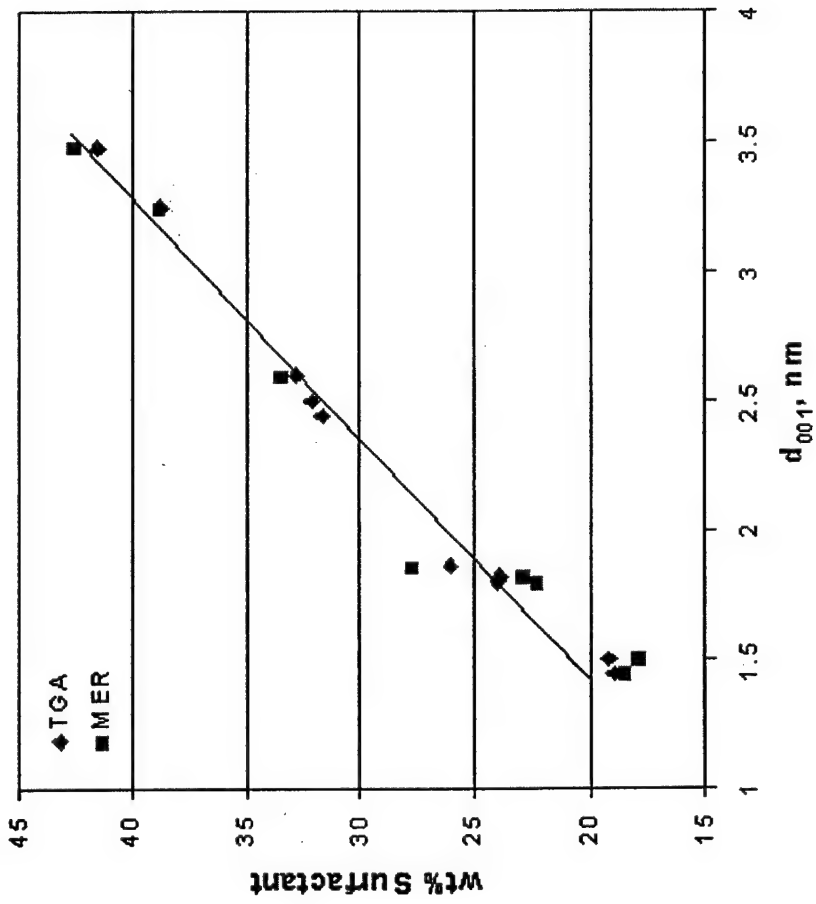


Figure 14. Comparison of the total organic content experimentally determined from TGA and predicted from MER with regards to the interlayer spacing determined from X-ray diffraction.

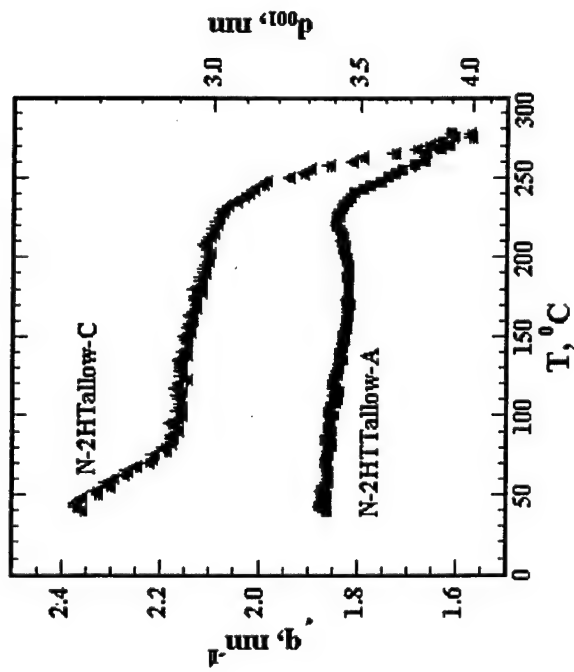


Figure 15. In situ small angle scattering from the degradation of N-2Htallow-A and N-2Htallow-C (position of basal reflection).

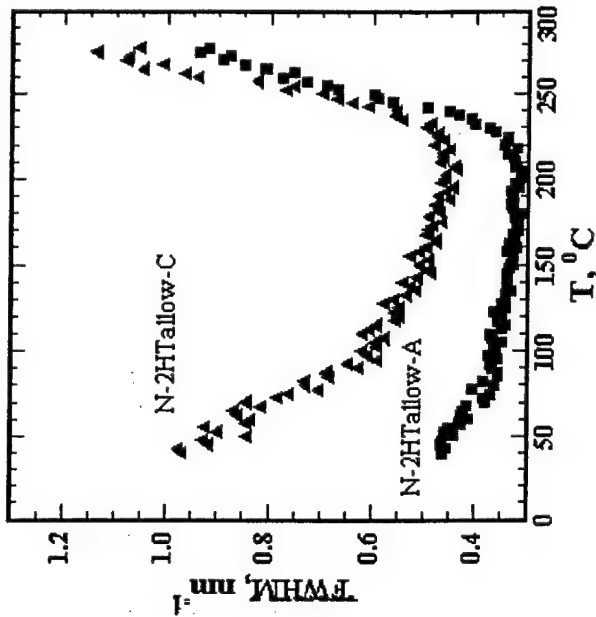


Figure 16. In situ small angle scattering from the degradation of N-2Htallow-A and N-2Htallow-C (FWHM of basal reflection).

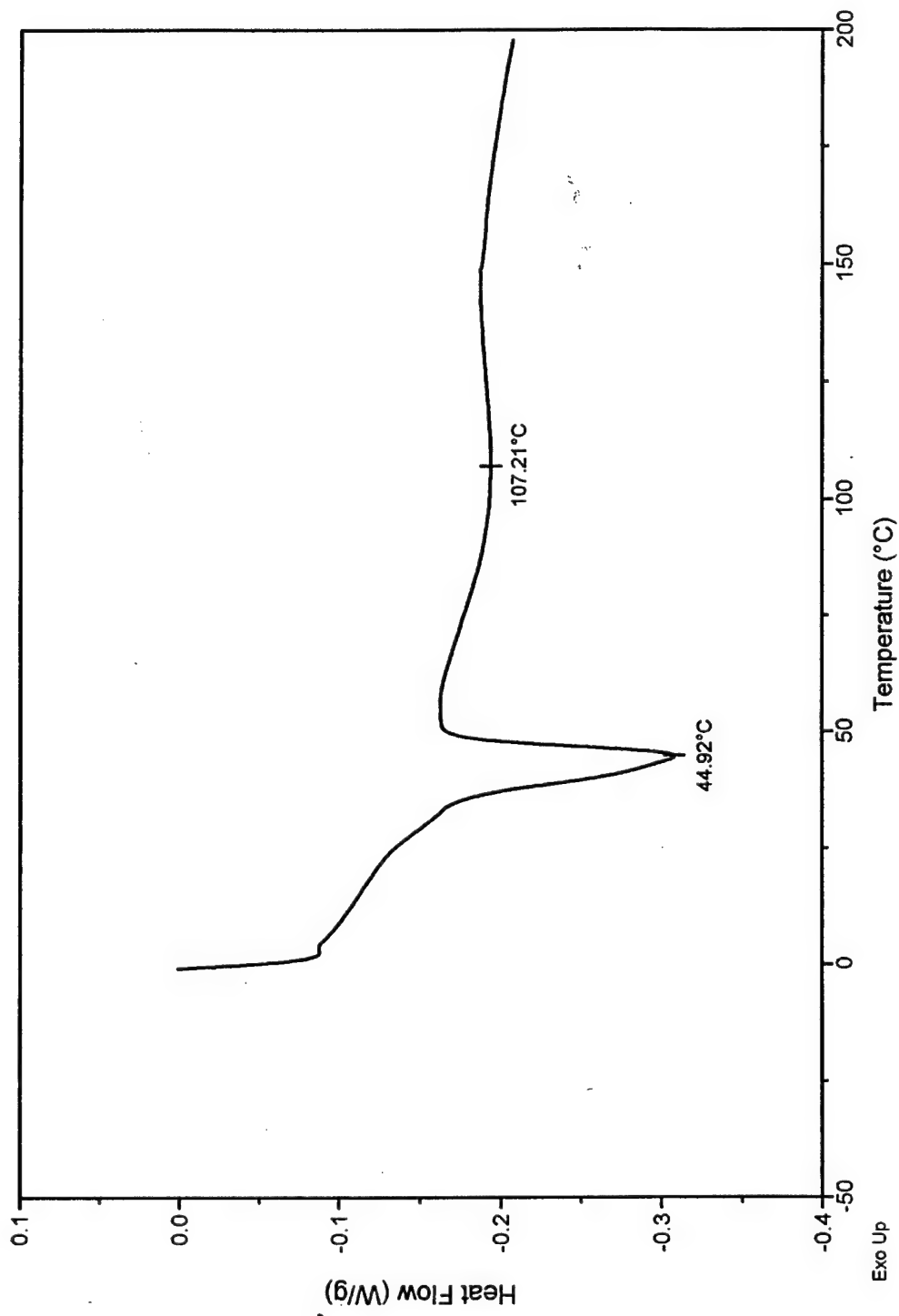


Figure 17. DSC curve of N-2HTallow-C from heating at 5°C/min.

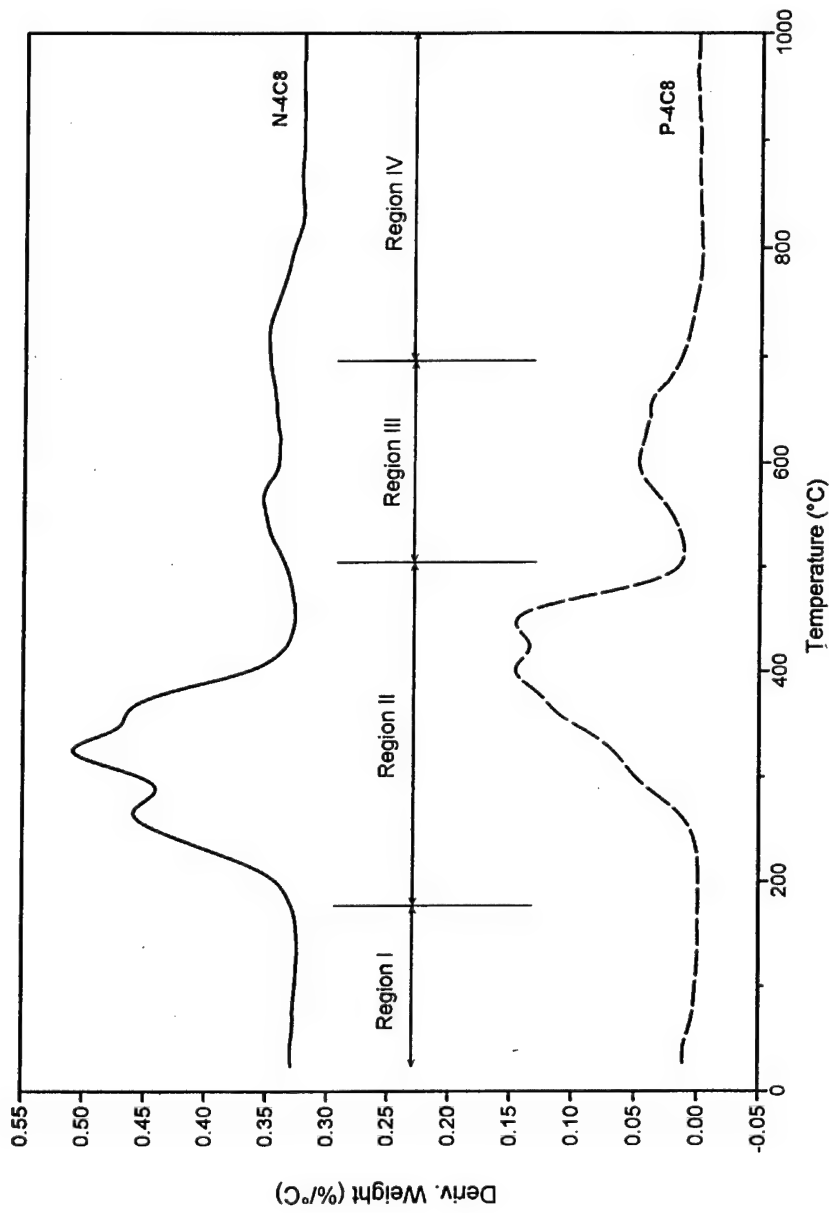


Figure 18. DTG curves comparing quaternary ammonium montmorillonite (N-4C8) and quaternary phosphonium montmorillonite (P-4C8).

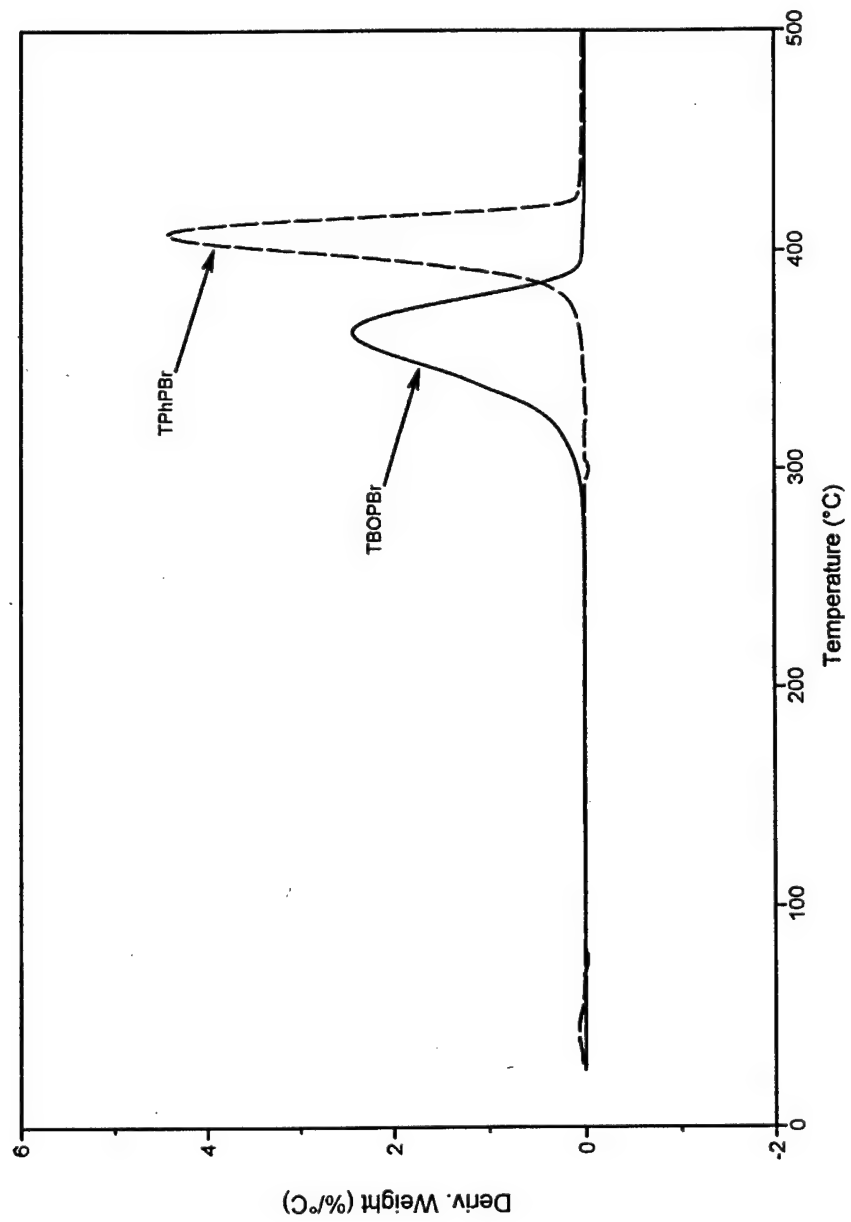


Figure 19. DTG curves from TGA studies of quaternary phosphonium bromides (TBOPBr and TPhPBr).

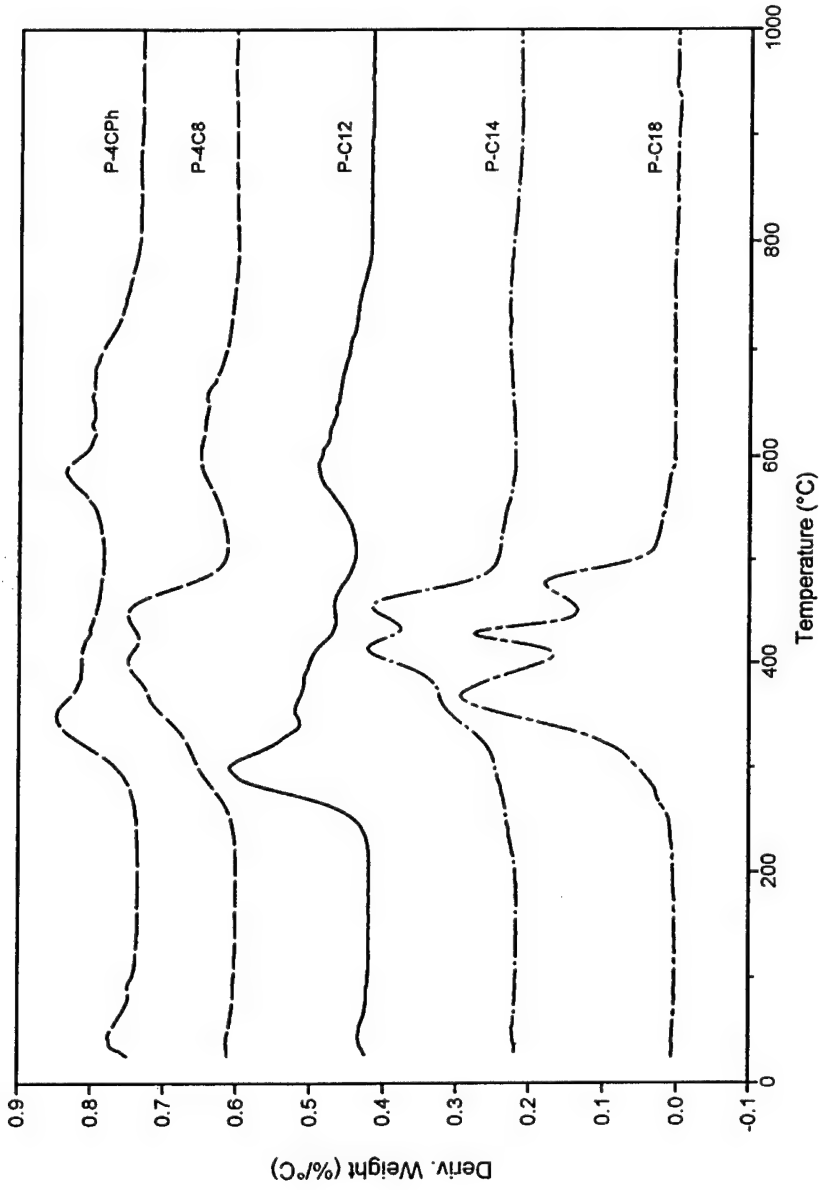


Figure 20. DTG curves from TGA studies of quaternary phosphonium montmorillonites (P-C12, P-C14, P-C16, P-C18, P-4Ph and P-4C8).

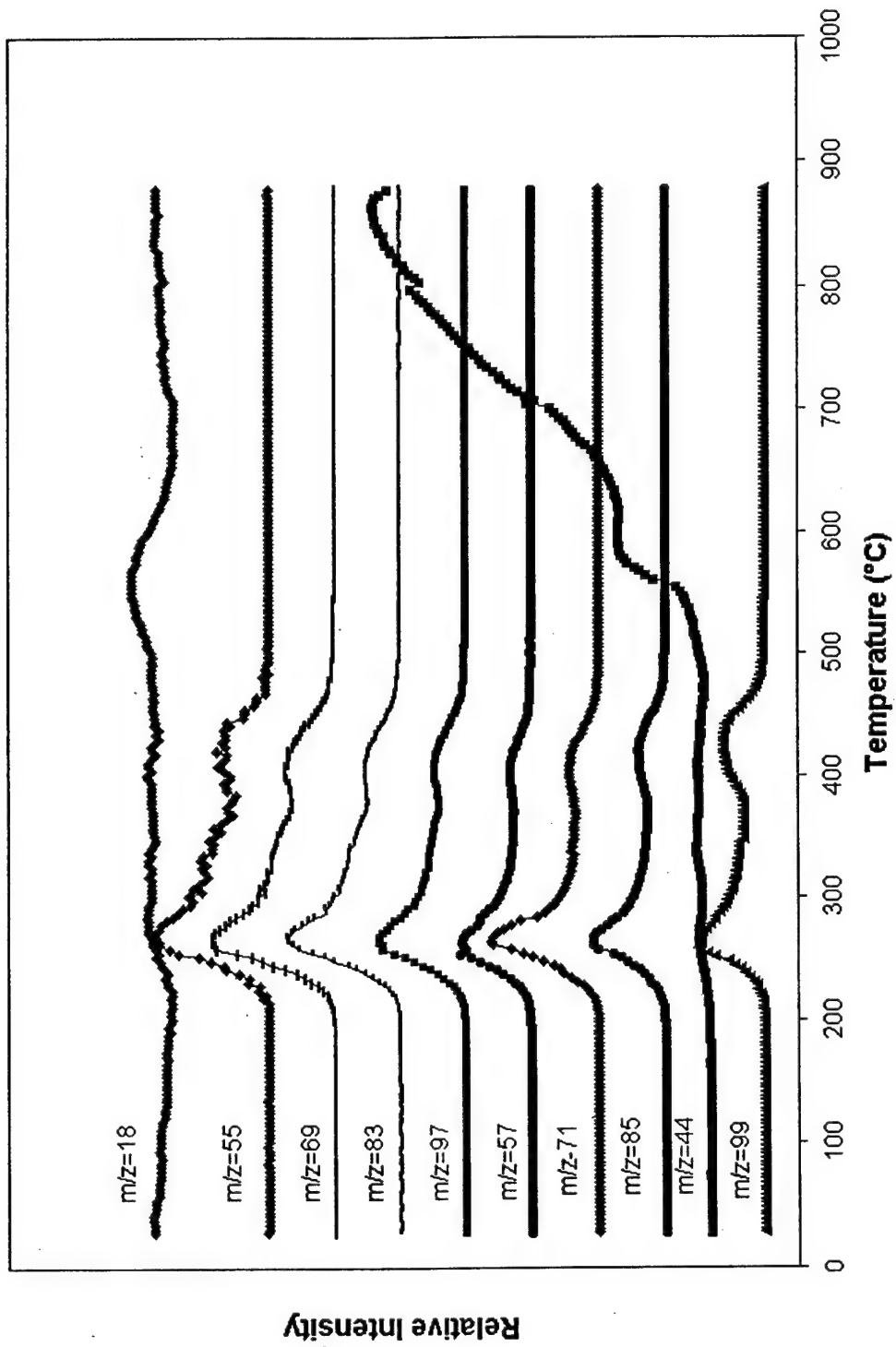


Figure 21. Temperature dependent MS results of the evolution products for P-C12.

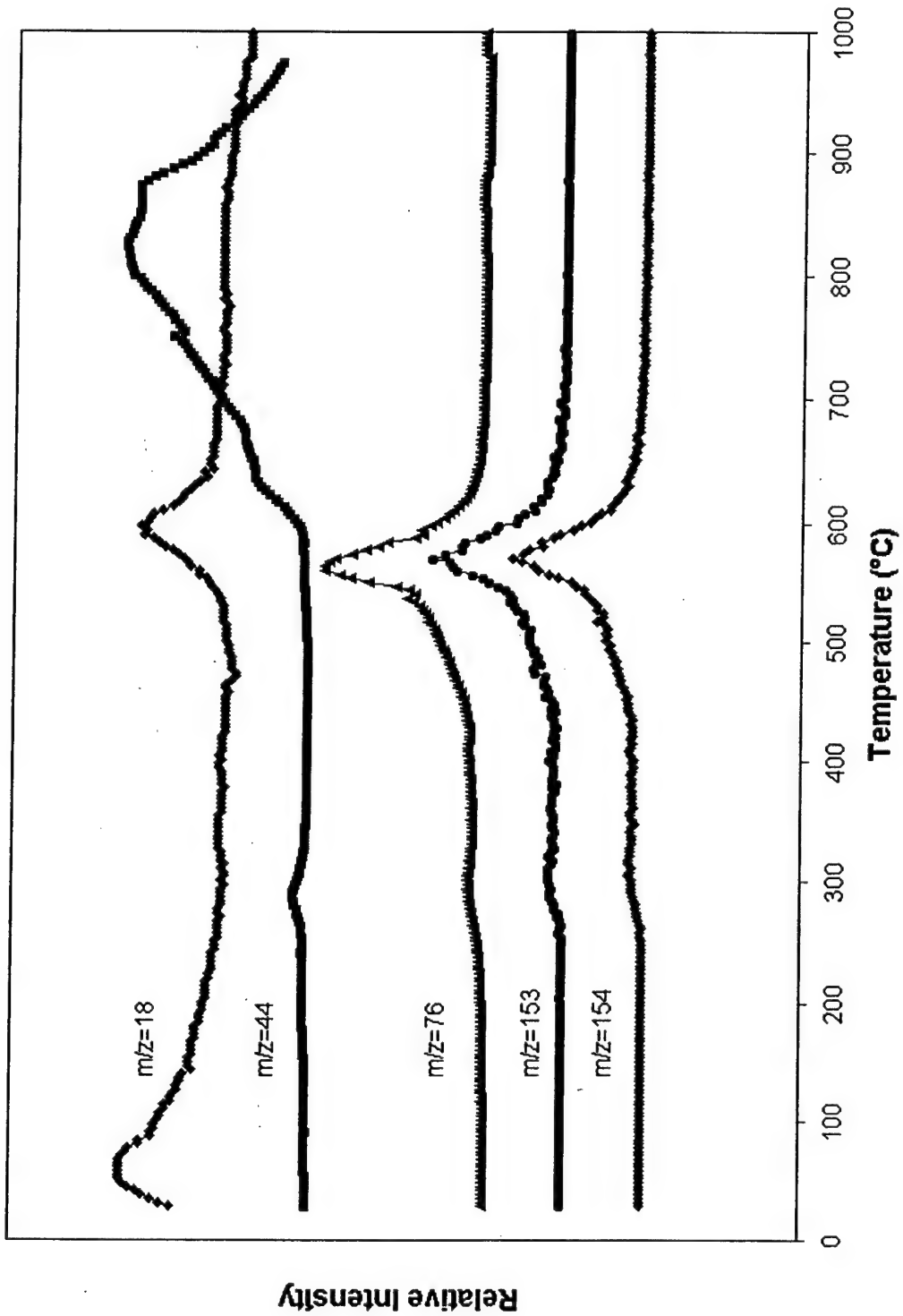


Figure 22. Temperature dependent MS results of the evolution products for P-4Ph.

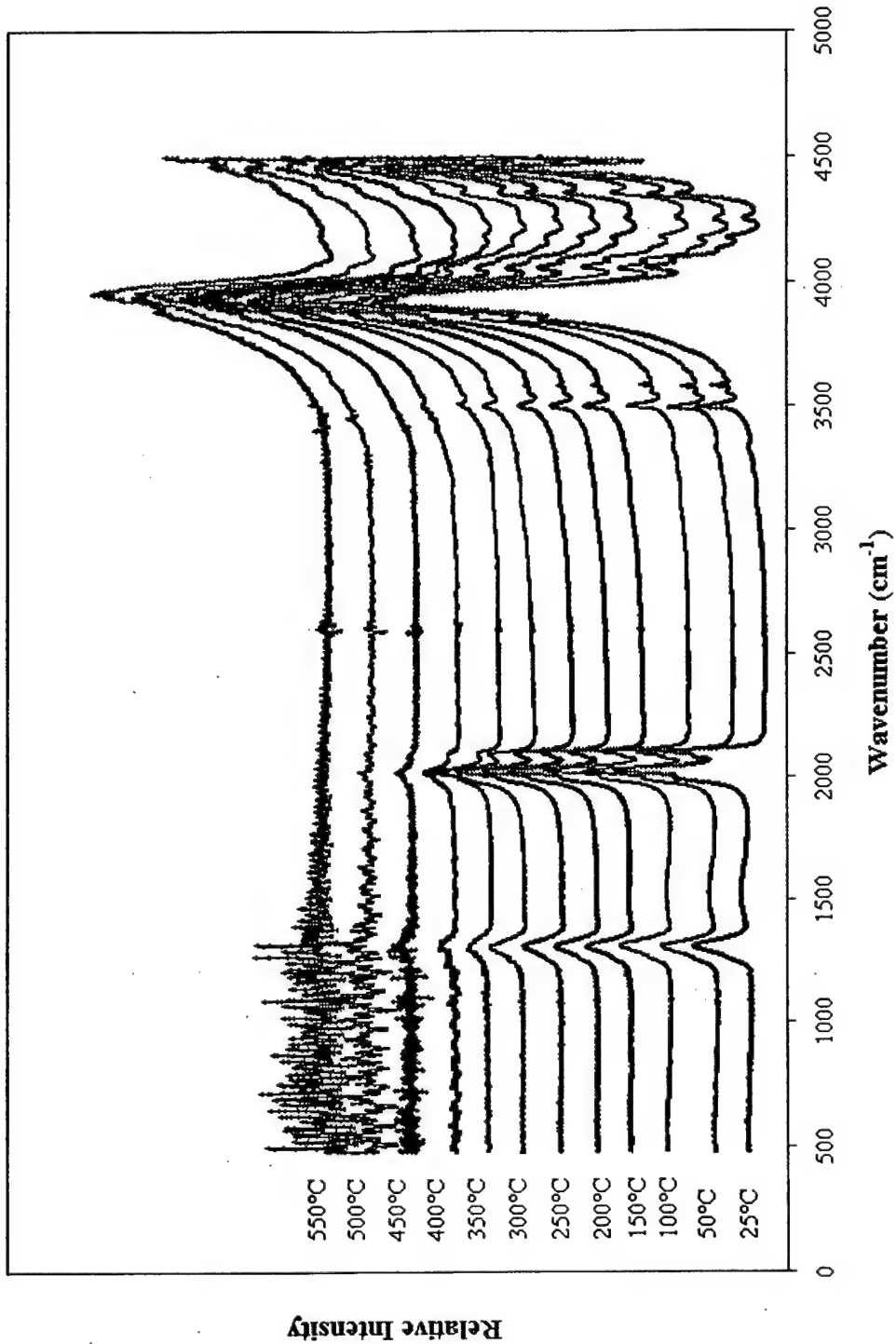


Figure 23. Temperature dependent FTIR evolution spectra for P-C18.

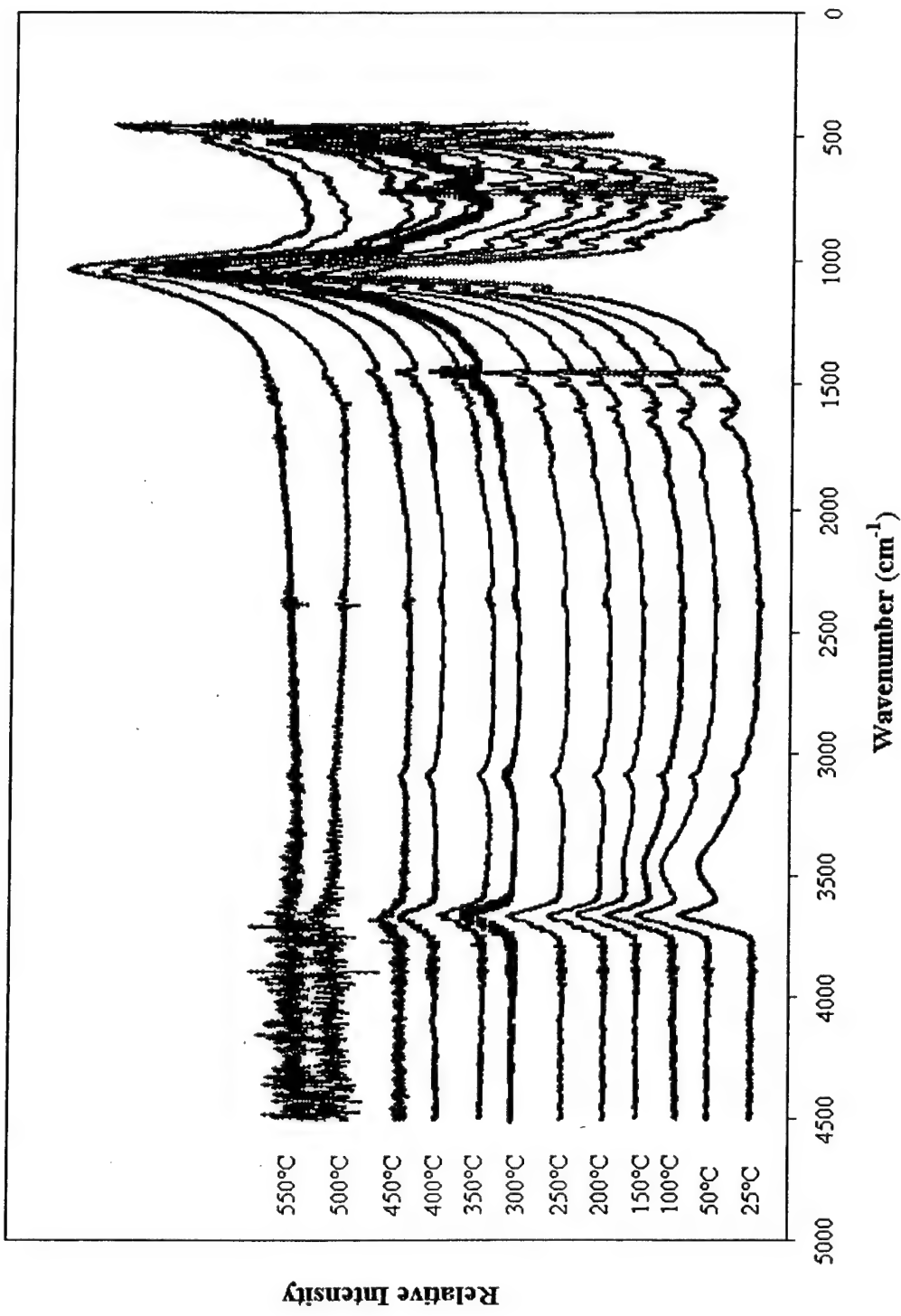


Figure 24. Temperature dependent FTIR evolution spectra for P-4Ph.

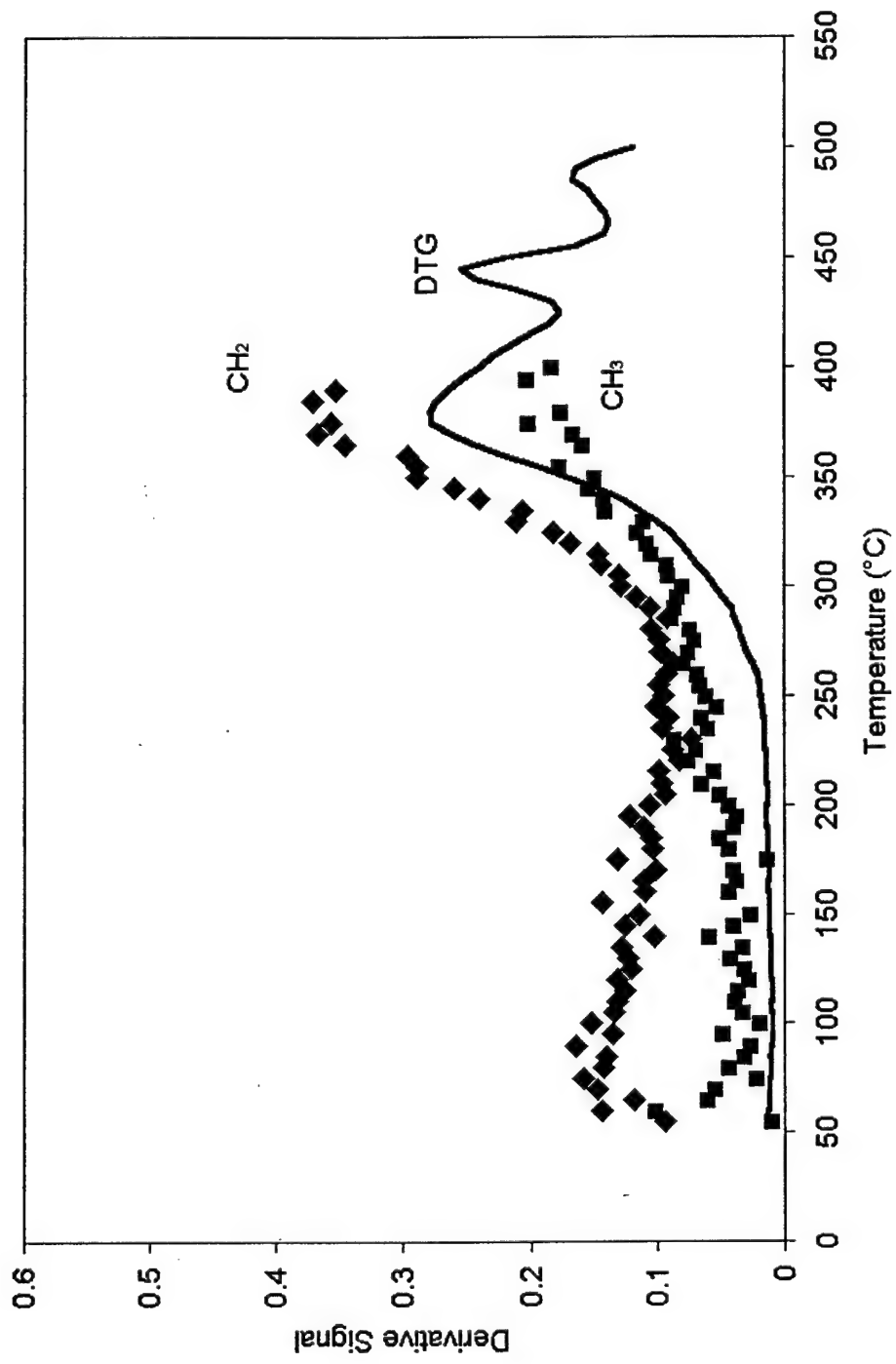


Figure 25. Comparison of the relative rate of change (derivative) of the mass loss (DTG) and peak area (FTIR: $\text{CH}_2 = v_{\text{as}}\text{CH}_2$ and $\text{CH}_3 = v_{\text{as}}\text{CH}_3$ and $v_s\text{CH}_3 = v_{\text{as}}\text{CH}_3$) for P-C18.

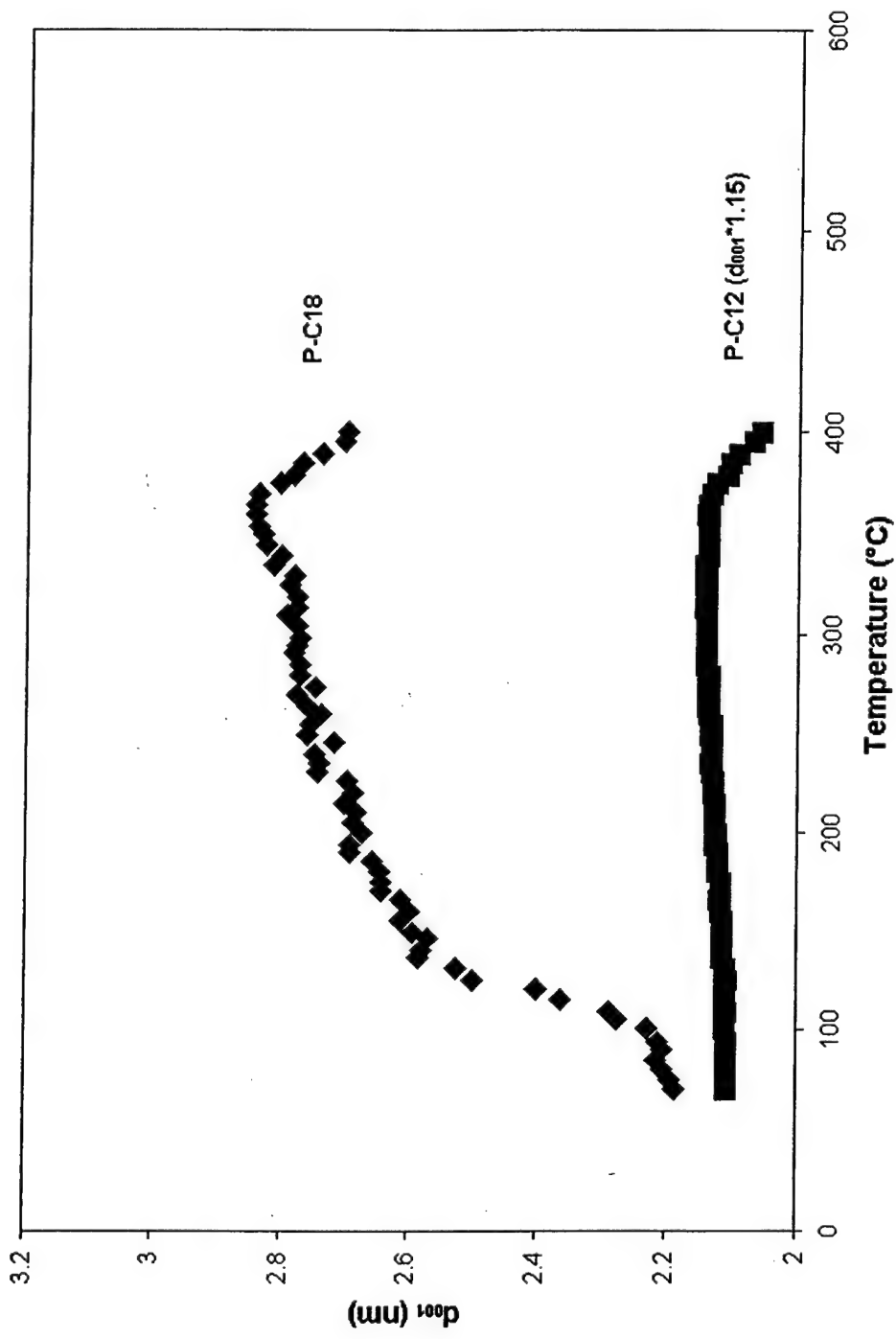


Figure 26. The change of layer distance (d_{001}) as a function of temperature from in-situ high temperature x-ray diffraction for P-C12 and P-C18.

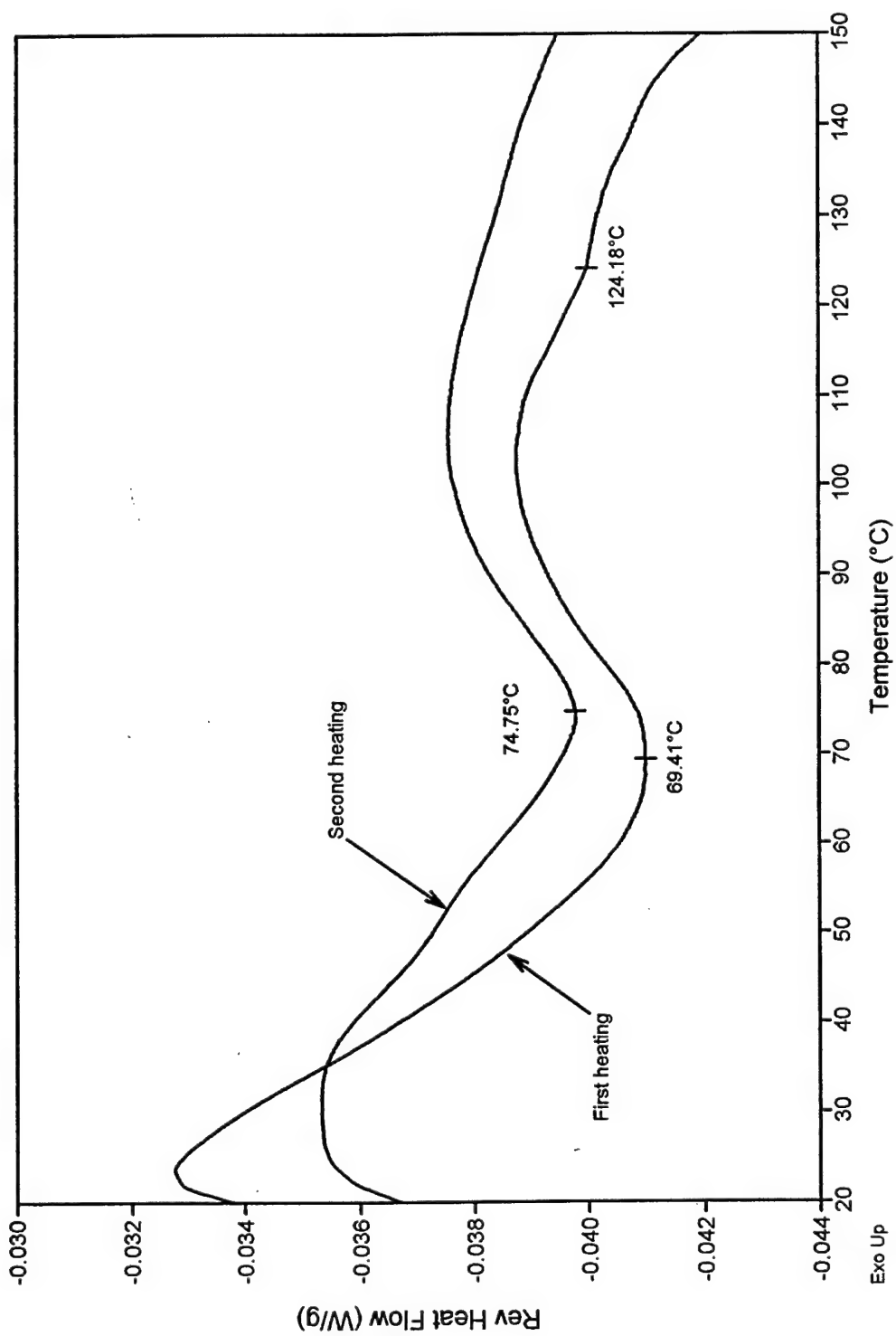


Figure 27. DSC result for P-C18.

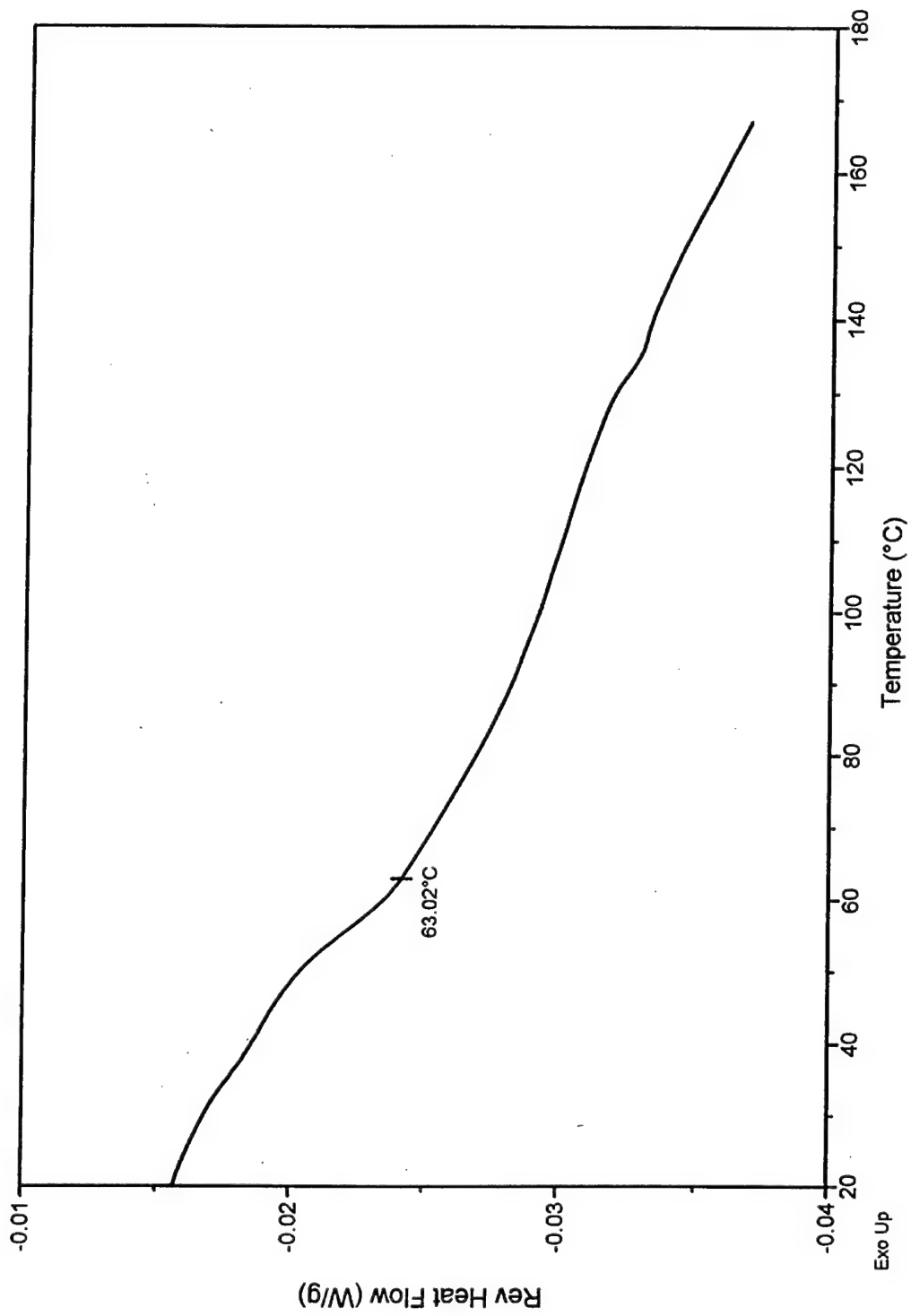


Figure 28. DSC result for P-C12.

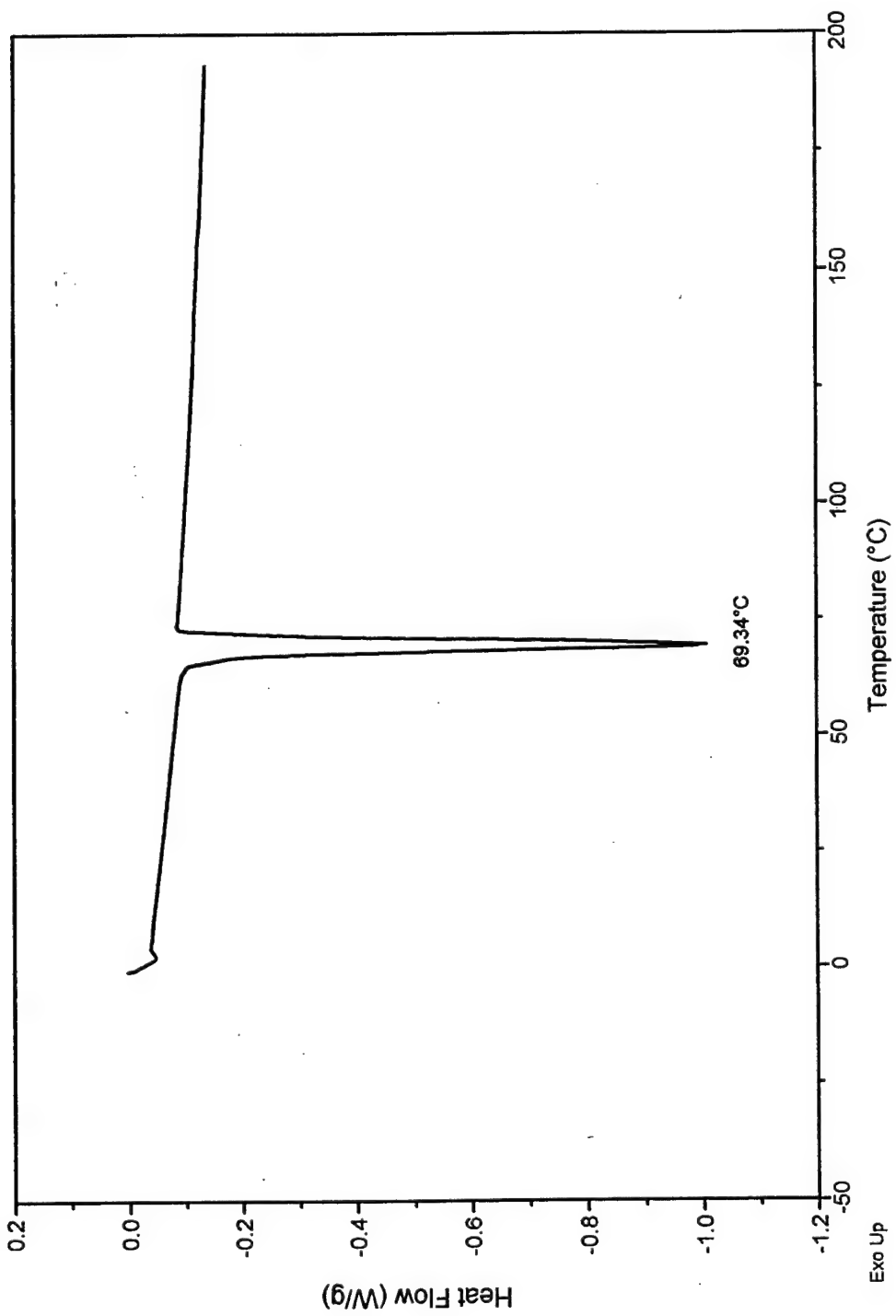


Figure 29. DSC result for TBOPBr.

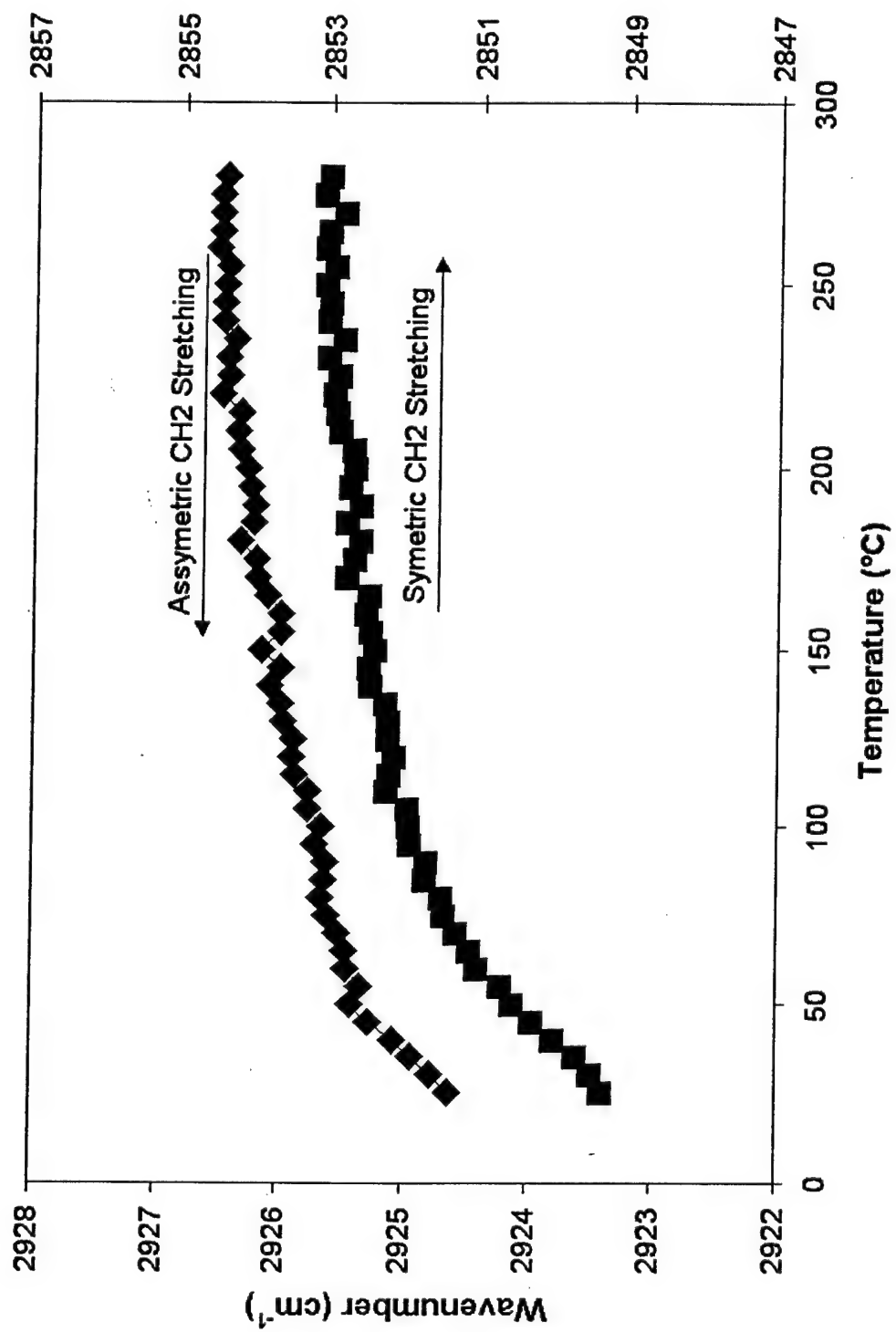


Figure 30. Change in $\nu_{\text{as}}(\text{CH}_2)$ and $\nu_s(\text{CH}_2)$ for P-C18 as a function of temperature.

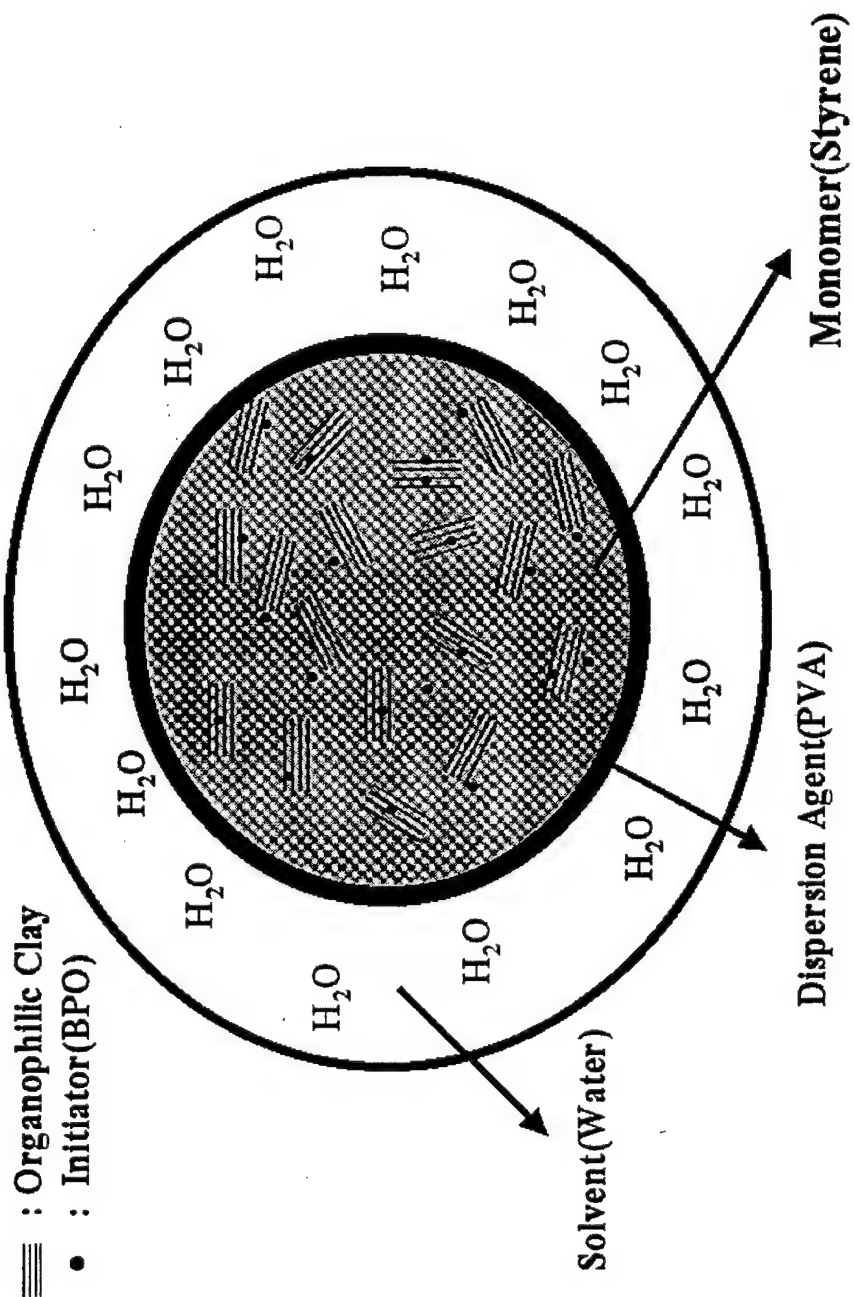


Figure 31. The reaction system of PS-MMT nanocomposites through suspension polymerization.

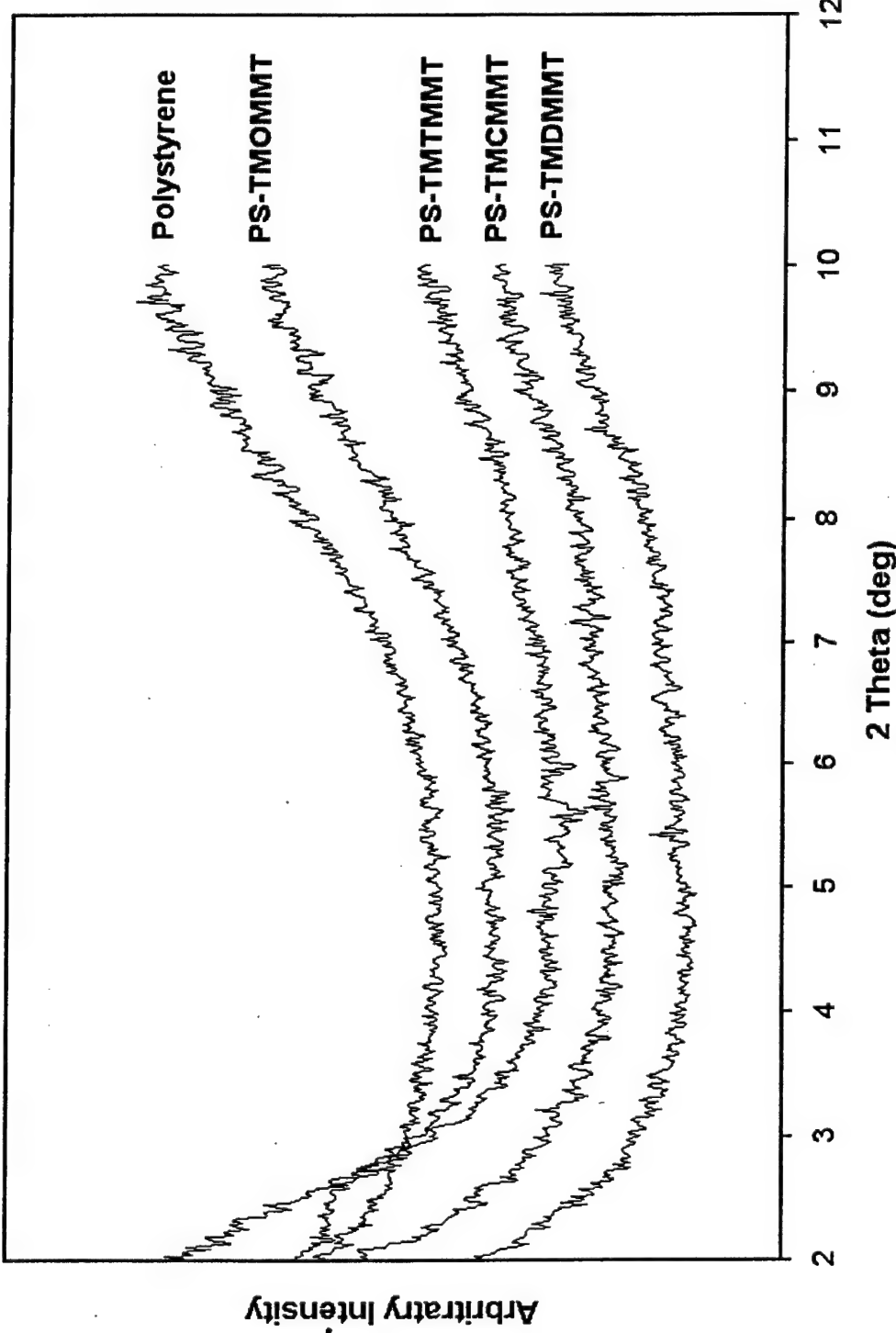


Figure 32. XRD curves of (a) Polystyrene, and (b) PS-TMOMMT, (c) PS-TMTMMT, (d) PS-TMCMMT, (e) PS-TMDMMT with 5.0 wt% of organo-MMT.



Magification=66000 (0.66nm=10nm)

Figure 33a. TEM image of PS-TMOMMT nanocomposite.



Magnification=66000 (0.66mm=10nm)

Figure 33b. TEM image of PS-TMDMMT nanocomposite.

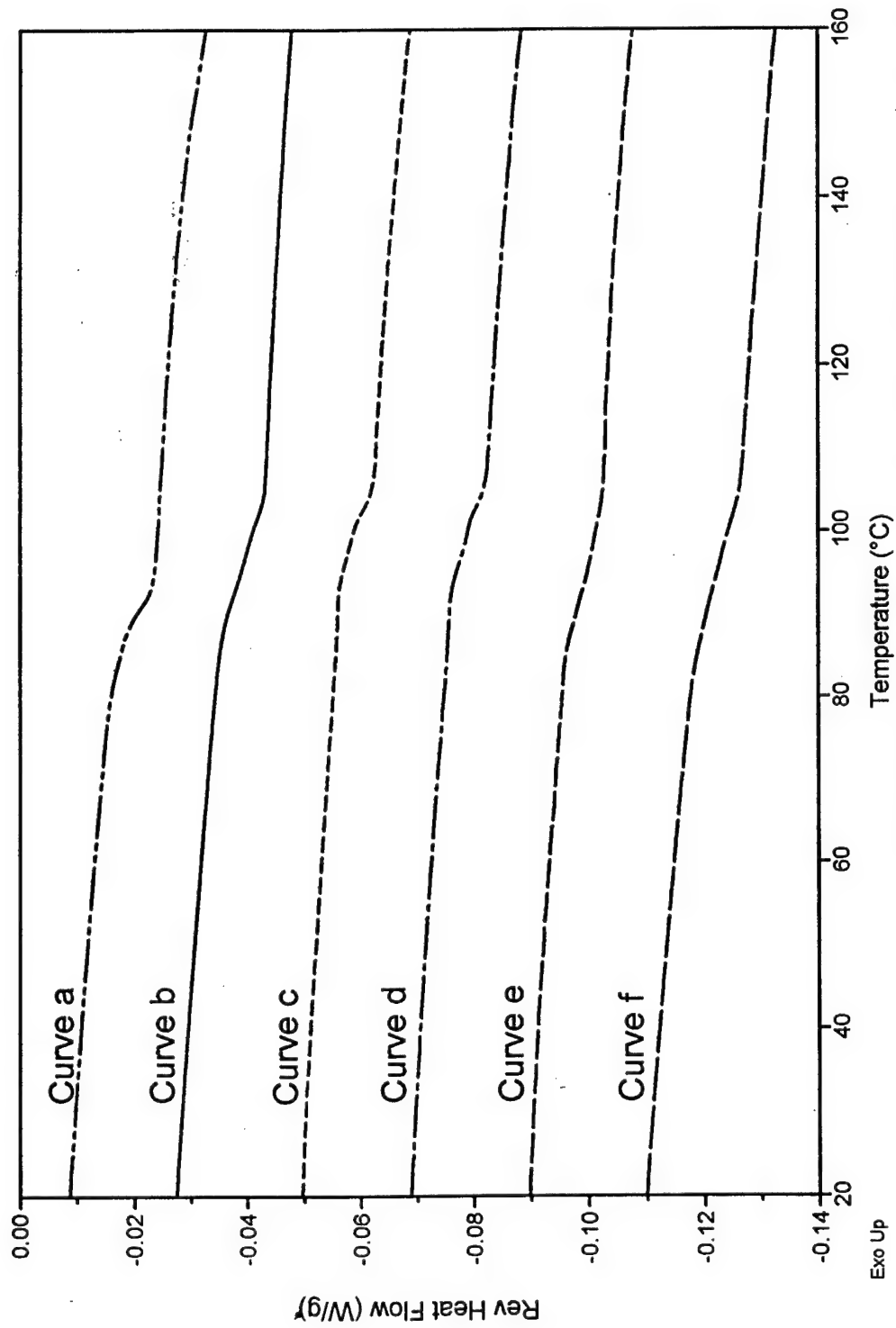


Figure 34. DSC curves of (a) Polystyrene, and PS-TMOMMT nanocomposites with different TMOMMT content (b) 1.0 wt%, (c) 2.5 wt%, (d) 5.0 wt%, (e) 7.5 wt%, (f) 10.0 wt%.

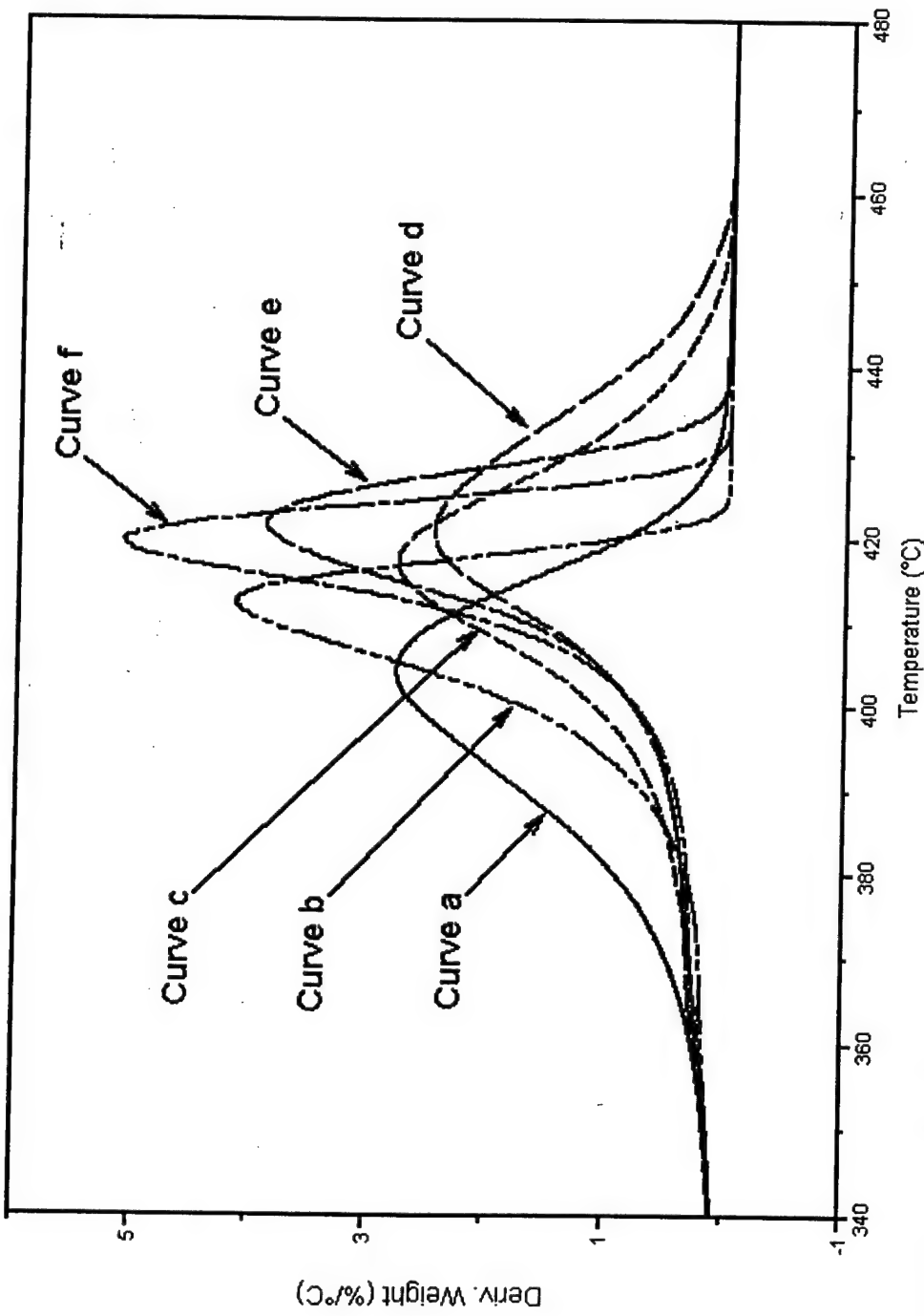


Figure 35. DTG curves of (a) Polystyrene, and PS-TMOMMT nanocomposites with different TMOMMT content (b) 1.0 wt%, (c) 2.5 wt%, (d) 5.0 wt%, (e) 7.5 wt%, (f) 10.0 wt%.

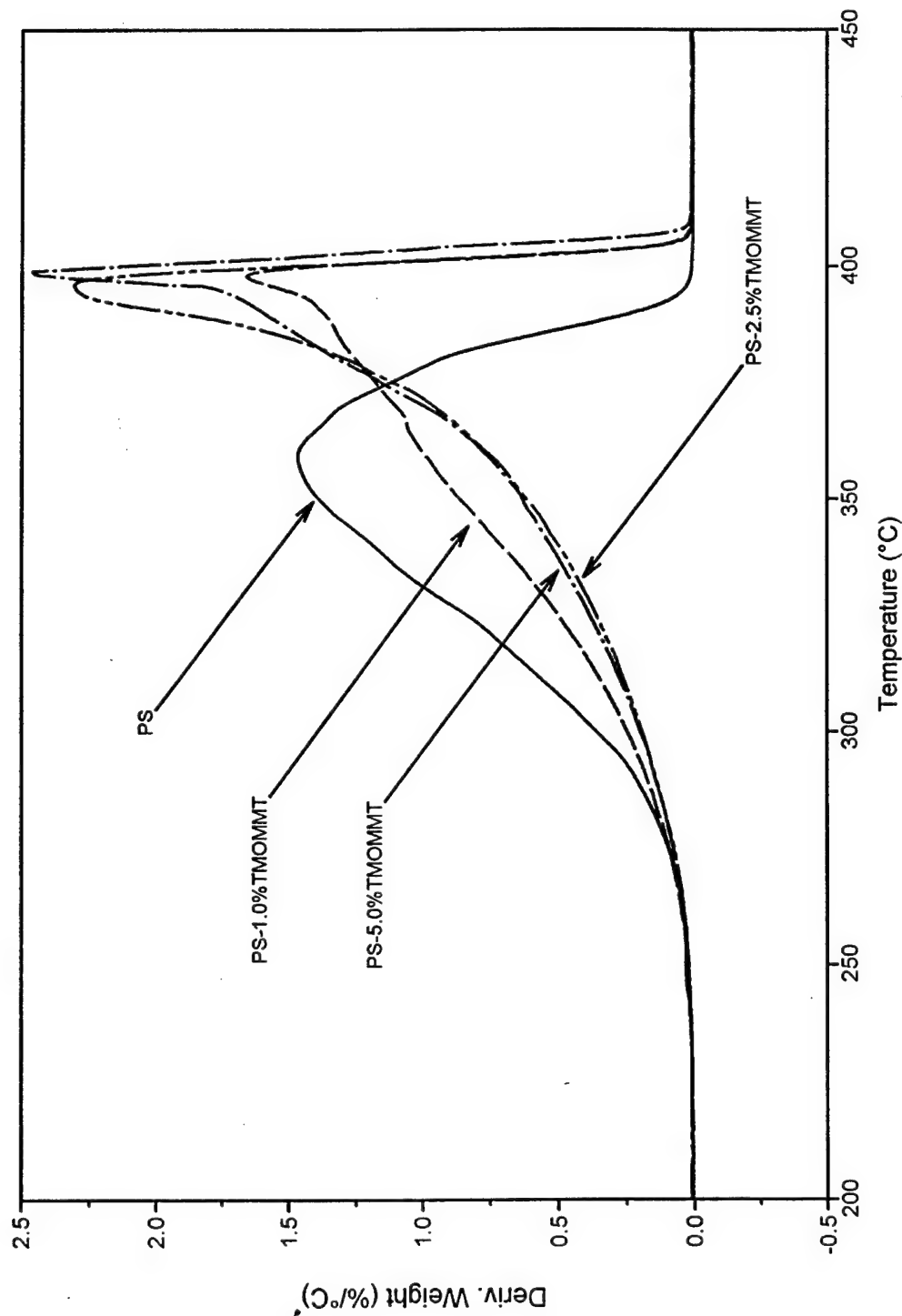


Figure 36. DTG curves of PS and PS-TMOMMT nanocomposites with different TMOMMT contents in an air atmosphere.

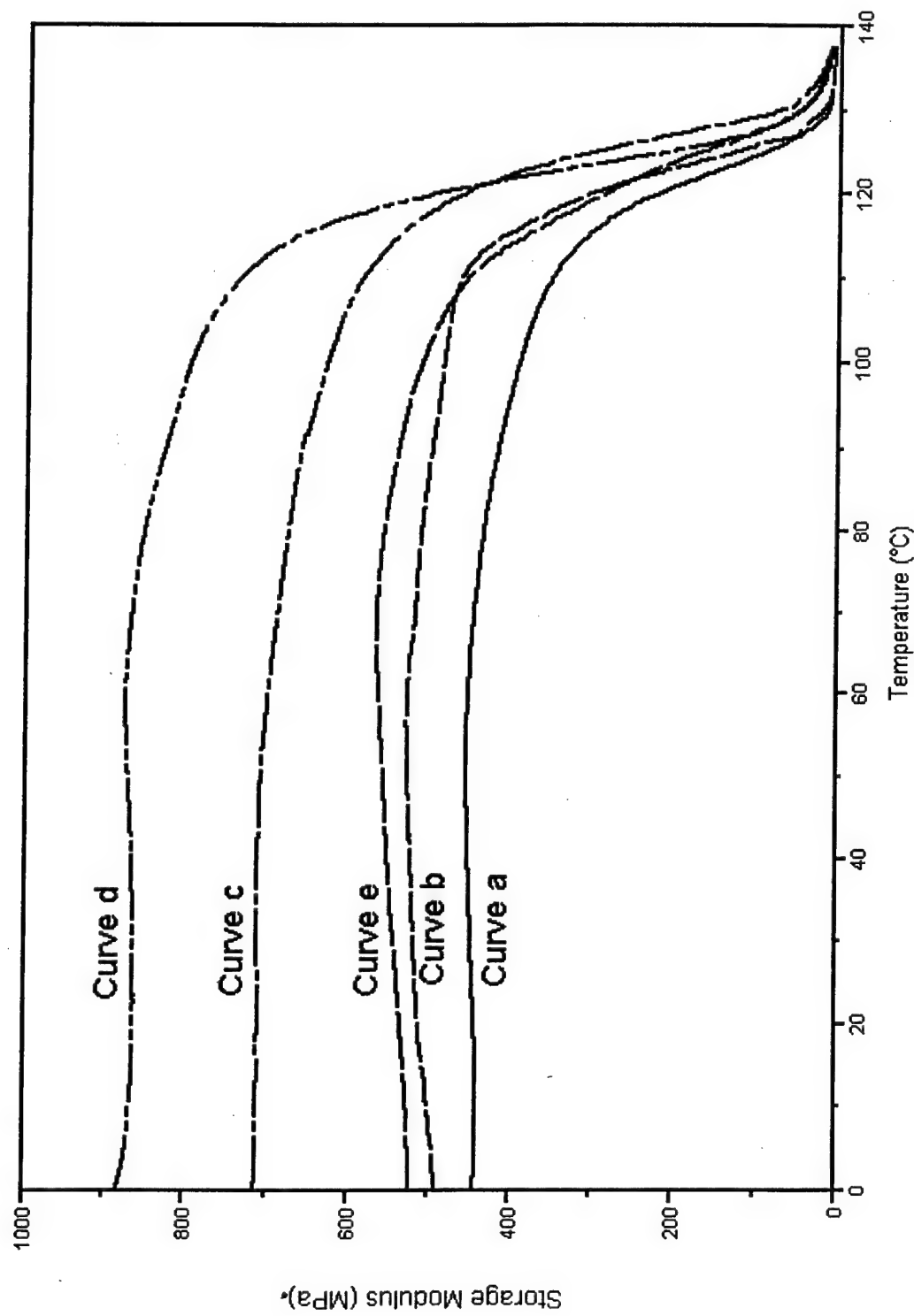


Figure 37. DMA (storage modulus) curves of (a) Polystyrene, and PS-TMOMMT nanocomposites with different TMOMMT content (b) 2.5 wt%, (c) 5.0 wt%, (d) 7.5 wt%, (e) 10.0 wt%.

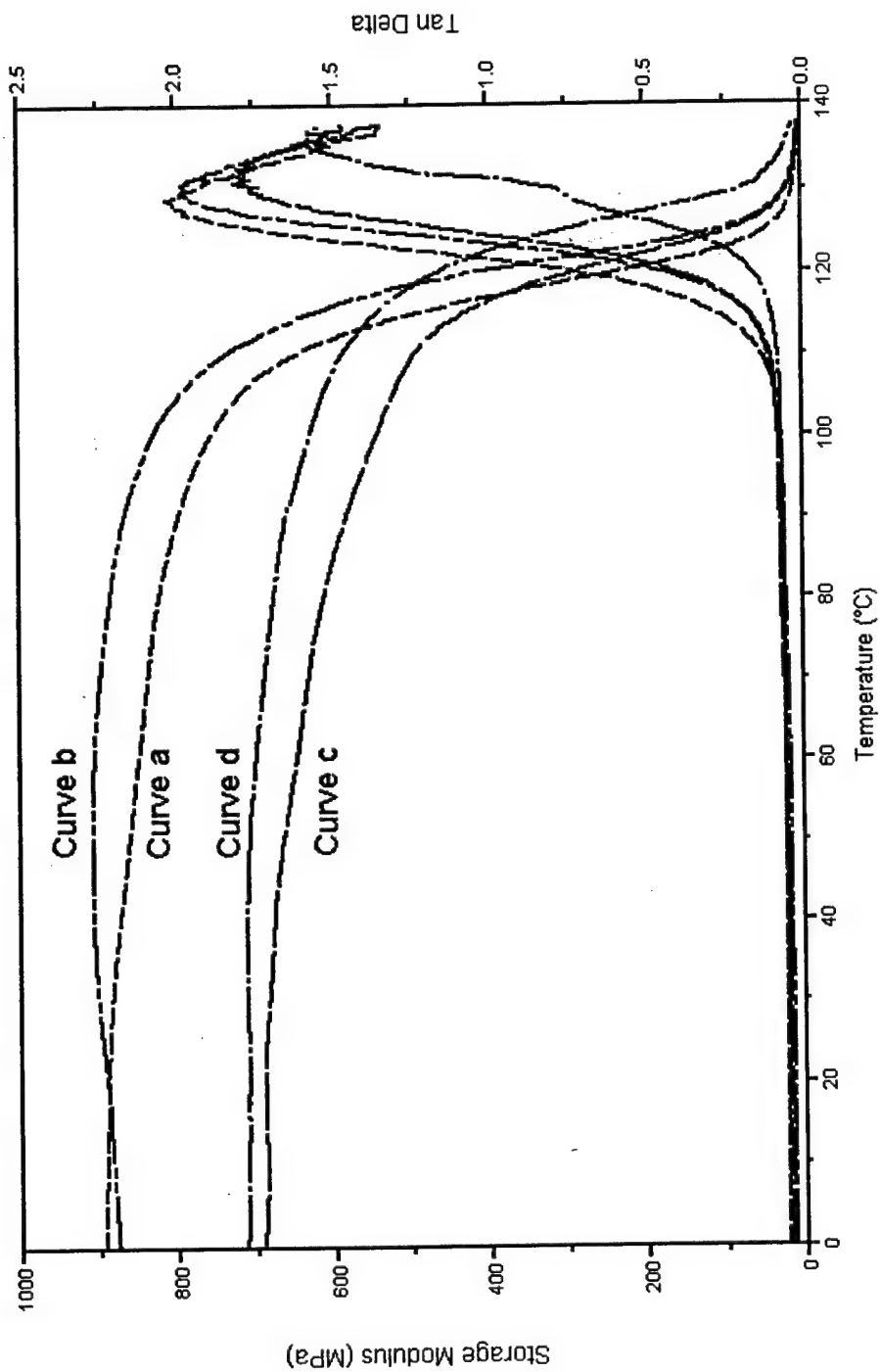


Figure 38. Comparison of DMA results of (a) PS-TMDMMT, (b) PS-TMCMMMT, (c) PS-TMTMMT, and (d) PS-TMOMMT nanocomposites with 5.0 wt% organo-MMT.

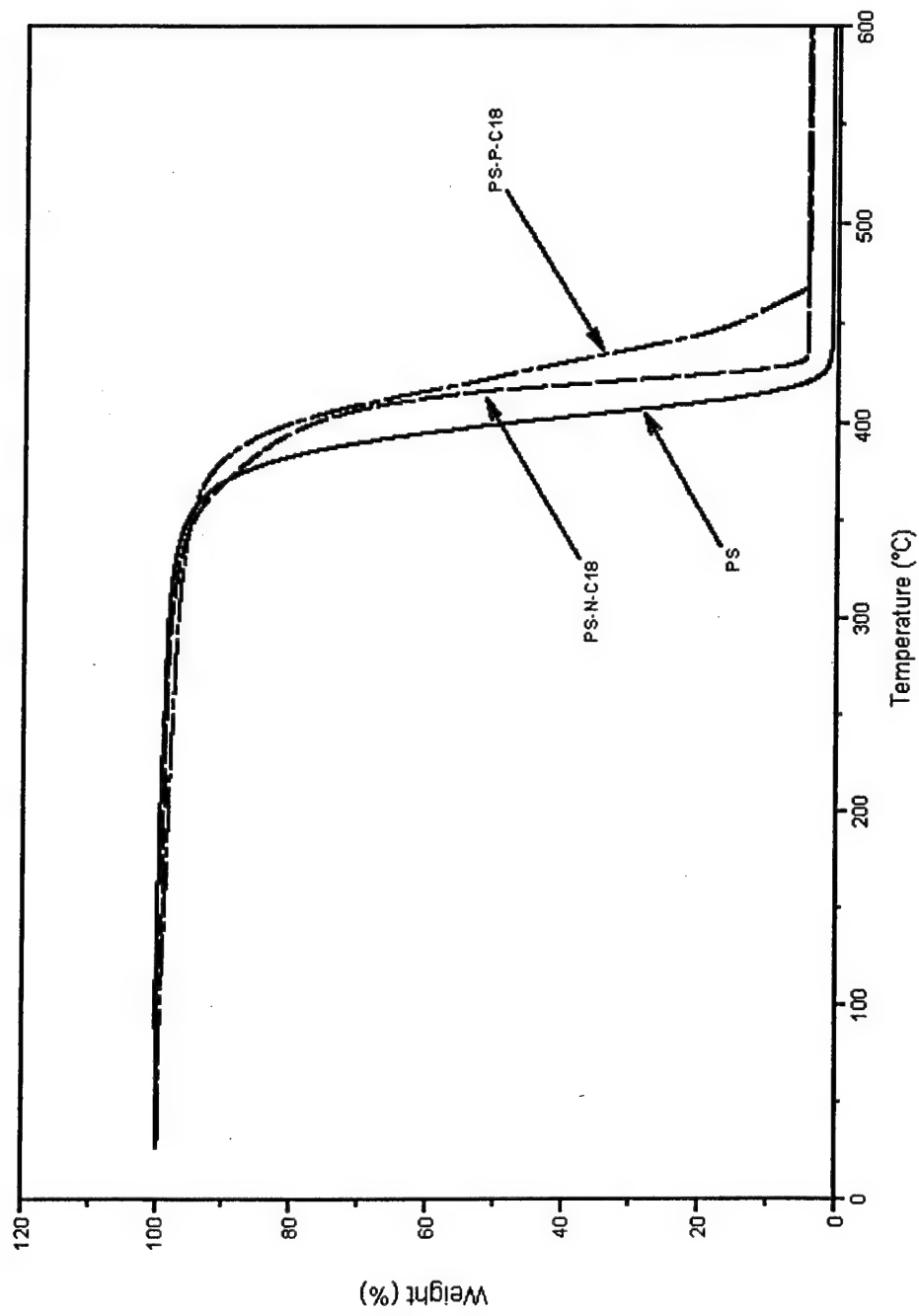
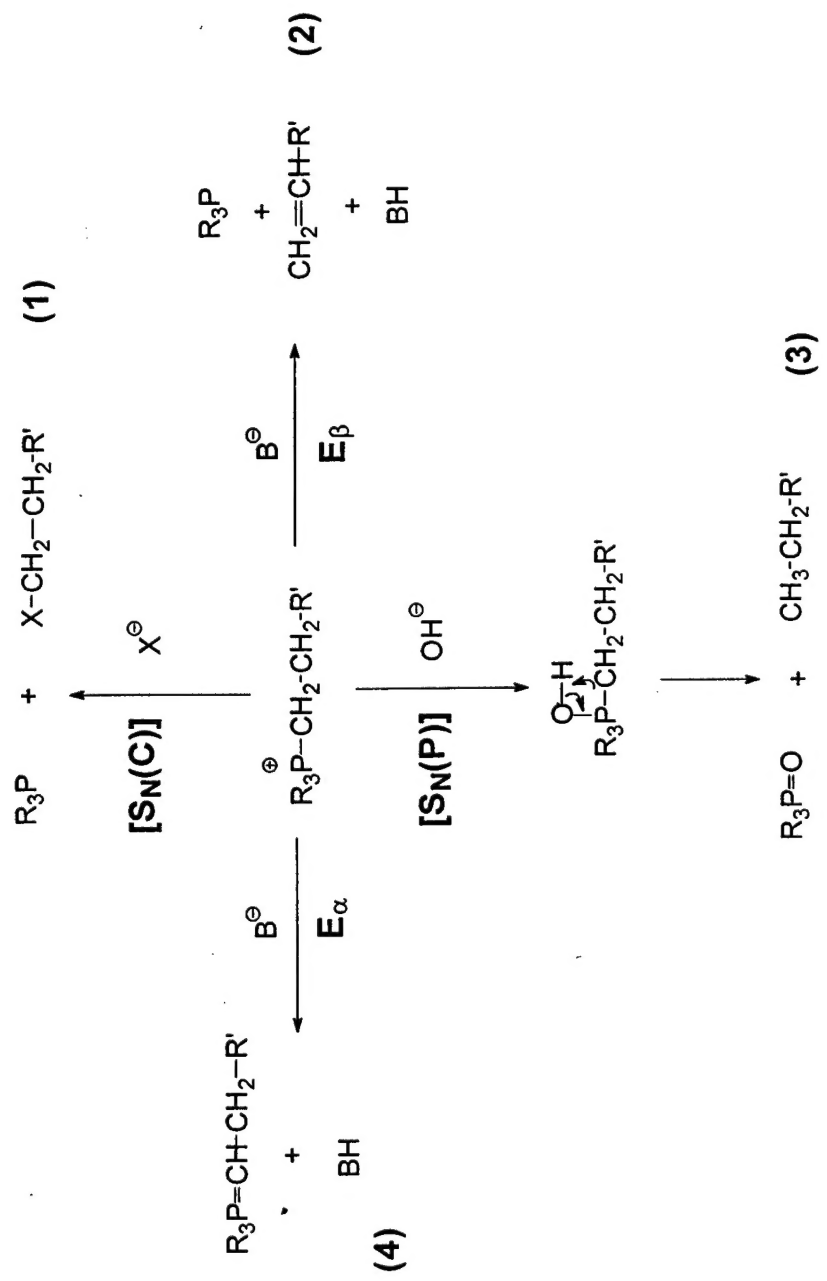
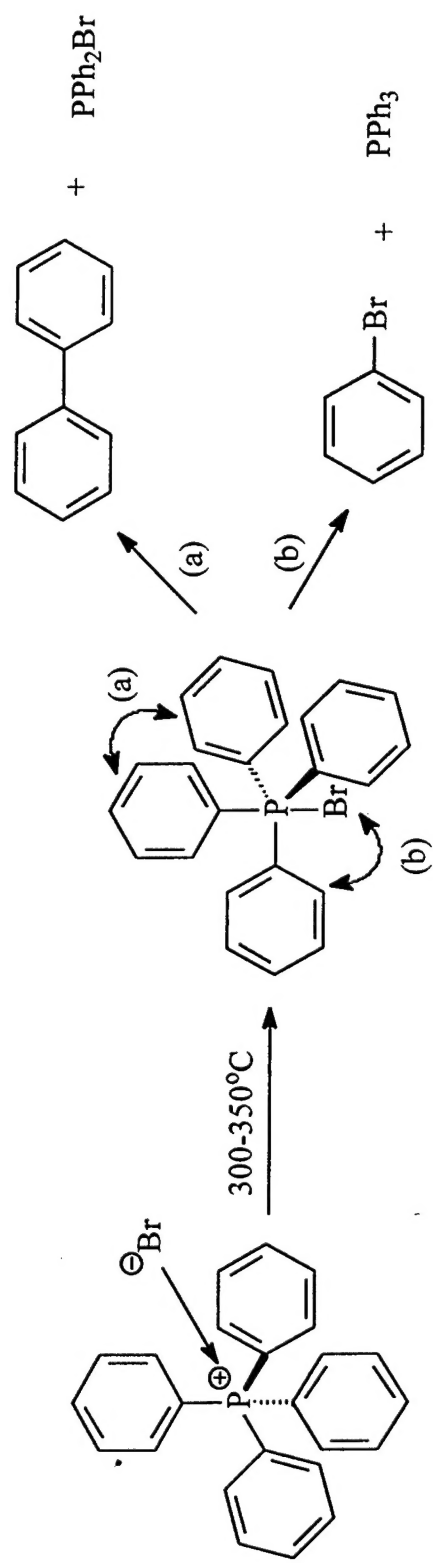


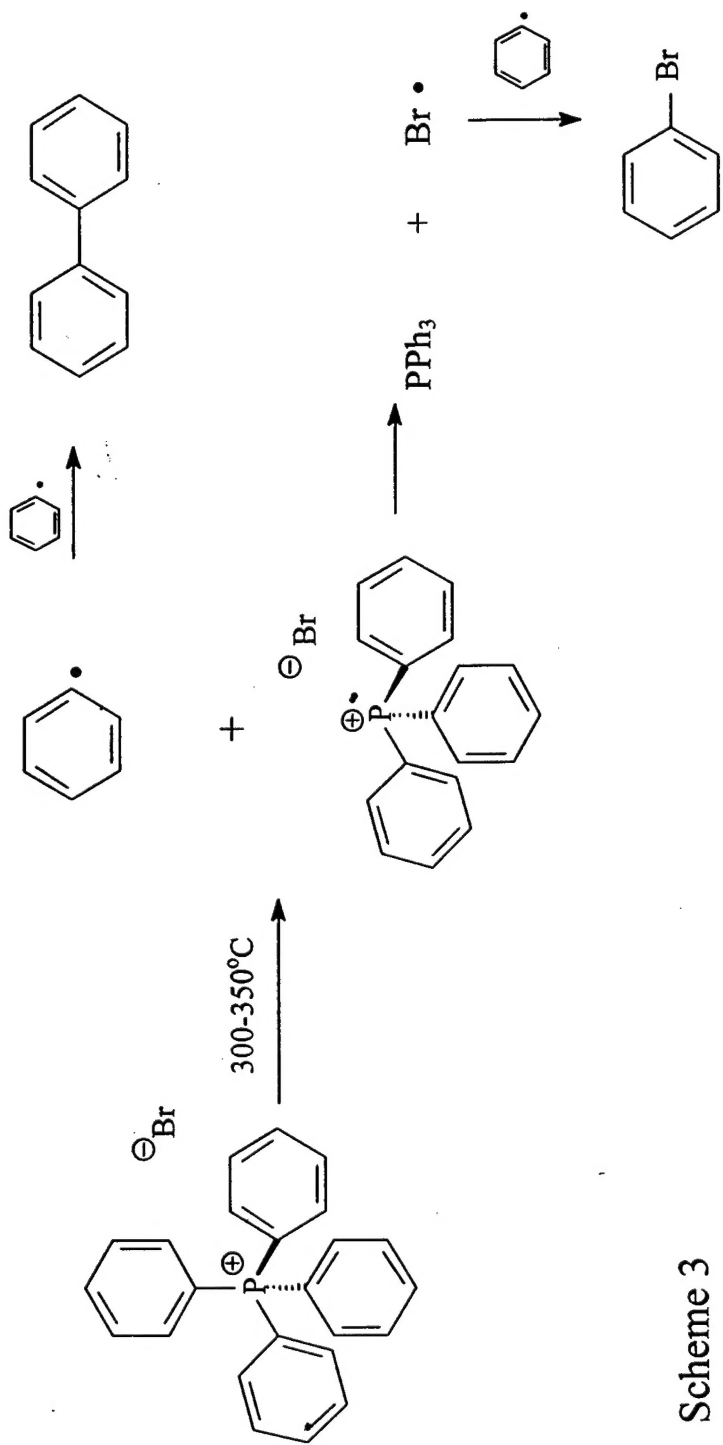
Figure 39. Comparison of TGA results of PS, PS-N-C18 nanocomposite and PS-P-C18 nanocomposite.



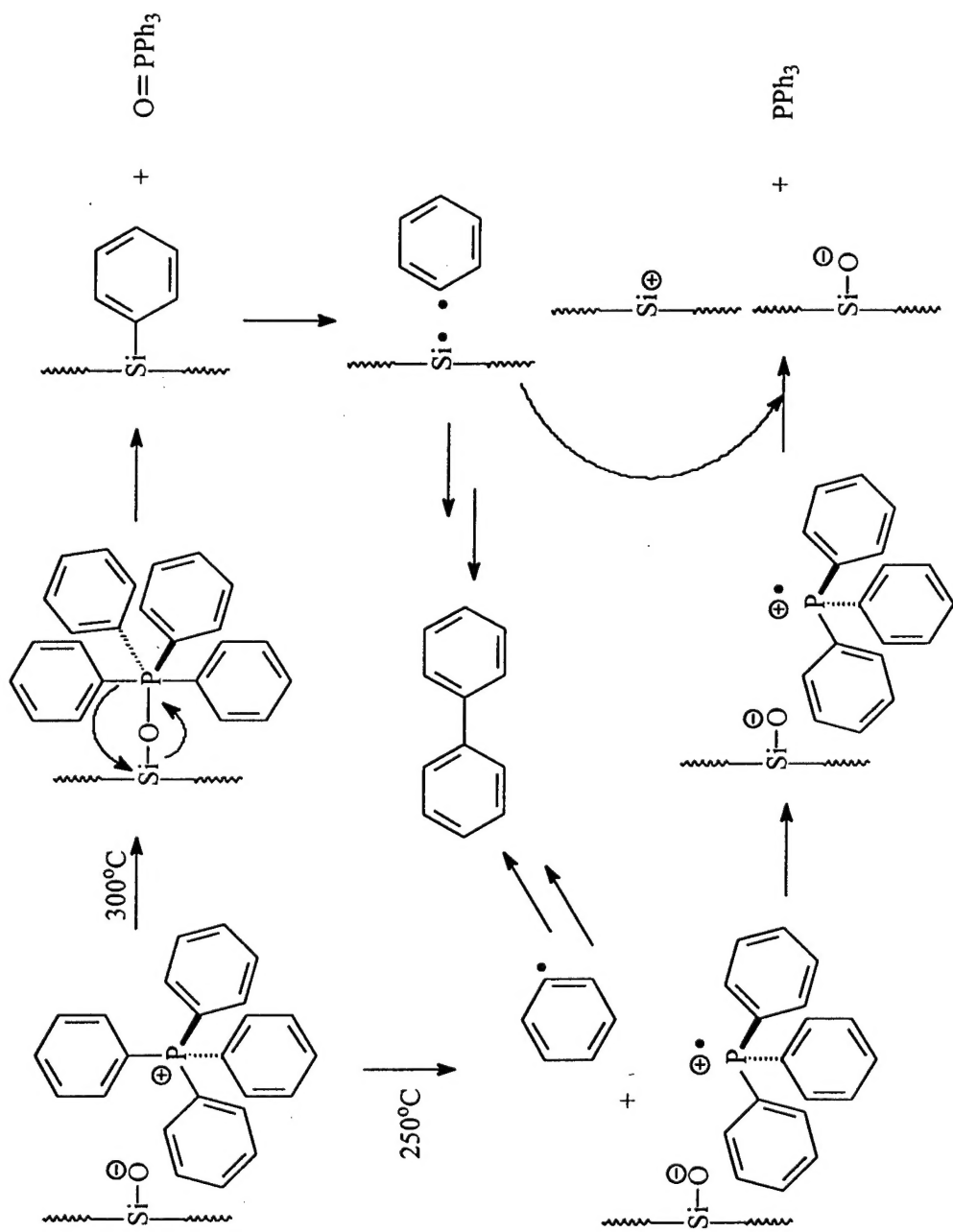
Scheme 1



Scheme 2



Scheme 3



Scheme 4